ISSN: 2153-1196 Volume 10, Number 9, August 2019

Scientific Research Publishing

Journal of Modern Physics

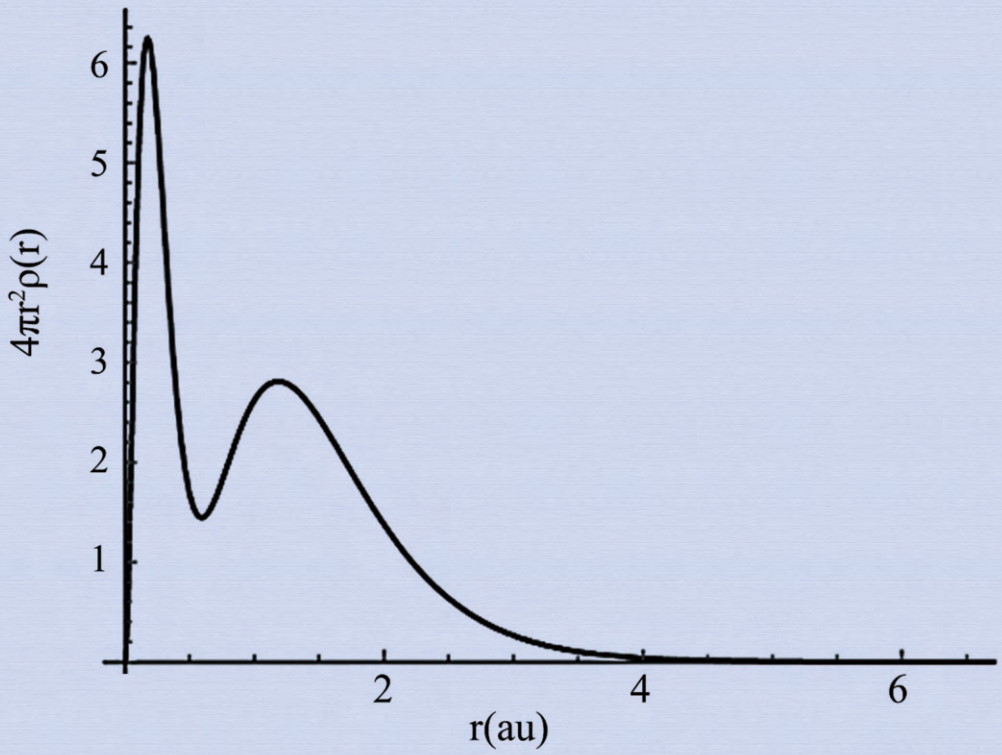

ISSN: 2153-1196

www.scirp.org/journal/jmp

Journal Editorial Board

ISSN: 2153-1196 (Print) ISSN: 2153-120X (Online)
http://www.scirp.org/journal/jmp

Editor-in-Chief

Editorial Board

Scientific Research Publishing

Journal of Modern Physics, 2019, 10, 1065-1156
http://www.scirp.org/journal/jmp
ISSN Online: 2153-120X
ISSN Print: 2153-1196

Table of Contents

Volume 10 Number 9 August 2019

The figure on the front cover is from the article published in Journal of Modern Physics, 2019, Vol. 10, No. 9 pp. 1134-1143 by Naranchimeg Davgiikhorol, Munkhsaikhan Gonchigsuren, Khenmedekh Lochin, Sukh Ochir and Tsogbadrakh Namsrai.

Journal of Modern Physics (JMP)
Journal Information

SUBSCRIPTIONS

The *Journal of Modern Physics* (Online at Scientific Research Publishing, www.SciRP.org) is published monthly by Scientific Research Publishing, Inc., USA.

Subscription rates:
Print: $89 per issue.
To subscribe, please contact Journals Subscriptions Department, E-mail: sub@scirp.org

SERVICES

Advertisements
Advertisement Sales Department, E-mail: service@scirp.org

Reprints (minimum quantity 100 copies)
Reprints Co-ordinator, Scientific Research Publishing, Inc., USA.
E-mail: sub@scirp.org

COPYRIGHT

PRODUCTION INFORMATION

For manuscripts that have been accepted for publication, please contact:
E-mail: jmp@scirp.org

Journal of Modern Physics, 2019, 10, 1065-1082
http://www.scirp.org/journal/jmp
ISSN Online: 2153-120X
ISSN Print: 2153-1196

A Quantum Dynamics of Heisenberg Model of the Neutron Associated with Beta Decay

Vu B. Ho

Advanced Study, 9 Adela Court, Mulgrave, Australia
Email: vubho@bigpond.net.au

How to cite this paper: Ho, V.B. (2019) A Quantum Dynamics of Heisenberg Model of the Neutron Associated with Beta Decay. *Journal of Modern Physics*, **10**, 1065-1082.
https://doi.org/10.4236/jmp.2019.109069

Received: June 13, 2019
Accepted: July 30, 2019
Published: August 2, 2019

Abstract

In this work we re-examine a model of the nucleons that involve the weak interaction which was once considered by Heisenberg; that is a neutron may have the structure of a dwarf hydrogen-like atom. We formulate a quantum dynamics for the Heisenberg model of the neutron associated with interaction that involves the beta decay in terms of a mixed Coulomb-Yukawa potential and the More General Exponential Screened Coulomb Potential (MGESCP), which has been studied and applied to various fields of physics. We show that all the components that form the MGESCP potential can be derived from a general system of linear first order partial differential equations similar to Dirac relativistic equation in quantum mechanics. There are many interesting features that emerge from the MGESCP potential, such as the MGESCP potential can be reduced to the potential that has been proposed to describe the interaction between the quarks for strong force in particle physics, and the energy spectrum of the bound states of the dwarf hydrogen-like atom is continuous with respect to distance. This result leads to an unexpected implication that a proton and an electron may also interact strongly at short distances. We also show that the Yukawa potential when restrained can generate and determine the mathematical structures of fundamental particles associated with the strong and weak fields.

Keywords

Quantum Dynamics, Beta Decay, Weak and Strong Interactions, Dirac Equations, Coulomb Potential, Yukawa Potential, MGESCP Potential, Differential Equations

1. Introduction

Despite that the mathematical formulation of quantum mechanics has been highly developed and the theory has been successfully applied into all domains

of applied sciences with the most accuracies that can be achieved by experiments, many fundamental physical processes at the quantum level that involve quantum mechanics still remain a mystery. In particular, one of the profound epistemological problems that continue to exist is the question of whether microscopic phenomena are in fact continuous or progressing in quantum jumps. In an article entitled ARE THERE QUANTUM JUMPS? Schrödinger wrote: "… A great many of our educated contemporaries, not equipped with the mathematical apparatus to follow our more technical deliveries, are yet deeply concerned with many general questions; one of the most stirring among them certainly is whether actually *natura facit saltus* or no …" [1]. It seems Schrödinger himself did not believe in abrupt quantum transitions, especially when physical phenomena are not considered as real but only associated with the probability view. Fundamentally, even quantum physical processes are occurring in a deterministic manner, down to the quantum level in the process of creation of elementary particles and radiation of mediators of physical fields. In this work we will discuss a physical process that belongs to the quantum domain but the physical process can be described deterministically and continuously; that is the beta minus decay in which a neutron n is transformed into a proton p and an electron e^- and an electron antineutrino $\overline{\nu}_e$ are emitted from the system. In the beta minus decay, the electrons are emitted with a continuous spectrum of energy, which can be represented symbolically as $n = p + e^- + \overline{\nu}_e$. In 1932 Werner Heisenberg proposed a form of interaction between the neutrons and protons inside the nucleus, in which neutrons were composite particles of protons and electrons. These composite neutrons would emit electrons, creating an attractive force with the protons, and then turn into protons themselves [2]. Despite that there were many issues with his theory, Heisenberg has an idea of an exchange interaction between particles inside the nucleus and the idea inspired Fermi to formulate a theory of beta decay by proposing the emission and absorption of the neutrino and electron, rather than just the electron as in Heisenberg's theory [3]. However, since the force associated with the neutrino and electron emission was shown not strong enough to bind the protons and neutrons in the nucleus, in his 1935 paper, Hideki Yukawa combined Heisenberg's idea of short-range interaction and Fermi's idea of an exchange particle to introduce a potential which includes an electromagnetic term and a term that decays exponentially [4]. Yukawa used the new potential to predict a massive mediator for the strong interaction. The massive mediator is called meson as its mass was in the middle of the proton and electron.

Since the energy spectrum of the emitted electron in the beta minus decay is continuous therefore Heisenberg's model of the neutron as a dwarf hydrogen-like atom cannot be realised if we only apply the Coulomb potential to describe the system. Instead, in this work we will show that a continuous spectrum of energy can be obtained by applying a mixed Coulomb-Yukawa potential of the form

$$V(r) = -\alpha \frac{e^{-\beta r}}{r} + \frac{Q}{r}, \tag{1}$$

where Q, α and β are physical parameters that will need to be determined [5] [6]. Furthermore, in order to account for possible bound states of a dwarf hydrogen-like atom which can be identified with a neutron we will need to use a more general form of Yukawa potential, which has been studied and applied to various fields of physics, the More General Exponential Screened Coulomb Potential (MGESCP) given as

$$V(r) = -\frac{V_0 e^{-2\alpha r}}{r} - \frac{V_0}{r} - V_0 \alpha e^{-2\alpha r}, \tag{2}$$

where V_0 is the potential depth and the parameter α is the strength coupling constant [7] [8]. Remarkably, we will show that the MGESCP potential can be reduced to the potential that has been proposed for the interactions between the quarks for strong force in particle physics and this result leads to an unexpected implication that a proton and an electron may also interact strongly at short distances. There are also prominent features that emerge from using the MGESCP potential to describe a neutron as a dwarf hydrogen-like atom, such as the energy spectrum of the bound states is continuous with respect to distance, and, as discussed in Section 3, the Yukawa potential can be restrained to generate and determine mathematical structures of physical objects that may be identified with the quantum mediators associated with the weak and strong interactions. With this regard, it is reasonable to suggest that functional potentials in physics may have physical mechanisms to generate mediators of associated physical fields, and these mechanisms can be formulated in terms of differentiable manifolds and their corresponding direct sums of prime manifolds as discussed in our works on the possibility to formulate physics in terms of differential geometry and topology [9].

2. Formulating Potentials from a System of Equations Similar to Dirac Equation

In the present state of physics there are four confirmed types of interactions between physical objects, which are the gravitational interaction, the electromagnetic interaction, the strong interaction, and the weak interaction. Except for the gravitational interaction, the other three types of interactions can be mathematically formulated so that they can comply with quantum mechanics, especially in the so-called standard model of particle physics [10]. In this section we will discuss a quantum dynamics of the interaction for the beta minus decay by deriving different types of potentials from a general system of linear first order partial differential equations which can be reduced to a system of equations similar to Dirac relativistic equation in quantum mechanics. It should be mentioned here that, unlike Dirac relativistic equation that is derived from the assumption of Lorentz invariance, solutions of differential equations which are similar to Dirac equation but are derived from a general system of differential equations can be

used to represent different type of physical objects rather than the exclusive mathematical wavefunctions that are used to calculate the probability of the outcome of an experimental result as proposed in quantum mechanics. For example, in our work on the fluid state of Dirac quantum particles, we showed that similar Dirac wavefunctions can be used to represent the stream function and velocity potential of a static fluid [11]. We now show that similar Dirac equation for a free particle, similar Dirac equation for an arbitrary field, and their corresponding solutions identified as potentials can be formulated from a general system of linear first order partial differential equations [12]. A general system of linear first order partial differential equations can be written in the form [13] [14]

$$\sum_{i=1}^{n}\sum_{j=1}^{n}a_{ij}^{r}\frac{\partial\psi_i}{\partial x_j}=\sum_{i=1}^{n}\left(\sum_{j=1}^{n}b_{ij}^{r}V_j+c_i^{r}\right)\psi_i+d^{r},\quad r=1,2,\cdots,n \tag{3}$$

The system of equations given in Equation (3) can be rewritten in a matrix form as

$$\left(\sum_{i=1}^{n}A_i\frac{\partial}{\partial x_i}\right)\psi=-\mathrm{i}\left(\sum_{i=1}^{n}qB_iV_i+m\sigma\right)\psi+\mathrm{i}kJ, \tag{4}$$

where $\psi=\left(\psi_1,\psi_2,\cdots,\psi_n\right)^{\mathrm{T}}$, $\partial\psi/\partial x_i=\left(\partial\psi_1/\partial x_i,\partial\psi_2/\partial x_i,\cdots,\partial\psi_n/\partial x_i\right)^{\mathrm{T}}$ with A_i,B_i and σ are matrices representing the quantities $a_{ij}^{r},b_{ij}^{r},c_j^{r}$, which are assumed to be constant in this work, and kJ is a matrix that represents the quantity d^{r}, where k is a dimensional constant. As normal convention, the letter i in front of the last two terms in Equation (4) is the imaginary number i. While the quantities q, m and kJ represent physical entities related directly to the physical properties of the particle under consideration, the quantities V_i represent the potentials of an external field, such as an electromagnetic field or the matter field of a quantum particle. In order to formulate a physical theory from the system of equations given in Equation (4), it is necessary to determine the unknown quantities A_i,B_i and σ, as well as the mathematical conditions that they must satisfy, such as commutation relations between them. The commutation relations between the matrices can be determined if we apply the operator $\sum_{i=1}^{n}A_i\partial/\partial x_i$ on the left on both sides of Equation (4) as follows

$$\left(\sum_{i=1}^{n}A_i\frac{\partial}{\partial x_i}\right)\left(\sum_{j=1}^{n}A_j\frac{\partial}{\partial x_j}\right)\psi=\left(\sum_{i=1}^{n}A_i\frac{\partial}{\partial x_i}\right)\left(-\mathrm{i}\left(\sum_{j=1}^{n}qB_jV_j+m\sigma\right)\psi+\mathrm{i}kJ\right). \tag{5}$$

Since the quantities A_i,B_i,σ,q and m are assumed to be constant, Equation (5) becomes

$$\begin{aligned}&\left(\sum_{i=1}^{n}A_i^{2}\frac{\partial^2}{\partial x_i^2}+\sum_{i=1}^{n}\sum_{j>i}^{n}\left(A_iA_j+A_jA_i\right)\frac{\partial^2}{\partial x_i\partial x_j}\right)\psi\\&=\left(-\mathrm{i}\left(\sum_{i=1}^{n}A_i\frac{\partial}{\partial x_i}\right)\left(\sum_{j=1}^{n}qB_jV_j+m\sigma\right)\right)\psi\\&\quad-\mathrm{i}\left(\sum_{i=1}^{n}qB_iV_i+m\sigma\right)\left(\left(\sum_{j=1}^{n}A_j\frac{\partial}{\partial x_j}\right)\psi\right)+\sum_{i=1}^{n}A_i\frac{\partial(\mathrm{i}kJ)}{\partial x_i}\end{aligned} \tag{6}$$

$$= -\mathrm{i}\left(\sum_{i=1}^{n}\sum_{j=1}^{n} qA_iB_j\frac{\partial V_j}{\partial x_i}\right)\psi - \left(\sum_{i=1}^{n}\sum_{j>i}^{n} q^2\left(B_iB_j + B_jB_i\right)V_iV_j - 2\mathrm{i}\sum_{i=1}^{n} qmB_iV_i\sigma - m^2\sigma^2\right)\psi - \mathrm{i}\left(\sum_{i=1}^{n} qB_iV_i + m\sigma\right)\left(\mathrm{i}kJ\right) + \sum_{i=1}^{n} A_i\frac{\partial\left(\mathrm{i}kJ\right)}{\partial x_i}$$

In order to describe the dynamics of a particular physical system, undetermined parameters given in Equation (4) must be specified accordingly. To obtain a system of partial differential equations similar to Dirac equation for an arbitrary field $\left(\gamma^\mu\left(i\partial_\mu - qV_\mu\right) - m\right)\psi = 0$ [15], we set $B_i = A_i = \gamma_i$, $\sigma = 1$ and $A_iA_j + A_jA_i = 0$. In this case Equation (4) becomes

$$\left(\sum_{i=1}^{4}\gamma_i\frac{\partial}{\partial x_i}\right)\psi = -\mathrm{i}\left(\sum_{i=1}^{4} q\gamma_iV_i + m\right)\psi + \mathrm{i}kJ, \tag{7}$$

where the matrices A_i and B_i have been identified with Dirac matrices γ_i as follows

$$\gamma_1 = \begin{pmatrix} 1 & 0 & 0 & 0 \\ 0 & 1 & 0 & 0 \\ 0 & 0 & -1 & 0 \\ 0 & 0 & 0 & -1 \end{pmatrix}, \gamma_2 = \begin{pmatrix} 0 & 0 & 0 & 1 \\ 0 & 0 & 1 & 0 \\ 0 & -1 & 0 & 0 \\ -1 & 0 & 0 & 0 \end{pmatrix},$$
$$\gamma_3 = \begin{pmatrix} 0 & 0 & 0 & -i \\ 0 & 0 & i & 0 \\ 0 & i & 0 & 0 \\ -i & 0 & 0 & 0 \end{pmatrix}, \gamma_4 = \begin{pmatrix} 0 & 0 & 1 & 0 \\ 0 & 0 & 0 & -1 \\ -1 & 0 & 0 & 0 \\ 0 & 1 & 0 & 0 \end{pmatrix} \tag{8}$$

For the case of Dirac equation, the matrices γ_i and σ satisfy the following conditions

$$\gamma_i^2 = \pm 1 \tag{9}$$

$$\gamma_i\gamma_j + \gamma_j\gamma_i = 0 \quad \text{for } i \neq j \tag{10}$$

It is seen from Equation (4) that the quantity kJ represents an internal source which is associated with a dynamical process of a quantum particle. For example, a quantum particle is undergoing some form of physical evolution that changes its physical structure, such as an accumulation of mass during its formation. In fact we will show that this physical process can be formulated using the MGESCP potential in which the energy spectrum depends continuously on distance. In terms of the gamma matrices γ_i then Equation (7) can be rewritten in a covariant form similar to Dirac equation for an arbitrary field with an internal source kJ as

$$\left(\gamma^\mu\left(\mathrm{i}\partial_\mu - qV_\mu\right) - m\right)\psi = \mathrm{i}kJ. \tag{11}$$

In this case Equation (6) also reduces to the following equation

$$\left(\sum_{i=1}^{4}\gamma_i^2\frac{\partial^2}{\partial x_i^2}\right)\psi = \left(-\mathrm{i}\sum_{i=1}^{4}\sum_{j>i}^{4} q\gamma_i\gamma_j\left(\frac{\partial V_j}{\partial x_i} - \frac{\partial V_i}{\partial x_j}\right) + 2\mathrm{i}\sum_{i=1}^{4} qm\gamma_iV_i - m^2\right)\psi - \mathrm{i}\left(\sum_{i=1}^{n} q\gamma_iV_i + m\sigma\right)\left(\mathrm{i}kJ\right) + \sum_{i=1}^{n}\gamma_i\frac{\partial\left(\mathrm{i}kJ\right)}{\partial x_i}. \tag{12}$$

If the quantities V_i are the four-potential of an electromagnetic field given by the identification $(V_1,V_2,V_3,V_4)=(V,A_x,A_y,A_z)$ then Equation (12) can be used to determine the dynamics of the components of the wavefunction $\psi=(\psi_1,\psi_2,\psi_3,\psi_3)^{\mathrm{T}}$, where the term $\partial V_j/\partial x_i-\partial V_i/\partial x_j$ are the components of the electric field $\boldsymbol{E}$ and the magnetic field $\boldsymbol{B}$.

Now we will discuss how free quantum particles can create their own physical fields in which wavefunctions can be identified as potentials. Therefore we set $\sum_{i=1}^{n} qB_iV_i=0$. Equations (7) and (12) for free particles reduce to equations

$$\gamma^{\mu}\partial_{\mu}\psi=-\mathrm{i}m\psi+\mathrm{i}kJ, \tag{13}$$

$$\gamma_i^2\frac{\partial^2\psi}{\partial x_i^2}=-m^2\psi+mkJ+\gamma_i\frac{\partial(\mathrm{i}kJ)}{\partial x_i}. \tag{14}$$

In the following we will consider two cases depending on the conditions that are applied to the internal source kJ in which either $kJ=0$ or $\neq 0$. For the case $kJ=0$, Equation (13) reduces to a form similar to Dirac equation for a free particle

$$\gamma^{\mu}\partial_{\mu}\psi=-\mathrm{i}m\psi. \tag{15}$$

For massive particles in which $m\neq 0$, all components of the wavefunction ψ_{μ} satisfy the Klein-Gordon equation

$$\frac{\partial^2\psi_{\mu}}{\partial t^2}-\frac{\partial^2\psi_{\mu}}{\partial x^2}-\frac{\partial^2\psi_{\mu}}{\partial y^2}-\frac{\partial^2\psi_{\mu}}{\partial z^2}=-m^2\psi_{\mu}. \tag{16}$$

And, in particular, if the wavefunctions are time-independent then we obtain

$$\frac{\partial^2\psi_{\mu}}{\partial x^2}+\frac{\partial^2\psi_{\mu}}{\partial y^2}+\frac{\partial^2\psi_{\mu}}{\partial z^2}=m^2\psi_{\mu}. \tag{17}$$

In this case the wavefunctions ψ_{μ} can be viewed as static Yukawa potential

$$\psi_{\mu}(r)=-\alpha\frac{\mathrm{e}^{-\beta r}}{r}, \tag{18}$$

where α and β are undetermined dimensional constants [10]. It should be mentioned here that, unlike Dirac wavefunctions that represent spinor fields, the wavefunctions ψ_{μ} in this work are simply the components of vector fields that are solutions of a system of linear first order partial differential equations. The identification of the wavefunctions ψ_{μ} can be viewed either as static Yukawa potential or Coulomb potential is similar to the identification that we discussed in our work on the fluid state of Dirac quantum particles in which Dirac-like wavefunctions are identified either with a velocity potential or a stream function [11]. According to Yukawa work, the wavefunctions given in Equation (18) can be associated with the strong interaction between nuclear particles.

For massless time-independent particles, the Klein-Gordon equation given in Equation (17) reduces to Laplace equation

$$\frac{\partial^2\psi_{\mu}}{\partial x^2}+\frac{\partial^2\psi_{\mu}}{\partial y^2}+\frac{\partial^2\psi_{\mu}}{\partial z^2}=0. \tag{19}$$

Solutions to Laplace equation can be written in the form

$$\psi_{\mu}\left(x,y,z\right)=\frac{Q}{r}. \tag{20}$$

In this case the wavefunctions ψ_{μ} can be viewed as static Coulomb potential, where Q is an undetermined dimensional constant, which is associated with the electromagnetic interaction between elementary particles.

As mentioned in the introduction, we will discuss possible bound states of a dwarf hydrogen-like atom which can be identified with a neutron therefore we will need to use a more general form of Yukawa potential, which is the MGESCP potential given as in Equation (2). Since the MGESCP potential has an extra term of the form $\psi_{\mu}=a\mathrm{e}^{-mr}$, therefore we now need to show how to derive this form of potential from the Dirac-like equation with an internal source given in Equation (13). Now, Dirac-like wavefunctions ψ_{μ} satisfy the following Klein-Gordon-like equation with a source

$$\frac{\partial^2\psi_{\mu}}{\partial t^2}-\frac{\partial^2\psi_{\mu}}{\partial x^2}-\frac{\partial^2\psi_{\mu}}{\partial y^2}-\frac{\partial^2\psi_{\mu}}{\partial z^2}=-m^2\psi_{\mu}+mkJ+\gamma_i\frac{\partial\left(\mathrm{i}kJ\right)}{\partial x_i}. \tag{21}$$

In particular, if the wavefunctions are time-independent then we obtain

$$\frac{\partial^2\psi_{\mu}}{\partial x^2}+\frac{\partial^2\psi_{\mu}}{\partial y^2}+\frac{\partial^2\psi_{\mu}}{\partial z^2}=m^2\psi_{\mu}-mkJ-\gamma_i\frac{\partial\left(\mathrm{i}kJ\right)}{\partial x_i}. \tag{22}$$

It can be verified that a solution of the form $\psi_{\mu}=a\mathrm{e}^{-mr}$, where a and m are constants, satisfies the following equation

$$\frac{\partial^2\psi_{\mu}}{\partial x^2}+\frac{\partial^2\psi_{\mu}}{\partial y^2}+\frac{\partial^2\psi_{\mu}}{\partial z^2}=m^2\psi_{\mu}-\frac{2ma\mathrm{e}^{-mr}}{r}. \tag{23}$$

By comparing Equation (23) to Equation (22), we obtain the following equation for the internal quantity kJ

$$mkJ+\gamma_i\frac{\partial\left(\mathrm{i}kJ\right)}{\partial x_i}=\frac{2am\mathrm{e}^{-mr}}{r}. \tag{24}$$

A differential equation for the quantity kJ can be determined by using the matrices γ_i given in Equation (8), which is written in an explicit form as

$$\begin{aligned}&\begin{pmatrix}0&0&0&1\\0&0&1&0\\0&-1&0&0\\-1&0&0&0\end{pmatrix}\frac{\partial\left(\mathrm{i}kJ\right)}{\partial x}+\begin{pmatrix}0&0&0&-i\\0&0&i&0\\0&i&0&0\\-i&0&0&0\end{pmatrix}\frac{\partial\left(\mathrm{i}kJ\right)}{\partial y}\\&+\begin{pmatrix}0&0&1&0\\0&0&0&-1\\-1&0&0&0\\0&1&0&0\end{pmatrix}\frac{\partial\left(\mathrm{i}kJ\right)}{\partial z}=\begin{pmatrix}1&0&0&0\\0&1&0&0\\0&0&1&0\\0&0&0&1\end{pmatrix}\left(-mkJ+\frac{2am\mathrm{e}^{-mr}}{r}\right).\end{aligned} \tag{25}$$

From Equation (25) we obtain the following equations for the quantity kJ

$$-mkJ+\frac{2am\mathrm{e}^{-mr}}{r}=0, \tag{26}$$

$$\frac{\partial(kJ)}{\partial z}=0,\ \frac{\partial(kJ)}{\partial x}-\mathrm{i}\frac{\partial(kJ)}{\partial y}=0,\ \frac{\partial(kJ)}{\partial x}+\mathrm{i}\frac{\partial(kJ)}{\partial y}=0. \tag{27}$$

The equations given in Equation (27) show that the source kJ is constant and from Equation (26) this also results in the constancy of the Yukawa potential which can be written as

$$\frac{\mathrm{e}^{-mr}}{r}=\frac{kJ}{2a}. \tag{28}$$

Now we apply the results that have been obtained into the MGESCP potential given in Equation (2), one of whose components has the form $\psi_\mu=V_0\alpha\mathrm{e}^{-2\alpha r}$. By comparing this potential to $\psi_\mu=a\mathrm{e}^{-mr}$ we have $a=V_0\alpha$ and $m=2\alpha$. With the Yukawa potential that is restrained by the condition given in Equation (28) the MGESP potential given in Equation (2) is reduced to

$$V(r)=-\frac{V_0}{r}\left(1+(1+\alpha r)\mathrm{e}^{-2\alpha r}\right)=-\frac{V_0}{r}+\frac{kJ}{2\alpha}(1+\alpha r)=-\frac{V_0}{r}+\frac{kJ}{2}r+\frac{kJ}{2\alpha}. \tag{29}$$

Except for the constant $kJ/2\alpha$, the potential given in Equation (29) has the form that is similar to the potential that describes an interaction between two fundamental quarks as proposed in the theory of quantum chromodynamics, namely, $V(r)=A/r+Br$. This type of potential describes interactions between two quarks that can be represented in the following picture shown in Figure 1 and Figure 2.

For small values of the distance r the potential manifests as a Coulomb potential $V=A/r$, however, for large values of distance the potential acts as a linear potential with respect to the distance $V=Br$. The linear potential shown in Figure 2 is a flux tube of energy in which the quantity B has the dimension of a cross-sectional energy therefore by comparison we may also interpret the quantity kJ in Dirac equation given in Equation (7) also as a cross-sectional energy. The reduced form of the MGESCP potential also indicates that a proton and an electron can attract strongly at very short distances so that they can bind and form a dwarf hydrogen-like atom.

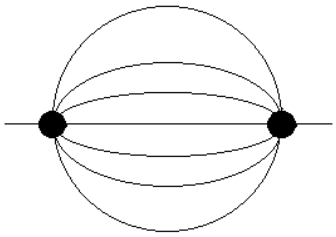

Figure 1. For small r $\boldsymbol{V=A/r}$.

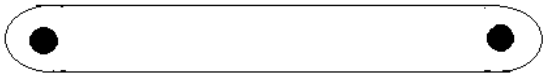

Figure 2. For large r $\boldsymbol{V=Br}$.

3. Topological Structures of Elementary Particles Generated by Yukawa Potential

In this section we discuss further the restraint to the Yukawa potential given in Equation (28) which has been shown to reduce the MGESCP potential to the potential that is proposed for the interaction between the quarks for strong force in particle physics. We now show that in fact the restrained Yukawa potential actually generates and determines mathematical structures of physical objects that may be identified with quantum mediators of the weak and strong interactions. Instead of giving a mathematical analysis of the restrained Yukawa potential given in Equation (28), as an illustration, we simply plot possible shapes that can be generated and determined by a restrained Yukawa potential from the relation given in Equation (28), namely, $\mathrm{e}^{-mr} = (kJ/2a)r$, with different values given to the parameters m and $kJ/2a$. Together, they possess a remarkable difference in their topological structures that may underlie physical effects that are associated with elementary quantum particles [16].

For the case $m = 0.001$ with $kJ/2a = \gamma = 1, 2, 3, 4$ we have the following possible shapes for elementary quantum particles as shown in **Figures 3-6**.

Figure 3. $\gamma = 1$.

Figure 4. $\gamma = 2$.

Figure 5. $\gamma = 3$.

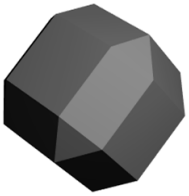

Figure 6. $\gamma = 4$.

For the case $m = 0.01$ with $kJ/2a = \gamma = 1,2,3,4$ we have the following possible shapes for elementary quantum particles as shown in Figures 7-10.

For the case $m = 0.1$ with $kJ/2a = \gamma = 0.1,1,2,3$ we have the following possible shapes for elementary quantum particles as shown in Figures 11-14.

Figure 7. $\gamma = 1$.

Figure 8. $\gamma = 2$.

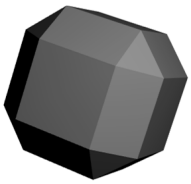

Figure 9. $\gamma = 3$.

Figure 10. $\gamma = 4$.

Figure 11. $\gamma = 0.1$.

Figure 12. $\gamma = 1$.

Figure 13. $\gamma = 2$.

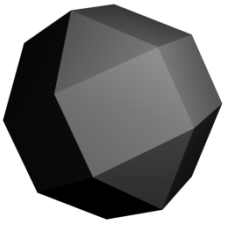

Figure 14. $\gamma = 3$.

For the case $m = 1$ with $kJ/2a = \gamma = 0.001, 0.01, 0.1, 1$ we have the following possible shapes for elementary quantum particles as shown in Figures 15-18.

For the case $m = 5$ with $kJ/2a = \gamma = 10^{-11}, 10^{-3}, 0.01, 0.1$ we have the following possible shapes for elementary quantum particles as shown in Figures 19-22.

For the case $m = 10$ with $kJ/2a = \gamma = 10^{-26}, 10^{-21}, 10^{-18}, 10^{-13}$ we have the following possible shapes for elementary quantum particles as shown in Figures 23-26.

4. A Quantum Dynamics of the Weak and Strong Interactions

In this section we will discuss whether a neutron can be modelled as a dwarf hydrogen-like atom with the two different mixed potentials given in Equations (1) and (2) so that it can be used to explain the physical processes associated with the beta minus decay. As shown in Section 2, these potentials can be formed from the three forms of potentials that have been derived from the Dirac equations. First we consider the mixed potential that is formed from the Coulomb potential and the Yukawa potential as given in Equation (1). As shown below, this form of potential can be used to explain how an electron can be repelled from a dwarf hydrogen-like atom composed of a proton and an electron. By differentiating Equation (1), we can obtain the following equations

$$\frac{\mathrm{d}V}{\mathrm{d}r} = \alpha \mathrm{e}^{-\beta r}\left[\frac{\beta}{r} + \frac{1}{r^2}\right] - \frac{Q}{r^2}, \quad \frac{\mathrm{d}^2V}{\mathrm{d}r^2} = -\alpha \mathrm{e}^{-\beta r}\left[\frac{\beta^2}{r} + \frac{2\beta}{r^2} + \frac{2}{r^3}\right] + \frac{2Q}{r^3}. \tag{30}$$

From Equation (30), the corresponding force of interaction $F(r) = -\mathrm{d}V/\mathrm{d}r$ is obtained as

$$F(r) = -\alpha \mathrm{e}^{-\beta r}\left[\frac{\beta}{r} + \frac{1}{r^2}\right] + \frac{Q}{r^2}. \tag{31}$$

Figure 15. $\gamma = 0.001$.

Figure 16. $\gamma = 0.01$.

Figure 17. $\gamma = 0.1$.

Figure 18. $\gamma = 1$.

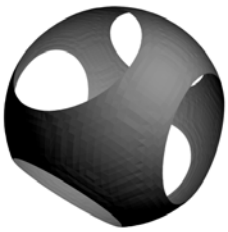

Figure 19. $\gamma = 10^{-11}$.

Figure 20. $\gamma = 10^{-3}$.

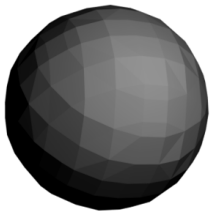

Figure 21. $\gamma = 0.01$.

Figure 22. $\gamma = 0.1$.

Figure 23. $\gamma = 10^{-26}$.

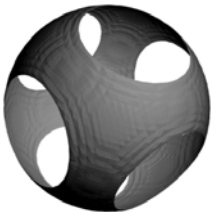

Figure 24. $\gamma = 10^{-21}$.

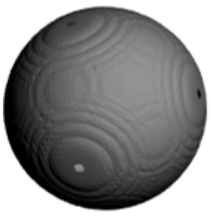

Figure 25. $\gamma = 10^{-18}$.

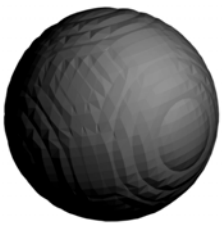

Figure 26. $\gamma = 10^{-13}$.

According to classical electrodynamics, the net force acting on the electron must be zero when it is circulating in stable orbits. If we assume the net force acting on the electron to vanish when it moves in a stationary orbit of finite radius $r = R = 1/\beta$, *i.e.* $F(1/\beta) = 0$, then from Equation (31) we obtain the relation

$$\beta^2\left(Q - \frac{2\alpha}{e}\right) = 0. \tag{32}$$

Since $\beta \neq 0$, we require $Q = 2\alpha/e$. The mixed potential given in Equation (1) now takes the form

$$V(r) = -\frac{eQ}{2}\frac{\mathrm{e}^{-\frac{r}{R}}}{r} + \frac{Q}{r}. \tag{33}$$

And the corresponding force of interaction $F(r) = -\mathrm{d}V/\mathrm{d}r$ is

$$F(r) = -\frac{eQ}{2}\mathrm{e}^{-\frac{r}{R}}\left[\frac{1}{Rr} + \frac{1}{r^2}\right] + \frac{Q}{r^2}. \tag{34}$$

In order to investigate further we need to know the nature of the stationary point at $r = R$. From Equation (30), the second derivative of $V(r)$ at $r = R$ is found as

$$\frac{\mathrm{d}^2V}{\mathrm{d}r^2} = -\frac{Q}{2R^3}. \tag{35}$$

Since we are considering the case for which the mixed potential given in Equation (33) is applied to the bound system of two charges of opposite signs, namely a proton and an electron, therefore the quantity Q can be written as $Q = -Kq_1q_2$, where $K > 0$ is a coupling constant. If q_1 is the charge of the proton, $q_1 = q$, and q_2 is the charge of the electron, $q_2 = -q$, then we have $Q = Kq^2 > 0$. Then from Equation (35) we obtain the condition $\mathrm{d}^2V/\mathrm{d}r^2 < 0$, therefore $V(r)$ has a local maximum at $r = R$. Since $F(r) = -\mathrm{d}V/\mathrm{d}r$, the force is attractive for $r < R$ and repulsive for $r > R$. This situation is seen similar to the case of weak interaction of beta minus decay in which a neutron turns into a proton and emits an electron and an anti-neutrino. First the neutron turns into a dwarf hydrogen-like atom, whose bound states will be described below using the MGESCP potential, then the electron moves in an orbit of zero force and then it is repelled from the dwarf hydrogen atom by a repulsive force. The force given in Equation (34) is rewritten as follows

$$F(r) = -\frac{eKq^2}{2}\mathrm{e}^{-\frac{r}{R}}\left[\frac{1}{Rr} + \frac{1}{r^2}\right] + \frac{Kq^2}{r^2}. \tag{36}$$

The force given in Equation (36) is assumed to be a weak force. Since R is the radius of the stationary orbit therefore we can assume that the electron is ejected from the stationary orbit because the equilibrium of this system at $r = R$ is unstable.

It can be seen that the whole process of beta decay is a complicated physical process that actually undergoes through many different physical configurations

of the system, therefore it can only be described approximately by many different dynamics, only if we can formulate the whole physical process under a mathematical formulation that can give rise to each physical configuration by some form of limit associated with mathematical parameters that are used to describe the whole system. With this in mind in the following we will discuss in terms of Schrödinger wave mechanics a more complete structure of a neutron as a dwarf hydrogen-like atom using a more complete MGESCP potential given in Equation (2). Consider the time-independent Schrödinger equation

$$-\frac{\hbar^2}{2\mu}\nabla^2\psi(\boldsymbol{r})+V(\boldsymbol{r})\psi(\boldsymbol{r})=E\psi(\boldsymbol{r}), \tag{37}$$

in which $V(r)$ is the More General Exponential Screened Coulomb Potential (MGESCP) given in Equation (2). Since the MGESCP potential is spherically symmetric, Equation (37) can be written in the spherical polar coordinates as

$$\begin{aligned}&-\frac{\hbar^2}{2\mu}\left(\frac{1}{r^2}\frac{\partial}{\partial r}\left(r^2\frac{\partial}{\partial r}\right)-\frac{\boldsymbol{L}^2}{\hbar^2r^2}\right)\psi(\boldsymbol{r})\\&+\left(-\frac{V_0}{r}\left(1+(1+\alpha r)\mathrm{e}^{-2\alpha r}\right)\right)\psi(\boldsymbol{r})=E\psi(\boldsymbol{r}),\end{aligned} \tag{38}$$

where the orbital angular momentum operator $\boldsymbol{L}^2$ is given by

$$\boldsymbol{L}^2=-\hbar^2\left(\frac{1}{\sin\theta}\frac{\partial}{\partial\theta}\left(\sin\theta\frac{\partial}{\partial\theta}\right)+\frac{1}{\sin^2\theta}\frac{\partial^2}{\partial^2\phi}\right). \tag{39}$$

Solutions of Equation (38) can be found using the separable form

$$\psi_{nl}(\boldsymbol{r})=R_{nl}(r)Y_{lm}(\theta,\phi), \tag{40}$$

where R_{nl} is a radial function and Y_{lm} is the spherical harmonic. Applying Equation (40), Equation (38) is reduced to the system of equations

$$\boldsymbol{L}^2Y_{lm}(\theta,\phi)=l(l+1)\hbar^2Y_{lm}(\theta,\phi), \tag{41}$$

$$\left(-\frac{\hbar^2}{2\mu}\left(\frac{\mathrm{d}^2}{\mathrm{d}r^2}+\frac{2}{r}\frac{\mathrm{d}}{\mathrm{d}r}\right)+\frac{l(l+1)\hbar^2}{2\mu r^2}-\frac{V_0}{r}\left(1+(1+\alpha r)\mathrm{e}^{-2\alpha r}\right)\right)R_{nl}(r)=ER_{nl}(r). \tag{42}$$

It has been shown that the radial solution $R_{nl}(r)$ to Equation (42) can be obtained as

$$R_{nl}(r)=N_{nl}r^{\left(-1+\sqrt{4l(l+1)+1}\right)/2}\mathrm{e}^{-\beta r}L_n^{1+\sqrt{4l(l+1)+1}}(2\beta r), \tag{43}$$

and the corresponding energy spectrum E_{nl} is given by

$$E_{nl}=-V_0\alpha\mathrm{e}^{-2\alpha r}-\frac{\mu}{2\hbar^2}\left(\frac{\left(V_0+V_0\mathrm{e}^{-2\alpha r}\right)}{n+l+1}\right)^2, \tag{44}$$

where $\beta^2=\left(2\mu\left(V_0+V_0\mathrm{e}^{-2\alpha r}\right)\right)/\hbar^2\left(2n+1+\sqrt{4l(l+1)+1}\right)^2$ [8]. Although this energy spectrum is discrete with respect to the quantum numbers *n* and *l*, it depends continuously on the radial distance *r*. In order to interpret the energy spectrum given in Equation (44) as some of energy spectrum associated with the

beta minus decay we need to apply the restraint condition applied to the Yukawa given in Equation (28) so that the MGESCP potential is reduced to the potential that is used to describe strong interaction at very short distances so that a proton and an electron can form a dwarf hydrogen-like atom. Then we obtain

$$E_{nl} = -\frac{kJ}{2}r - \frac{\mu}{2\hbar^2}\left(\frac{\left(V_0 + \left(kJ/2\alpha\right)r\right)}{n+l+1}\right)^2. \tag{45}$$

Now we may interpret this continuous spectrum of energy with respect to distance as the energy spectrum of massive mediators associated with strong force described by the potential given in Equation (29). When a physical particle is created it is being created continuously until it reaches the size that is required for the system. This process happens in a very short time therefore it seems like an instantaneous creation. In particle physics, the parameter α of the exponential term is expressed in terms of the mass m of a force carrier as $\alpha = mc/2\hbar$. Therefore when the mass of the force carrier is being continuously created the parameter α is being getting larger, at the same time the radius r is also getting bigger, therefore the term $\mathrm{e}^{-2\alpha r} \to 0$ and also the term $\alpha \mathrm{e}^{-2\alpha r} \to 0$. The mass that is accumulated by the force carrier must be supplied by the neutron. When the force carrier with required mass hits the electron, the latter will move further from the proton. On the other hand the MGESCP potential is reduced to the mixed Coulomb-Yukawa potential when the process of creation of the force carrier is complete. This form of potential provides a repulsive force to move the electron away.

As a further remark on the forms of potentials given in Equations (1) and (2), it is seen that the potential given in Equation (2) cannot be reduced to the potential given in Equation (1). And as a consequence the solutions given in Equation (43) cannot be reduced to solutions to a Schrödinger wave equation that uses a potential of the form given in Equation (1). In order to reduce to the potential given in Equation (1) we would need to consider a more general form of potential which can be written as

$$V\left(r\right) = -\alpha\frac{\mathrm{e}^{-\beta r}}{r} + \frac{Q}{r} + K\mathrm{e}^{-\gamma r}. \tag{46}$$

where K, Q, α, β and γ are physical parameters that will need to be determined. This potential would describe a more complete physical process of beta decay when it is applied to the Schrödinger wave equation given in Equation (37). However, whether the Schrödinger wave equation with this form of potential could be solved to obtain exact solutions similar to solutions given in Equation (43) requires more rigorous mathematical investigations.

5. Conclusion

In this work we have discussed a quantum dynamics of Heisenberg's model of the neutron associated with the beta minus decay through the weak and strong interactions in which a neutron may have the structure of a dwarf hydrogen-like

atom. It has been shown that the whole process of beta decay is a complicated physical process that actually undergoes many different physical states of configuration of the system. Therefore, the physical process of beta decay should be described by many different dynamics rather than a single one, only if we can formulate the whole physical process under a mathematical formulation that can give rise to each state by some form of limit associated with mathematical parameters that are used to describe the whole system. For example, a more complete mathematical formulation would require a more general form of potential as given in Equation (46) in Section 4. However, in this work we have still been able to discuss in terms of Schrödinger wave mechanics a quantum dynamics of the neutron as a dwarf hydrogen-like atom using a more complete potential which has been studied and applied to various fields of physics, the so-called the More General Exponential Screened Coulomb Potential (MGESCP). We have shown that the MGESCP potential can be derived from a Dirac-like system of equations which can be reduced from a general system of linear first-order partial differential equations. There is a particular advantage for our approach to deriving a Dirac-like system of equations from a general system of differential equations, that are Dirac-like wavefunctions which can be interpreted according to the purpose of the mathematical investigation of a physical system. They can be used to represent different type of physical objects rather than exclusive mathematical wavefunctions that are used to calculate the probability of the outcome of an experimental result. From the MGESCP potential we have also been able to derive a form of potential that is used to describe interaction between quarks in strong interaction and, in particular, the energy spectrum of the bound state of the dwarf hydrogen-like atom that is continuous with respect to space. This may be a manifestation of a continuous creation of an elementary particle in space. We have also shown that the Yukawa potential can generate and determine the physical shapes of fundamental particles associated with the strong and weak fields. As a consequence, it seems reasonable to suggest that the functional potential in physics may have physical mechanisms to generate mediators of associated physical fields, and these mechanisms can be formulated in terms of differentiable manifolds and their corresponding direct sums of prime manifolds as discussed in our works on the possibility to formulate physics in terms of differential geometry and topology.

Acknowledgements

We would like to thank the reviewers for their critical and constructive comments and we would also like to thank Jane Gao of the administration of JMP for her editorial advice during the preparation of this work.

Conflicts of Interest

The author declares no conflicts of interest regarding the publication of this paper.

References

[1] Schrödinger, E. (1952) *The British Journal for the Philosophy of Science*, **3**, 10. https://doi.org/10.1093/bjps/III.10.109

[2] Bromberg, J. (2013) The Impact of the Neutron: Bohr and Heisenberg. Department of the History and Philosophy of Science, Hebrew University, Jerusalem.

[3] Feynman, R.P. and Gell-Mann, M. (1958) *Physical Review*, **109**, 193. https://doi.org/10.1103/PhysRev.109.193

[4] Yukawa, H. (1935) *Proceedings of the Physico-Mathematical Society of Japan*, **17**, 48.

[5] Ho, V.B. (2016) On the Stationary Orbits of a Hydrogen-Like Atom.

[6] Ho, V.B. (2017) *International Journal of Physics*, **6**, 105-115. https://doi.org/10.12691/ijp-6-4-2

[7] Ikhdair, S.M. and Sever, R. (2016) *Journal of Mathematical Chemistry*, **41**, 343-353. https://doi.org/10.1007/s10910-007-9226-x

[8] Ita, B.I., Louis, H., Akakuru, O.U., Magu, T.O., Joseph, I., Tchoua, P., Amos, P.I., Effiong, I. and Nzeata, N.A. (2018) *Journal of Quantum Information Science*, **8**, 24-45. https://doi.org/10.4236/jqis.2018.81003

[9] Ho, V.B. (2016) Formulating Physics Purely in Terms of Differential Geometry and Topology, Project.

[10] Perkins, D.H. (1987) Introduction to High Energy Physics. Addison-Wesley, Sydney.

[11] Ho, V.B. (2018) *Journal of Modern Physics*, **9**, 2402-2419. https://doi.org/10.4236/jmp.2018.914154

[12] Ho, V.B. (2018) *Global Journal of Science Frontier Research A*, **18**, 37-58.

[13] Melshko, S.V. (2005) Methods for Constructing Exact Solutions of Partial Differential Equations. Springer Science & Business Media, Berlin.

[14] Ho, V.B. (2018) Formulation of Dirac Equation for an Arbitrary Field from a System of Linear First Order Partial Differential Equations.

[15] Dirac, P.A.M. (1928) *Proceedings of the Royal Society A*: *Mathematical, Physical and Engineering Sciences*, **117**, 610-624.

[16] Webdev2.0, Implicit Equations 3d Grapher.

Journal of Modern Physics, 2019, 10, 1083-1089
http://www.scirp.org/journal/jmp
ISSN Online: 2153-120X
ISSN Print: 2153-1196

Predicting Dark Energy Survey Results Using the Flat Space Cosmology Model

Eugene Terry Tatum[1], U. V. S. Seshavatharam[2]

[1]Bowling Green, KY, USA
[2]Honorary Faculty, I-SERVE, Hyderabad, India
Email: ett@twc.com, seshavatharam.uvs@gmail.com

How to cite this paper: Tatum, E.T. and Seshavatharam, U.V.S. (2019) Predicting Dark Energy Survey Results Using the Flat Space Cosmology Model. *Journal of Modern Physics*, **10**, 1083-1089.
https://doi.org/10.4236/jmp.2019.109070

Received: July 12, 2019
Accepted: July 30, 2019
Published: August 2, 2019

Abstract

The Flat Space Cosmology (FSC) model is utilized to show how this model predicts the value of the Hubble parameter at each epoch of cosmic expansion. Specific attention in this paper is given to correlating the observable galactic redshifts since the beginning of the "cosmic dawn" reionization epoch. A graph of the log of the Hubble parameter as a function of redshift z is presented as the FSC prediction of the pending Dark Energy Survey results. In the process, it is discovered that the obvious tension between the SHOES local Hubble constant value and the 2018 Planck Survey and the 2018 Dark Energy Survey global Hubble constant values may be explained by a time-variable, scalar, Hubble parameter acting in accordance with the FSC model.

Keywords

Flat Space Cosmology, Dark Energy, Hubble Parameter, SHOES Hubble Constant, ΛCDM Concordance Model, Cosmology Theory, Early Universe

1. Introduction and Background

The SHOES (Supernovae, H_0, for the Equation of State of dark energy) report [1] of a "best estimate" local Hubble constant value of 73.24 ± 1.74 km·s^{-1}·Mpc^{-1} is in tension with the global Hubble constant estimates of 67.36 ± 0.54 km·s^{-1}·Mpc^{-1} and 67.77 ± 1.30 km·s^{-1}·Mpc^{-1} reported by the 2018 Planck Survey [2] and 2018 Dark Energy Survey (DES) [3] collaborations, respectively. Given these dramatically different results (at 3.4σ) between measurements of local and global values, one wonders if what most cosmologists prefer to call the Hubble *constant* is actually a time-variable, scalar, Hubble *parameter*. In the next few years, this question is likely to be resolved by earth and space-based telescopes and wide-field cameras in conjunction with 3D computer simulations of the time evolution of

our expanding universe. Ideally, we hope to learn the value of the Hubble parameter at each point in cosmic time beginning with the "cosmic dawn" epoch.

At present, the ΛCDM concordance model of cosmology is only seriously challenged by one other type of model, the $R_h = ct$ model. This type of model was introduced by Fulvio Melia in 2012 [4] and several similar models of this type soon followed. Perhaps the most successful of these models, in terms of observational correlations and predictions, is Flat Space Cosmology (FSC) [5] [6] [7] [8] [9]. The interested reader should start with a recent FSC summary paper [10], which shows how its predictive capacity and falsifiability make it preferable in many ways to the ΛCDM concordance model. To date, none of the many *global* predictions of the time-varying FSC model parameters (Hubble parameter, radius, mass, energy, entropy, average temperature, temperature anisotropy, *etc.*) have been falsified. One of the important ways in which the FSC model is superior to the ΛCDM concordance model is in its *predictive* capacity with respect to calculating the value of the Hubble parameter at every second of cosmic evolution from the Planck-scale epoch. FSC since its inception in 2015, for instance, has predicted a current global Hubble parameter value of 66.893 $\text{km}\cdot\text{s}^{-1}\cdot\text{Mpc}^{-1}$, which fits the measured 2018 Planck and 2018 DES values given above. This FSC value also fits the 66.93 ± 0.62 $\text{km}\cdot\text{s}^{-1}\cdot\text{Mpc}^{-1}$ value predicted by ΛCDM with 3 neutrino flavors having a mass of 0.06 eV.

It is the purpose of this paper to show how the FSC model, since its inception, has provided a means to calculate the Hubble parameter values correlating with every cosmic redshift epoch since "cosmic dawn".

2. Results

The relevant FSC equations useful for these calculations include:

$$z \cong \left(\frac{T_t^2}{T_o^2} - 1\right)^{1/2} \tag{1}$$

$$T_t^2 R_t \cong 1.027246639815497 \times 10^{27}\,\text{K}^2\cdot\text{m} \tag{2}$$

It is trivial to show how Equations (1) and (2), in conjunction with the FSC Hubble parameter definition ($H_t = c/R_t$), can be rearranged and undergo substitution to give:

$$T_0^2\left(z^2+1\right) \cong H_t\left[\frac{1.027246639815497\times 10^{27}\,\text{K}^2\cdot\text{m}}{c}\right] \tag{3}$$

For ease of comparison, the value of the time-dependent Hubble parameter H_t in reciprocal seconds (s^{-1}) can be multiplied by $3.08567758 \times 10^{19}$ $\text{km}\cdot\text{Mpc}^{-1}$ to convert H_t to its conventional $\text{km}\cdot\text{s}^{-1}\cdot\text{Mpc}^{-1}$ units. To accomplish this, the left-hand term in (3) is multiplied by this factor. One can now use the following equation to compare redshift z values with H_t values in $\text{km}\cdot\text{s}^{-1}\cdot\text{Mpc}^{-1}$:

$$\begin{aligned} &T_0^2\left(z^2+1\right)\left(3.08567758\times 10^{19}\,\text{km}\cdot\text{Mpc}^{-1}\right) \\ &\cong H_t\left[\frac{1.027246639815497\times 10^{27}\,\text{K}^2\cdot\text{m}}{c}\right] \end{aligned} \tag{4}$$

Taking the square root of both sides of (4) gives:

$$\left(z^2+1\right)^{1/2} \cong \left[H_t\right]^{1/2}\left[\frac{1.027246639815497\times10^{27}\,\mathrm{K}^2\cdot\mathrm{m}}{cT_0^2\left(3.08567758\times10^{19}\ \mathrm{km}\cdot\mathrm{Mpc}^{-1}\right)}\right]^{1/2} \tag{5}$$

Using the $z+1$ convention for redshift, this approximates to:

$$z+1 \cong 0.122\sqrt{H_t} \tag{6}$$

One can then use the knowledge that today's FSC Hubble parameter value of 66.893 $\mathrm{km\cdot s^{-1}\cdot Mpc^{-1}}$ corresponds to 14.617 billion years of current cosmic age in order to calculate Hubble parameters at every billion-year interval of cosmic age. The following equation is useful in this regard:

$$H_t \cong H_0\left(\frac{14.617}{t}\right) \tag{7}$$

where the t value is simply the integer, or fractional number, of billions of years of cosmic age, and H_0 = 66.893 $\mathrm{km\cdot s^{-1}\cdot Mpc^{-1}}$.

One can then construct the following table (Table 1) of FSC Hubble parameter values corresponding to redshift z values varying from $z = 0$ (corresponding to today's observed global Hubble parameter value) to z = 11.09 (for the epoch of the highest-redshift galaxy yet observed).

Table 1. Cosmic age, redshift z, Hubble parameter, $\mathrm{Log_{10}}$ Hubble parameter.

Cosmic Age (Gyrs)	Redshift z	H_t ($\mathrm{km\cdot s^{-1}\cdot Mpc^{-1}}$)	$\mathrm{Log_{10}}(H_t)$
14.617	0.00	66.893	1.83
14	0.02	69.84	1.84
13	0.06	75.21	1.88
12	0.10	81.48	1.91
11	0.15	88.89	1.95
10	0.21	97.78	1.99
9	0.27	108.64	2.04
8	0.35	122.22	2.09
7	0.44	139.68	2.15
6	0.56	162.96	2.21
5	0.71	195.55	2.29
4	0.91	244.44	2.39
3	1.20	325.92	2.51
2	1.70	488.89	2.69
1	2.81	977.77	2.99
0.5	4.40	1955.55	3.29
0.25	6.63	3911.1	3.59
0.142	9.11	6868.25	3.84
0.0996	11.09	9820.49	3.99

The results shown in Table 1 can be used to present a graph (Figure 1) of $\log_{10}(H_t)$ as a function of redshift z.

3. Discussion

The FSC publication entitled, "Temperature Scaling in Flat Space Cosmology in Comparison to Standard Cosmology" [11] makes note of the fact that the temperature curves of FSC and ΛCDM cosmology are somewhat different, particularly in the first billion years or so of cosmic evolution. This is a function of the embedded FSC scaling thermodynamic equation. A graph (Figure 2) from the temperature scaling paper is reproduced herein.

The blue line is the radiation temperature (T_R) curve expected in the ΛCDM concordance model and the green line is the radiation temperature curve expected in FSC. The dashed red line represents the measured and projected spin temperature (T_S) and the solid red line represents the baryonic gas temperature

Figure 1. $\text{Log}_{10}(H_t)$ as a function of redshift z.

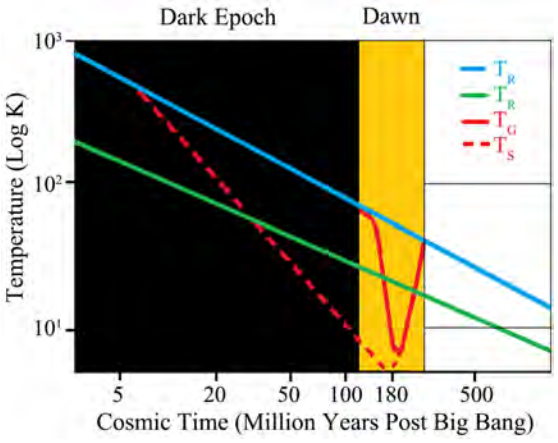

Figure 2. Cosmic temperature vs cosmic age in ΛCDM (blue) and FSC (red).

(T_G). In Figure 2, the concordance model temperature curve, as well as the concordance model conception of the time scale at which "cosmic dawn" occurred is presented as seen in Bowman's publication [12] on the recent redshifted 21-cm observations. One should note that, in the FSC model, the same radiation temperatures and redshift z values correlating to "cosmic dawn" occurred at about 20 - 60 million years after the Planck epoch, as opposed to approximately 110 - 250 million years in the concordance model. As discussed in recent FSC papers (see references [10] and [11]), the FSC model allows for earlier galaxy formation by several hundred million years in comparison to the concordance model. Thus, the FSC model, by its significantly *colder* temperature curve in the first billion years, offers a solution to the "The Impossibly Early Galaxy Problem" described by Steinhardt [13].

Of most importance with respect to the stated purpose of this paper, one can now see that the FSC model makes very specific predictions for the Hubble parameter values correlating with the range of currently observable galactic redshifts. The following major points need to be stressed:

1) As is true for all $R_h = ct$ models, the FSC Hubble parameter is *scalar* over the great span of cosmic time. $R_h = ct$ models require that the Hubble parameter value be defined according to $H_t = c/R_t$, where c is the speed of light and R_t is the Hubble radius at any time t. Thus, while at any point in human time spans the Hubble parameter may appear to be a constant, any cosmic model which incorporates c/R_t within its Hubble parameter equation *stipulates* that the Hubble term is not a true constant over the great span of cosmic time.

2) The SHOES study of the "local" Hubble constant measured galactic separation velocities per megaparsec at earlier cosmic times corresponding to a range of redshift z values of less than 0.15. It is interesting to note that their averaged "outlier" Hubble constant value corresponds roughly with the FSC Hubble parameter value correlated to a redshift z value of 0.06 (see Table 1). Moreover, when the Milky Way was used as a sole anchor for these observations, the SHOES study H_0 value of 76.18 ± 2.37 km·s^{-1}·Mpc^{-1} can be seen to fit the middle of the $0 < z < 0.15$ range of our Figure 1 curve. The $\log_{10}(76.18)$ is 1.88. *This may be more readily apparent if one compares the first five entries in* Table 1. Similar adopted zero point measurements of Hubble parameters corresponding to higher z value ranges are fully expected by these authors to correlate with higher sections of Figure 1 curve. If so, then modern cosmologists will soon accept the idea of a time-variable, scalar, Hubble parameter.

3) Table 1 and Figure 1 show very specific *predictions* of the FSC model awaiting confirmation or refutation within the next few years of observations. If these observations prove that the Hubble parameter has a radically different temporal history than predicted herein, the FSC model and any similar $R_h = ct$ models would then be falsified. On the other hand, if observations in the next few years fit with Table 1 and Figure 1, the temporal behavior of dark energy would be better understood using the FSC model. In such case, the FSC model

might then become the new concordance model.

4. Summary and Conclusions

The heuristic FSC $R_h = ct$ cosmology model is utilized to evaluate the tension between the SHOES local Hubble constant value and the Planck Survey and Dark Energy Survey global values. The SHOES report looked at a specific redshift z range of $0 < z < 0.15$. Thus, the first approximately 11 billion years of the cosmic expansion history was not subjected to their analysis.

In the FSC model, the Hubble parameter is defined according to $H_t = c/R_t$. Therefore, the FSC Hubble parameter is time-variable and scalar according to Table 1 and Figure 1. The FSC model predicts that the middle of the range of $0 < z < 0.15$ should correlate with a Hubble parameter value of approximately 75 $km \cdot s^{-1} \cdot Mpc^{-1}$, which fits the SHOES Hubble constant determination of 76.18 ± 2.37 for the part of their study using the Milky Way as their anchor galaxy.

The authors predict that, in the next few years, similar measurements corresponding to higher z value ranges will correlate with higher sections of Figure 1 curve. If this proves to be the case, then modern cosmologists will have to accept that what is currently called a Hubble constant is actually a time-variable, scalar, Hubble parameter. Furthermore, such a result would likely establish FSC as the new concordance model.

Dedications and Acknowledgements

This paper is dedicated to Dr. Stephen Hawking and Dr. Roger Penrose for their groundbreaking work on black holes and their possible application to cosmology. Dr. Tatum also thanks Dr. Rudolph Schild of the Harvard-Smithsonian Center for Astrophysics for his past support and encouragement. Author Seshavatharam UVS is indebted to professors Brahmashri M. Nagaphani Sarma, Chairman, Shri K.V. Krishna Murthy, founding Chairman, Institute of Scientific Research in Vedas (I-SERVE), Hyderabad, India, and to Shri K.V.R.S. Murthy, former scientist IICT (CSIR), Govt. of India, Director, Research and Development, I-SERVE, for their valuable guidance and great support in developing this subject.

Conflicts of Interest

The authors declare no conflicts of interest regarding the publication of this paper.

References

[1] Reiss, A.G., *et al.* (2016) *The Astrophysical Journal*, **826**, 56. https://doi.org/10.3847/0004-637X/826/1/56

[2] Aghanim, N., *et al.* (2018) Planck 2018 Results VI. Cosmological Parameters.

[3] Macaulay, E., *et al.* (2018) *Monthly Notices of the Royal Astronomical Society*, **486**, 2184-2196.

[4] Melia, F. and Shevchuk, A.S. (2012) *Monthly Notices of the Royal Astronomical Society*, **419**, 2579-2586. https://doi.org/10.1111/j.1365-2966.2011.19906.x

[5] Tatum, E.T., Seshavatharam, U.V.S. and Lakshminarayana, S. (2015) *International Journal of Astronomy and Astrophysics*, **5**, 116-124. https://doi.org/10.4236/ijaa.2015.52015

[6] Tatum, E.T., Seshavatharam, U.V.S. and Lakshminarayana, S. (2015) *Journal of Applied Physical Science International*, **4**, 18-26.

[7] Tatum, E.T., Seshavatharam, U.V.S. and Lakshminarayana, S. (2015) *Frontiers of Astronomy, Astrophysics and Cosmology*, **1**, 98-104.

[8] Tatum, E.T. and Seshavatharam, U.V.S. (2018) *Journal of Modern Physics*, **9**, 2008-2020. https://doi.org/10.4236/jmp.2018.910126

[9] Tatum, E.T. and Seshavatharam, U.V.S. (2018) *Journal of Modern Physics*, **9**, 1469-1483. https://doi.org/10.4236/jmp.2018.98091

[10] Tatum, E.T. (2018) *Journal of Modern Physics*, **9**, 1867-1882. https://doi.org/10.4236/jmp.2018.910118

[11] Tatum, E.T. and Seshavatharam, U.V.S. (2018) *Journal of Modern Physics*, **9**, 1404-1414. https://doi.org/10.4236/jmp.2018.97085

[12] Bowman, J.D. (2018) *Nature*, **555**, 67-70. https://doi.org/10.1038/nature25792

[13] Steinhardt, C.L., *et al.* (2015) *The Astrophysical Journal*, **824**, 21. https://doi.org/10.3847/0004-637X/824/1/21

Journal of Modern Physics, 2019, 10, 1090-1124
http://www.scirp.org/journal/jmp
ISSN Online: 2153-120X
ISSN Print: 2153-1196

An Analysis of the Origin of the Interaction Force between Electric Charges, including Justification of the ln*r* Term in the Completed Coulomb's Law, in HM16 Ether

Ioan Has[1], Simona Miclaus[1], Aurelian Has[2]

[1]Land Forces Academy "Nicolae Balcescu", Sibiu, Romania
[2]Independent Researcher, Rm. Valcea, Romania
Email: hasavo@yahoo.com, simo.miclaus@gmail.com, hasaurelian@yahoo.com

How to cite this paper: Has, I., Miclaus, S. and Has, A. (2019) An Analysis of the Origin of the Interaction Force between Electric Charges, including Justification of the ln*r* Term in the Completed Coulomb's Law, in HM16 Ether. *Journal of Modern Physics*, **10**, 1090-1124.
https://doi.org/10.4236/jmp.2019.109071

Received: July 5, 2019
Accepted: August 3, 2019
Published: August 6, 2019

Abstract

In this study, we demonstrate the correctness of our 2010 hypothesis regarding the need to complete Coulomb's F_C law with the term ln*r*, resulting in the completed F_{CC} force. For this purpose, we consider the electrical interactions between charged microparticles (MPs), which develop as fundamental vibrations (FVs) in ether, producing the vibrational strains ε and γ and the resulting stresses σ and τ, as percussions of ether cells (ECs) upon the MP surface. The stresses σ and τ produce a resultant force F_P, due to the percussions which constitute the real electric force F_{CC}. The spatial effect of ether on F_P is demonstrated by an analytical method, considering the electrical interaction between MPs through various equidistant spatial paths l_i of FVs, modelled on the basis of the Huygens principle for waves. For this issue, we utilized a numerical calculation, which could be generalized. But this spatial effect of the ether leads at a very slow decreasing of the F_P forces ratio r_F when doubling the distance l, in contrast to Coulomb's F_C forces whose ratio r_F decreases accentuate with doubling l. Accordingly, the necessity of including the term ln r in the F_{CC} force, which is limited to 1.0 for doubling l, at long distances, was justified.

Keywords

Nature of Electric Charges, Constitution of Microparticles, Calculus of Electric Forces from Percussions Forces, HM16 Model of Ether with Fundamental Vibrations, Completed Coulomb Law Justification

1. Introduction

The HM16 ether model, originally proposed by the present authors in 2016 [1], will be the starting point for the present analysis, which will provide new developments in the model in terms of the composition, and behaviour and effect of ether in nature and in physics.

We consider in our HM16 model that in nature, all microparticles (MPs) have either a positive or a negative electric charge, denoted MP^+ and MP^-. However, in the general case in which the MP sign (+ or −) is not important, we will utilize the simple notation MP in the text, for both MP^+ and MP^-. In addition, it is accepted in physics that at the macro scale, MP^+ and MP^- are in parity, or even in pairs, and matter is neutral in nature.

To date, in physics, the nature of positive $+q$ and negative $-q$ electric charges has been neither defined nor explained. Furthermore, it has not been justified physically and materially.

In the following sections, we will initially present the modelling of the physical nature of the electric charge by highlighting new properties of the HM16 model of ether and of MPs, related to electric charges.

The paper brings in some novelties, such as the mechanical percussion nature of corrected electric forces F_{CC}, or the many simultaneous paths in ether of electric force F_{CC} transmission from close to closer distances, in contrast to the classical Coulomb force F_C transmitted at a distance.

The main new contribution of the paper is the analytical demonstration that the F_{CC} forces decrease very slow with the distance l, thus justifying the new term $\ln r$, in contrast to the classical Coulomb force F_C which decreases with distance.

But this spatial effect of the ether leads at a limit to 1.0 in the decrease of the F_P forces ratio when doubling the distance l, in contrast to Coulomb's F_C forces whose ratio decreases to 0.25 with doubling l.

Accordingly, the necessity of including the term $\ln r$ in the F_{CC} force, which too is capped to 1.0 for doubling l, at long distances, was demonstrated.

In all the following graphical representations of space filled with ether, we will also indicate the indispensable reference frame (RF), usually as a Cartesian *Oxyz* frame, attached to a certain MP immovable in ether or to a certain cell of the ether (EC). Hence any *Oxyz* frame will be an absolute RF, referring to the ether.

2. Origin of the Interaction Force between Microparticles with Electric Charges MP^+ and MP^- in the Case of the HM16 Ether Model

Since we admit that the electric charge is intimately linked to MPs, the electric charge can be explained by the composition and functioning of MPs in the HM16 ether model.

In the following analysis, we will utilize the same abbreviations used in [1], which will be redefined in this section as follows.

HM16 is our ether model initiated in 2016, MP stands for microparticle, SMP

for submicroparticle, ESMP for a especial submicroparticle, RF for the reference frame, EC for ether cells, EP for etheron particles, FV for fundamental vibrations in ether, PV for particle vibrations, MB for a material body, F_{CC} for the corrected/completed Coulomb force, F_C for the classical Coulomb electric force, p_i for individual percussion forces, f_i for continue force from percussions, F_P for the resultant percussion force, F_N for the classical Newtonian gravitational force, F_{DC} for the force between two electrical dipoles, r_F for F_s forces ratio at doubled distances, ε and γ for linear and angular deformations/strains and σ and τ for normal and tangential efforts/stresses;

An MP which is currently considered electrically neutral, such as a neutron, in fact comprises the MPs (or submicroparticles (SMPs)) MP^+ and MP^-, with compensatory positive $(+q)$ and negative $(-q)$ electric charges, resulting in the common neutral bodies. In the following text, charge refers only to electric charge.

A first variant of the mode of operation of MPs considers the Type A HM16 ether model in terms of the crystalline disposition of etherons, as defined in [1], in which the specific vibrational/vortex model of an MP is considered as a basic phenomenon which transmits its vibrations to the surrounding crystalline network of etherons and accordingly, to other MPs (**Figure 1**).

A second variant of MPs' mode of operation is given by the Type B HM16 model of ether, in the form of a fluid as defined in [1], in which the flow/circulation of etheron particles (EPs) between different MPs occurs during the absorption or emission of ether particles or ether cells (ECs) by any MP. The $+q$ and $-q$ electric charges are given here by the debit of the fluid emitted or absorbed by specific MPs.

The Type A HM16 ether model is the main focus of the present analysis.

Of course, the detailed mechanisms developed between ether components and the forces acting between MPs, which will be presented and utilized in the next part of this paper, are only hypothesized, because until now it has not been possible to observe or directly measure them at their very small scale.

However, our HM16 ether model and its functioning is based on, and is in agreement with, actual existing experimental data from physics concerning the behaviour of matter and radiation at an observable scale.

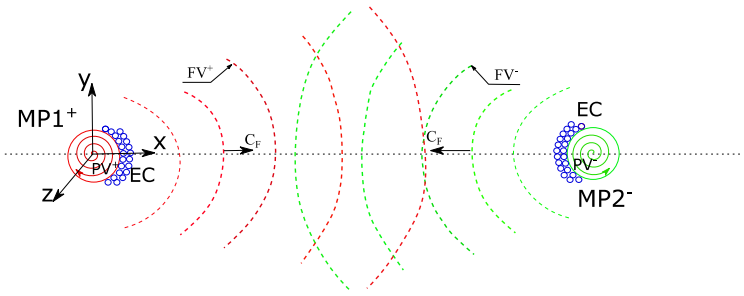

Figure 1. Interaction between $MP1^+$ and $MP2^-$ through the transmission of fundamental vibrations (FVs) in the *Oxyz* reference frame attached to the immovable MP1.

Any such hypothesis will be confirmed in physics, when the results correspond to the real behaviour of matter and to the structure/composition of radiation at an observable scale.

Furthermore, as the purpose of this study, we will show that the results yielded by our HM16B model will be in accordance with the results of physical experiments. Accordingly, our initial hypothesis concerning the HM16 ether model will be confirmed.

It should be noted, as in [1], that the first-order components of HM16 ether, namely the ether particles themselves, are of two types: EPα and EPβ. These are the α and β etherons, which are grouped into the elemental cells (ECs) of ether, with at least four etherons (tetrahedrons) or as is more justified by volume symmetry, with eight etherons (cubes).

Ether is considered to be in its natural, undisturbed state, thus presenting no deformations/displacements but containing the fundamental vibrations (FVs) induced by all existing MPs, which are considered immobile/fixed in space at the starting moment of any analysis.

We acknowledge that the MPs in ether constitute physical support for the electric charges $+q$ and $-q$ and we refer to them as MP^+ and MP^- respectively.

Firstly, in the HM16 ether model, any MP^+ or MP^- contains a group of vibrating EPs or ECs exhibiting their own PV^+ or PV^- vibrations, with their specific sign pattern (+/−) and with their own frequency ω, where PV signifies an internal particle vibration (**Figure 1**).

Furthermore, the different actions of PV^+ and PV^- produced by MP^+ and MP^- respectively, create corresponding FVs in the surrounding ether, *i.e.* FV^+ and FV^-.

Any MP1 will produce its own FVs in ether, which travel away from the MP1 (**Figure 1**) and are eventually transmitted to all the other MPs in the ether from across the universe, according to the Huygens principle for vibrations.

We should state that, similarly to the claims made in section III of [1], the FVs of the HM16 ether comprise the linear specific (unitary) deformations ε and the angular specific (unitary) distortions γ, of the crystalline spatial net of ECs. Both ε and γ are periodic or pulsatory deformations, with frequency ν corresponding to the pulsation ω of the MPs' rotations or oscillations. These specific deformations ε and γ of a body, are known in mechanics as strains.

In the present analysis, we will discuss only the plane problem of deformations or of the strains ε and γ. Although in the general analysis of the HM16 ether model we are dealing with a spatial problem, in which the plane deformations ε and γ are replaced by the three-dimensional spatial tensors of deformations $\boldsymbol{\varepsilon}$ and $\boldsymbol{\gamma}$, this does not diminish the utility of studying the plane problem, which can then be generalized.

These vibrations in ether FV^+ and FV^- will create the effect and mode of interaction between MPs, as the electrical forces, which are specific to MP^+ and different to MP^- (**Figure 2**).

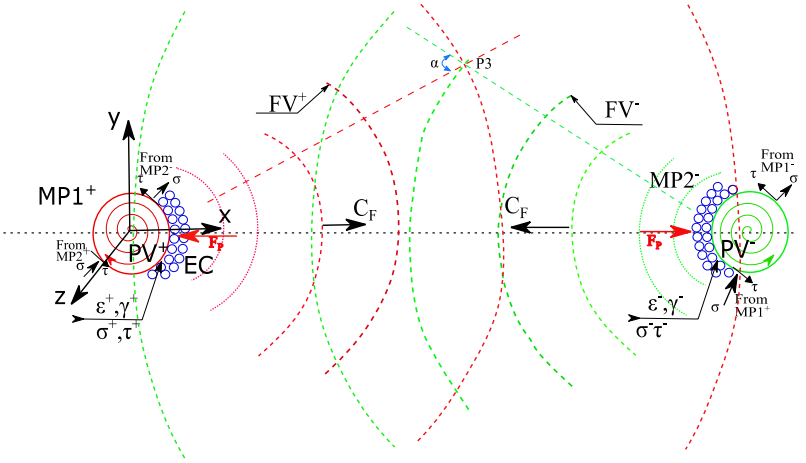

Figure 2. The emergence of the F_p force between $MP1^+$ and $MP2^-$ created by the σ and τ stresses, through the transmission of the FVs with the ε and γ strains, in the *Oxyz* reference frame attached to the immovable MP1.

This difference in the behaviour of MP^+ and MP^- may, in principle, be manifested by the sense of the ε deformation (elongation $+\varepsilon$ or compression $-\varepsilon$) and by the sense of the γ rotation (clockwise $+\gamma$ or anticlockwise $-\gamma$), which are deformations produced in the ether's spatial net of ECs, under the effect of FV^+ and FV^- as created by MP^+ or MP^-.

This specific behaviour of MP^+ or MP^- is illustrated in **Figure 3**, which presents MP^+ and MP^- disposed in opposition on a principal diagonal D1, *i.e.* in the two opposing quadrants of a Cartesian *Oxyz* reference system.

There, MP^+ manifests its own vibrations PV^+, with a frequency ν (or pulsation ω) consisting of strain couples $+\varepsilon$ and $+\gamma$ along +D1, and similarly MP^- manifests its own PV^- consisting of the strain couples $+\varepsilon$ and $-\gamma$ along +D1 (or couples $-\varepsilon$ and $+\gamma$ along D1) (**Figure 3**).

Then, MPs in contact with surrounding ECs will transmit and create FVs, via their own PVs.

The FVs in the ether are also of two types: FV^+ representing strain couples with the same sign ($+\varepsilon$ and $+\gamma$ or $-\varepsilon$ and $-\gamma$) and FV^- representing strain pairs with opposite sign ($+\varepsilon$ and $-\gamma$ or $-\varepsilon$ and $+\gamma$).

Accordingly, in the HM16 ether model, the specific properties of electric charges $+q$ and $-q$ are intrinsically attached to MP^+ and to MP^- by their specific mode of vibration PV^+ or PV^- manifested mechanically.

The detailed mechanics of PVs (as oscillations, vortexes or other kinds of movements) is not yet known, but it is not strictly necessary here.

Concerning the mechanism of the transmission of vibrations of the electrical force F_{CC} between electrically charged MPs via the ether, we advance here a hypothesis regarding the manifestation and continuous action of percussion forces p_i between the involved physical objects considered to be in direct contact (MPs, ECs), in which force transmissions are produced from close to closer distances (and not at a distance), as will be presented in the next section of this paper.

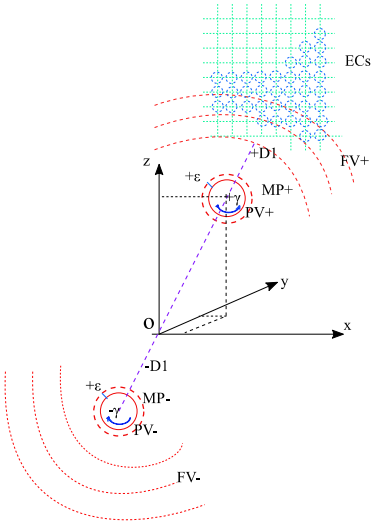

Figure 3. The manifestation of the charged MP^+ and MP^-, creating the specific vibrations FV^+ and FV^- in ECs, acting upon any MPs, creating the ε and γ strains and giving percussions p_p in the *Oxyz* reference frame attached to an EC.

If an MP1 is present at a point in the ether and an MP2 is found in the area (**Figure 2**), the MP2 will be subjected over its entire external surface to a contact of FVs through the ECs, caused by MP1.

This contact action appears because the vibrating ECs of ether, around MP2, have direct contact with the MP2 surface and as such will create normal stresses σ (two−way stresses, *i.e.* $-\sigma$ compression and $+\sigma$ stretching) and tangential stresses τ (with two senses $+\tau$ and $-\tau$) over the entire surface of the MP2 (**Figure 2**), with a resultant force $+f$ or $-f$ upon a unit area. Obviously, the phenomenon is similar for MP1 when the cause is an MP2.

In HM16, FVs caused by an MP^+ will create vectors (tensors in 3D) of the stresses σ and τ (or of the resultant force *f*) on the unit surface of an MP, disposed in the opposite directions to the σ and τ stresses (or force *f*) caused on the same MP unit surface by an MP^-.

Adding the two types of stress vectors (tensors) σ and τ (or the resultant *f*) upon the whole surface of an MP will result in a $+F$ force of attraction or a $-F$ force of repulsion (**Figure 2**, **Figure 3**) between the two types of MPs, depending on whether they have identical or opposite electric charges $+q$ or $-q$.

Accordingly, in HM16, in the presence of MP^+ (**Figure 2**, **Figure 3**), the vectors of the strains ε and γ produced in the ether, as well as the resultant vectors of the stresses σ and τ (or resultant *f*) acting on the MP^- surface, will have opposite senses, resulting in an attraction force $+F$ on this MP^-, while the same $+F$ force will be simultaneously applied to the MP^+.

Regarding the resultant force caused by vibrational waves starting from two MPs of the same sign (MP^+ and MP^+ or MP^- and MP^-), the vectors of the strains ε and γ and the vectors of the stresses σ and τ (or resultant *f*) will have the same senses (**Figure 2**, **Figure 3**). In turn, there will be a repulsive force $-F$ on the

second MP (MP^+/MP^-), while the same repulsive force $-F$ will appear on the first MP at the same time.

Consequently, the difference in the behaviour of interactions between MP^- and MP^+ is manifested according to the above presentation.

However, it is possible that between MPs of the same sign, attraction forces arise (and between the MPs of opposite signs, repulsion forces appear) according to the completed law of F_{CC} force [2]. For these forces, there will be different formulas, that depend on the distance l_i between the MPs or between the material bodies (MBs).

However, these interaction forces, having the opposite sense to those usually currently considered, will not change the physical behaviour of the MPs, which possess a property equivalent to the actual sign of the electric charge.

The above presentation can be considered to be the mechanism of the appearance and manifestation of electric charges $+q$ and $-q$. They are, in fact, intrinsic properties of MPs and of the ether.

MPs^+ and MPs^- produce in ether some specific FV^+ or FV^- which acts upon other MPs^- and MPs^+. Depending on these FVs, the interaction force F_{CC} results between MPs.

Today, in physics, the Coulomb force F_C is considered to be a manifestation of interaction at distance between the so-called electric charges $+q$ and $-q$. However, these charges do not exist as physical entities, only as manifestations of specific vibrations of MPs and of the HM16 ether model (**Figure 3**).

Note that the sense of the F_{DC} force between two electric dipoles will always be attraction [2], resulting in a gravitational pull exerted by the F_{DC} via the corrected F_{CC} force given in Euation (21) in [3].

3. The Occurrence Mode of the Interaction Force between Charged Microparticles in the Case of Type A HM16 Ether

To the best of our knowledge, in no classical analysis of electricity [4] [5] [6] [7] [8] is there any discussion of the possibility that the Coulomb forces F_C could, in fact, be the result of the unitary forces σ or τ, which might act on the surface of MPs due to ε or γ deformations of the ether.

We note that in the classical approach, considering the Coulomb electric interaction between two MBs or MPs endowed with electric charges $\pm q$, only the existence of concentrated F_C forces of the Coulomb type are acknowledged.

It is also classically understood that F_C forces appear and act at a distance instantly and mutually between MB1 and MB2, with the sense of the action provided by the electric charge signs $\pm q$. The F_C force is considered to be a linear, one-directional vector, which is transmitted directly on a straight line between MB1 and MB2.

We observe that, similar to the case of the electric force, in the case of Newtonian gravitational interaction, the gravitational force F_N is classically considered to act between two MBs. It is acknowledged that the force F_N is also a focused

force, the size of which is a function of the masses m of the bodies and of the distance $1/r^2$ [7] [8].

However, in our analysis of the presence of HM16 ether, we consider that the cause of F_C forces is the appearance of the unitary stresses σ and τ acting on the entire surface of an MP2 (Figure 2). Furthermore, the σ and τ stresses do not occur instantly at a distance but are the result of the specific ε and γ deformations of the ECs around the MP2. In addition, ε, γ strains are produced by FVs from ether, caused by the PVs vibrating permanently inside the corresponding MP1, whose strains ε and γ are permanently transmitted by the MP1 directly to the ether as FVs.

In this case, in the presence of HM16 FVs in the ether, they neither occur nor are transmitted between MP1 and MP2 in the form of a single straight vector of the F_C type. In fact, these fundamental waves/FVs are transmitted in the form of a spatial phenomenon, which is present around any MP in the form of spatial vibrations/waves advancing from MP1 in all directions in space at a speed c_f (Figure 2). The FVs are transmitted through the material structure as ECs of the HM16 ether, starting from any existing MP_i and continuing according to the Huygens principle into the whole ether present in the whole of space, which in this case is considered to be Euclidean space.

Moreover, the classical transmission of F_C as a linear vector from MP1 directly to the destination (MP2) cannot occur, because it is highly likely that the F_C straight line will encounter another MP, or even several MPs, existing in any MBs. Furthermore, such a classical type straightforward F_C force in the form of a straight line (linear vector) cannot bypass an obstacle, or even an MP. As a result of bypassing an MB, the F_C force can no longer be considered to be a linear vector or a straight line.

Due to the above situation, the spatial transmission of F_{CC} in the form of spatial FVs, in terms of ether volume, prompts an additional argument.

In fact, the ε and γ deformations of the ether acting on MP2 are caused by the corresponding MP1 itself. Furthermore, MP1 is in an area of the ether where a quantity of energy (ΔE) has accumulated, which is manifested in the production of its own PVs as vortexes/oscillations in the EC group in the volume of the MP1 (Figures 1-3).

These PV vibrations in the EC group constituting the MP1 may in fact be periodic deformations (or even rotations/whirlpools) inside these ECs from MP1, of type ε_p and γ_p and with frequency ω (Figures 1-3). They are similar to the two types of specific deformations in compact MBs, known in mechanics as ε_m and γ_m. However, ε_p and γ_p do not transmit energy like ε_m and γ_m, owing to the ether's special (ideal) properties.

Meanwhile, MP1, by being in intimate contact with ether, precisely conveys its vibrations to it as ε_p and γ_p deformations, which will create periodic ε and γ deformations in the ECs of the adjacent ether (Figure 2, Figure 3). The ε and γ deformations of ether will have an amplitude that may be different from that of

ε_p and γ_p from the MP, but they will have their own preserved frequency ω across the entire network of the surrounding ECs.

It follows that these ε and γ deformations in the whole EC network are continuously present over time, as long as there exists an MP1 at their origin and no energy consumption/transmission is involved. In addition, these ε and γ deformations in ether can only be transmitted from near to near in the whole three-dimensional ether network, with a fundamental speed c_f given by ether's physical properties. These properties are currently unknown, but we only can suppose they are the properties of an ideal body having an extremely high modulus E and an extremely low density ρ, consequently resulting in a wave speed c_f that is extremely high, in our estimate.

At the same time, it is likely that in the fixed ether cell/particle (EC/EP) network, ε and γ deformations can only be produced in quantum terms, by altering the positions of ECs/EPs in the ether only in jumps of Δx, Δy and Δz. These jumps can only take place between fixed EC/EP positions in the primary ether network (**Figure 2**, **Figure 3**), or possibly between intermediate positions in the second−order ether network [1].

Such a primary network is considered to be fixed, with stable EC positions in space, including in the fixed *Oxyz* reference frame (**Figure 2**, **Figure 3**), and permanent in time if disturbing factors do not occur.

Now, we consider such an etheric network with a given point P2, situated upon an MP2 surface (**Figure 2**). At time t at P2, the FVs arise from one, two or more sources (MP1a, MP1b, MP1c, etc.), located in the area in approximately the same direction (**Figure 2**). Then, local vibrational deformations ε and $\gamma(\omega)$ of the ether will appear at P2. At the point P2 at which these vibrations arrive on the MP2 surface, we can say that the FVs have reached their end point or terminus point. Here, the interesting, useful deformations ε and $\gamma(\omega)$ can only be those in the last layer of ECs in direct contact with the surface of the MP2, caused by all MP1s existing in the considered direction (**Figure 2**).

The P2 terminus point of the FVs' vibration paths can only be located at the point of contact of FV1 with an MP2 surface. For the MP2, the effect of the ε and $\gamma(\omega)$ deformations in the surrounding ether will be manifested by the MP2's own EC deformations, *i.e.*, ε_p and γ_p. These deformations imply a modification of the stress distribution σ, τ on the surface of the MP2, resulting in the F_p type of interaction force described in Section 4, as a result of these stresses. Note that this F_p force is the effect of FV1 through σ and τ, appearing on the entire outer surface of the MP2.

However, if the point P3 is located anywhere in the ether network in an area in which there is no MP (**Figure 2**), the path of FV1 will not have P3 as an end point, and so the FV1 waves will continue beyond P3. Beyond P3, there will be a continuation of the FV1 vibration transmission and of the ε and $\gamma(\omega)$ ether deformation. Accordingly, at the P3 point, there is no longer an end-point effect of the deformation, as in the case of P2.

Meanwhile, at the P3 point, which is not a terminus point, the continuation of the waveform path of FVs and the ε and $\gamma(\omega)$ deformations of ether can be pursued according to the Huygens principle, which also applies to ether, as shown in Section 5.

This is because the ether constitutes a special, albeit material, structure, present in all space, so that anywhere there is a P3 free point, where an FV1 arrives, the Huygens principle of waves can be applied [7] [8]. According to the Huygens principle, the point P3 becomes a source of a secondary vibration FV1' of the ether, which has the same nature as FV1 but moves only in the forward direction.

However, if at the point P3 a second vibration FV2 arrives concomitantly with FV1, the travel direction of which makes an angle α with the direction of FV1 (**Figure 2**), it is logical that in P3, a certain effect or phenomenon of special interference of the Huygens type appears, in which both FV1 and FV2 will have an effect upon the ether, as will be shown in Section 4.

4. Mechanism of the Occurrence and Calculation of the F_P Force between the Considered Electrically Charged Microparticles, by a Real Interaction Force as a Result of Ether Percussions

The FVs produced by all other MPs in the ether of the universe, including those of MP1 (**Figures 1-3**), act upon MP2.

Any of these FVs must be considered to act on the point P2 on the surface S of MP2, via the strains $\varepsilon(\omega)$ and $\gamma(\omega)$, which create the stresses σ and τ (**Figure 2**, **Figure 3**). However, it must be stated that the principle of the superposition of effects is valid, meaning that we can separately analyse the effects of MP1 (or any MP_i) upon MP2.

We can consider the plane problem further, even though the stress phenomenon occurs in space (**Figure 4**).

In fact, on the entire outer surface S of MP2, there will be variations in stresses σ and τ, due to the differences in strains $\varepsilon(\omega)$ and $\gamma(\omega)$, which are precisely created on the surface S of MP2 by the action of the FVs of the ether produced by MP1.

We can consider the action of any FV waves on PM2, by exerting small percussions p_i with the FV frequency(pulsation) $\nu(\omega)$ (**Figure 4**). The percussions p_i are the results of the variations in the stresses σ and τ produced by any vibrating ECs, due to the FVs of the ether, consisting of the deformations $\varepsilon(\omega)$ and $\gamma(\omega)$ with frequency/pulsation ν/ω of the FVs.

However, we consider that the small percussions p_i of an EC, act with the frequency ν of the FVs (**Figure 4**). If the frequency of an FV is ν, the EC and the produced p_i will act ν times per second, and so the percussions p_i, which are discrete in time, will result in a continuous equivalent force f_i of an EC, given by the equation

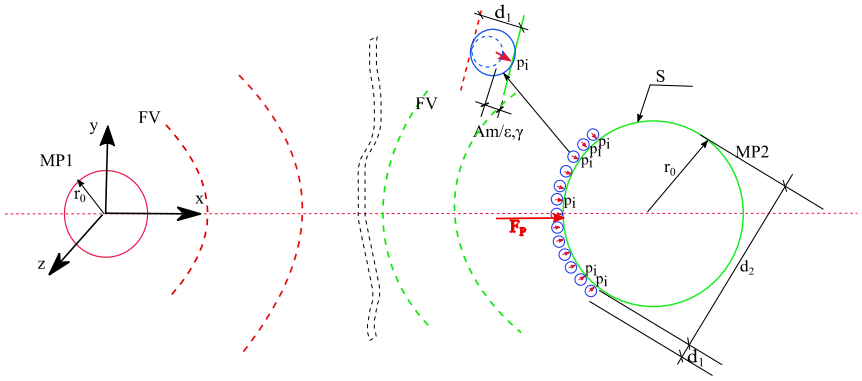

Figure 4. The mechanism of production of the percussions p_i created by FV from MP1 to MP2, in the *Oxyz* reference frame attached to the immovable MP1.

$$p_i = \frac{1}{\nu} f_i \tag{0}$$

Physically, the magnitude of the percussion force p_i will be given by the square of the amplitude $(A_m)^2$ of the displacement of the EC of the ether, at the time of the EC collision with MP2 (**Figure 4**). This is similar to the vibration energy of a harmonic oscillator. The magnitude of p_i will also depend on the distance l between MP1 and MP2, with a physically justifiable variation, along with the inverse of the square of the distance l^2, as in Coulomb's F_C force Equation (1) in [1].

$$p_i = k_e \frac{(A_m)^2}{l^2} \tag{1}$$

In Equation (1), k_e is an elastic coefficient of the type of Hooke's modulus E from the field of mechanics:

$$\sigma = E\varepsilon \quad or \quad E = \sigma/\varepsilon \tag{2}$$

showing the proportionality between p_i and the amplitude A_m. It follows that the measurement unit (in SI) of k_e will be

$$[k_e] = \frac{[p_i][l^2]}{[A_m]^2} = \frac{\mathrm{N}\cdot\mathrm{s}\cdot\mathrm{m}^2}{\mathrm{m}^2} = \mathrm{N}\cdot\mathrm{s} \tag{2a}$$

It follows that the measurement unit (in SI) of E from Equation (2) will be:

$$[E] = \frac{[\sigma]}{[\varepsilon]} = \frac{\mathrm{N/m}^2}{-} = \mathrm{N/m}^2 \tag{2b}$$

The unitary force f_i given by an EC, which is considered to be a continuous force in time resulting from the percussions p_i from an EC upon a MP, will be given by introducing (1) into (0), resulting in:

$$f_i = \nu p_i = \nu k_e \frac{(A_m)^2}{l^2} \tag{2c}$$

We will make an approximate assessment of the force f_i by adopting a possible

value for the elastic constant k_e from Equation (1). We do this by utilizing its similarity to the value of the elastic coefficient E in Hooke's law for a solid crystalline body (closest to the behaviour of the Type A ether in [1]).

For steel, we have the following value from mechanics.

$$E \approx 2\times 10^{11}\ \mathrm{N/m^2} \tag{2d}$$

Now, it follows that in Equation (2c) the expression with the same measurement unit (in SI) as E in (2b) will be

$$\left[\frac{\upsilon k_e}{l^2}\right]=\frac{[f_i]}{\left[(A_m)^2\right]}=\frac{\mathrm{N}}{\mathrm{m}^2}=[E'] \tag{3}$$

From Equations (2a) and (3) we find the equivalence of terms.

$$k_e=\frac{E'l^2}{\upsilon} \tag{3a}$$

We obtain a value of the ether modulus E' of about three orders of magnitude greater than that for steel from Equation (2d):

$$E'=10^3\times E=10^3\times 2\times 10^{11}\ \mathrm{N/m^2}\approx 2\times 10^{14}\ \mathrm{N/m^2} \tag{3b}$$

1). The case of astronomical distances. Now, we substitute in (3a) an astronomical distance $l = 10^7$ m, and a frequency for the FVs approximately the same as for γ rays, *i.e.* $\nu = 10^{22}$ Hz, obtaining:

$$k_e=\frac{2\times 10^{14}\left(10^7\right)^2}{10^{22}}=2\times 10^6\ \mathrm{N\cdot s} \tag{3c}$$

Here, we must consider the spatial problem of MP1 and MP2, with f_i representing the modulus of a spatial vector $\overline{f_i}$, oriented normally at the sphere surface of MP2 at any point.

The resultant force F_P given by the percussions produced by all the ECs in contact with MP2, with a total number of n percussions acting permanently in time on the sphere surface S of MP2 (**Figure 4**), will be the resultant sum of vectors $\overline{f_i}$ oriented normally on the entire surface S of MP2.

Let us calculate approximately the number n of ECs, for a diameter d_1, acting from the direction of MP1 on MP2 with diameter d_2 (**Figure 4**). We consider that the relevant area for the number n of ECs in contact with MP2, is that of the spheres of MP2 and that of the large circle of the EC. This can be calculated as the ratio of the spherical surface S of MP2 in contact with ECs and the area s of the large circle around the EC sphere.

$$n=\frac{S_{\mathrm{MP2}}}{s_{\mathrm{CE}}}=\frac{\pi d_2^2}{1/4\,\pi d_1^2}=4\frac{d_2^2}{d_1^2} \tag{4}$$

The ECs are located with distances between them of approximately $2d_1$. We consider that the diameter d_1 of an EC is $d_1 = b_e = 10^{-27}$ m, according to [1]. We consider that the diameter of an electron/proton MP is $d_2 = 10^{-15}$ m. Entering these values into (4) results in the following number (pcs) of ECs in contact.

$$n = 4\frac{\left(10^{-15}\right)^2}{\left(2\times10^{-27}\right)^2} = 4\frac{10^{-30}}{4\times10^{-54}} = 10^{24}\,\text{pcs} \tag{4a}$$

We will consider that the FV amplitude A_m is of the order of 10^{-3} d_1, similar to the working strain ε in the mechanics of solids.

The effects of percussions p_i (and of f_i) acting at 360˚ will be given by their projections on the Ox axis f_{ix}, which gives a mean projection angle of 45˚, resulting in

$$f_{ix} = f_i \cos 45^\circ = f_i \cdot 0.71 \tag{4b}$$

However, f_{ix} acts in two senses on the Ox axis, giving a distribution of approximately +50% and −50% in the two senses. The forces $+f_{ix}$ are given by the distance l_0 while the forces $-f_{ix}$ are given by the distance $(l_0 + d_1)$. We can obtain from Equations (4b) and (2c):

$$f_{i0} = \frac{0.71\nu g}{l^2} \quad \text{with} \quad g = k_e\left(A_m\right)^2 \tag{4c}$$

$$g = 2\times10^6\left(10^{-3}\times10^{-27}\right)^2 = 2\times10^{-54}\,\text{N}\cdot\text{s}\cdot\text{m}^2 \tag{4d}$$

Using an astronomical distance $l_0 = 10^7$ m we can obtain from Equations (4b), (4c) and (4d):

$$\frac{1}{0.71}f_{i0} = 2\times\frac{10^{22}\times10^{-54}}{\left(10^7\right)^2} = 2\times\frac{10^{-32}}{\left(10^7\right)^2}\,\text{N} \tag{4e}$$

$$\frac{1}{0.71}f_{i1} = 2\times\frac{10^{22}\times10^{-54}}{\left(10^7+10^{-15}\right)^2} = 2\times\frac{10^{-32}}{\left(10^7+10^{-15}\right)^2}\,\text{N} \tag{4f}$$

Hence the net force is given by the difference of the forces from Equations (4e) and (4f):

$$\Delta f_i = f_{i1} - f_{i0} = 0.71\times2\times10^{-32}\left[\frac{1}{\left(10^7+10^{-15}\right)^2} - \frac{1}{\left(10^7\right)^2}\right] \tag{5}$$

$$\begin{aligned}\Delta f_i = f_{i1} - f_{i0} &= 0.71\times2\times10^{-32}\frac{\left(10^7\right)^2 - \left(10^7+10^{-15}\right)^2}{\left(10^7\right)^2\left(10^7+10^{-15}\right)^2} \\ &= 0.71\times2\times10^{-32}\frac{10^{14} - 10^{14} - 2\times10^7\times10^{-15} - 10^{-30}}{10^{14}\left(10^{14} + 2\times10^7\times10^{-15} + 10^{-30}\right)}\end{aligned} \tag{5a}$$

$$\begin{aligned}\Delta f_i = f_{i1} - f_{i0} &\approx 0.71\times2\times10^{-32}\times\frac{-2\times10^7\times10^{-15}}{10^{14}\times10^{14}} \\ &= -0.71\times2\times10^{-32}\times\frac{2\times10^{-8}}{10^{28}} = -2.84\times10^{-68}\,\text{N}\end{aligned} \tag{5b}$$

The total force of interaction F_P upon an MP, given by the net percussions Δf_i of all the ECs around it, can be calculated from Equations (4a) and (5b).

$$F_P = n\times\Delta f_i = -10^{24}\times2.84\times10^{-68} = -2.84\times10^{-44}\,\text{N} \tag{6}$$

For comparison, we will calculate the classical Coulomb force F_C, using Equation (1) of [1]. In a situation in which MP2 has a charge $+e$ and MP1 has a charge $-e$, located at a distance of $l = 10^7$ m, this results in:

$$F_c = -\frac{(1e)^2}{4\pi \times 8.85\times 10^{-12}\times l^2} = -\frac{\left(1.6\times 10^{-19}\right)^2}{4\pi \times 8.85\times 10^{-12}\times \left(10^7\right)^2} = -2.30\times 10^{-42}\,\mathrm{N} \quad (6a)$$

It is noted that in Equations (6) and (6a), the two forces F_P and F_C were obtained with values that were not equal but close, with $F_P < F_C$.

This can also be seen by considering that the value of F_P obtained in (6) is the force resulting from only one electric interaction path l_i out of multiple interaction paths and multiple corresponding forces F_{Pi}, as will be seen in Section 5.

The difference is also due to the approximations of the physical parameters of ether and of the simplified forces f_i, made in the above numerical calculation.

2). The case of a laboratory distance. Now, we substitute in Equation (3a) a laboratory distance $l = 10^{-1}$ m and the same frequency for the FVs, and we obtain

$$k_e = \frac{2\times 10^{14}\left(10^{-1}\right)^2}{10^{22}} = 2\times 10^{-10}\,\mathrm{N\cdot s} \quad (7)$$

From Equations (4c) and (7) we obtain:

$$g = 2\times 10^{-10}\left(10^{-3}\times 10^{-27}\right)^2 = 2\times 10^{-70}\,\mathrm{N\cdot s\cdot m^2} \quad (7b)$$

With a laboratory distance $l_0 = 10^{-1}$ m we can obtain from Equations (4e), (4f) and (7b):

$$\frac{1}{0.71} f_{i0} = 2\times \frac{10^{22}\times 10^{-70}}{\left(10^{-1}\right)^2} = 2\times \frac{10^{-48}}{\left(10^{-1}\right)^2}\,\mathrm{N} \quad (8a)$$

$$\frac{1}{0.71} f_{i1} = 2\times \frac{10^{22}\times 10^{-70}}{\left(10^{-1}+10^{-15}\right)^2} = 2\times \frac{10^{-48}}{\left(10^{-1}+10^{-15}\right)^2}\,\mathrm{N} \quad (8b)$$

Hence, the net force Δf_i given by the difference of the forces f_i above, will be:

$$\Delta f_i = f_{i1} - f_{i0} = 0.71\times 2\times 10^{-48}\left[\frac{1}{\left(10^{-1}+10^{-15}\right)^2} - \frac{1}{\left(10^{-1}\right)^2}\right] \quad (9)$$

$$\begin{aligned}\Delta f_i = f_{i1} - f_{i0} &= 0.71\times 2\times 10^{-48}\frac{\left(10^{-1}\right)^2 - \left(10^{-1}+10^{-15}\right)^2}{\left(10^{-1}\right)^2\left(10^{-1}+10^{-15}\right)^2} \\ &= 0.71\times 2\times 10^{-48}\frac{\left(10^{-1}\right)^2 - \left(10^{-1}\right)^2 - 2\times 10^{-1}\times 10^{-15} - 10^{-30}}{10^{-2}\left(10^{-2}+2\times 10^{-1}\times 10^{-15}+10^{-30}\right)}\end{aligned} \quad (9b)$$

$$\begin{aligned}\Delta f_i = f_{i1} - f_{i0} &\approx 0.71\times 2\times 10^{-48}\times \frac{-2\times 10^{-1}\times 10^{-15}}{10^{-2}\times 10^{-2}} \\ &= -0.71\times 2\times 2\times 10^{-48}\times \frac{10^{-16}}{10^{-4}} = -2.84\times 10^{-60}\,\mathrm{N}\end{aligned} \quad (9c)$$

The total force of interaction F_P upon an MP, given by the net percussions Δf_i of all the ECs around it, can be calculated from Equations (4a) and (9c).

$$F_P = n \times \Delta f_i = -10^{24} \times 2.84 \times 10^{-60} = -2.84 \times 10^{-36}\ \text{N} \tag{10}$$

For comparison, we will calculate the classical Coulomb force F_C, using Equation (1) of [1]. In a situation in which MP2 has a charge $+e$ and MP1 has a charge $-e$, located at a laboratory distance of $l = 10^{-1}$ m, this results in

$$F_c = -\frac{(1e)^2}{4\pi \times 8.85 \times 10^{-12} \times l^2} = -\frac{\left(1.6 \times 10^{-19}\right)^2}{4\pi \times 8.85 \times 10^{-12} \times \left(10^{-1}\right)^2} = -2.30 \times 10^{-26}\ \text{N} \tag{10a}$$

It is noted that, in Equations (10) and (10a), the two F_P and F_C forces obtained were not equal, but were in the same large domain, with $F_P \ll F_C$, which is also due to the approximations of the physical parameters of ether and the simplified forces f_i, used in the above numerical calculation and which is more suitable for astronomical distances.

Comparing this result with the result from i), we conclude that the method utilized above and also in [3], is more suitable for the astronomical domain, while for the laboratory and atomic domains, it must be improved.

This can also be seen by considering that the value of F_P obtained in (10) is the force resulting only from only one electric interaction path l_i from among many interaction paths and multiple corresponding forces F_{Pi}, as shown in Section 5.

5. Presentation of the Mechanism of the Physical Interaction between Microparticles with Electric Charges

We will now analyse the physical mechanism for producing an electrical interaction between the MPs, which we consider as being the only carriers of the positive and negative electric charges. This hypothesis implies the existence of only charged MP^+ and MP^- microparticles, but in this paper the signs + and − will not be indicated but only supposed. Even particles which are considered neutral, such as neutrons, are composed of MP^+ and MP^- pairs, giving zero total charge.

As a result of the electrical interactions between MPs in the ether, there will be a force that will act on each electrically charged MP. Classically, this force is considered today to be Coulomb's F_C electric force.

However, this force was recently identified and named by the present authors [3] the Coulomb completed force or F_{CC}.

The F_{CC} will be created as an effect of ε and γ ether deformations developed on the surface of the MP2, produced by the FVs originating from MP1. We can assume that the FVs are transmitted through ether, by rays, roads or paths, starting from MP1 and inclined at different angles α_i (**Figure 4**). Next, we will denote by l_i the lengths of the complete paths between MP1 and MP2, starting at radius r_i.

The effect of ε and γ ether deformations is also seen by changes in the stresses σ and τ acting on the surface of MP2 (**Figure 2**, **Figure 3**), which create F_{CC} ac-

cording to the mechanism presented in Section 2.

The FVs travel at a speed c_f, with the first FVs reaching MP2 being those that travel the shortest direct path l_0, arriving after time t_0 (Figure 4, Figure 5).

$$t_0 = l_0 / c_f \tag{11}$$

The first FVs will leave MP1 at time t_i. For simplicity, we adopt $t_i = 0$, without thereby affecting the generality of the analysis. These FVs create ε and γ (both with pulsation ω) deformations of the ether cell network, on the surface of MP2 (Figure 2, Figure 4, Figure 5).

Similarly, the FVs travelling along path $l_1 > l_0$ reach MP2 after time t_1.

$$t_1 = l_1 / c_f \tag{11a}$$

Meanwhile, the FVs that travel along path $l_2 > l_1$ arrive after time t_2

$$t_2 = l_2 / c_f \tag{11b}$$

while the FVs that travel along path $l_n > l_{n-1}$ arrive after the time t_n.

$$t_n = l_n / c_f \tag{11c}$$

However, at the same time t_0, all the FVs travelling in the directions of rays $r_1, r_2, r_3, \cdots, r_n$ and moving along paths $l_1, l_2, l_3, \cdots, l_n$, will be able to reach MP2 (Figure 5, Figure 6). However, they left MP1 in the moments preceding t_0 and their paths must observe the condition of the total accumulated intervals Δl_{ti}, given that we also have:

$\Delta t = \Delta l / c_f$, and hence (11d)

$$\Delta l_{ti} = l_i - l_0 = t_i c_f \tag{11e}$$

However, each of these FV_i vibrations creates a percussion force F_P on MP2, according to Equation (6) in Section 3.

All these F_P forces, when summed up over all FV_i vibrations on the entire surface S of MP2, create the Coulomb completed force F_{CO}, according to our hypothesis in Equation (21) from [3].

We can depict the elementary force of the F_P percussion type in a simple and natural general form similar to Equation (6), as a variation proportional to the inverse of the square root of the ray r travelled by the FVs in ether free of any other EPs.

$$F_P = \frac{k_p}{r^2} \tag{12}$$

At time t_0, all the F_{Pi} forces created by FVs on MP2, leaving MP1 at times t_i from Equation (11c), preceding t_0 and corresponding to the lengths l_i of the travelled paths, simultaneously act directly on MP2. The different forces F_{Pi} given by (12) oriented according to the rays r_i inclined at angles α_i, are as follows (Figure 5, Figure 6).

$$F_{P0} = \frac{k_p}{l_0^2}; F_{P1} = \frac{k_p}{l_1^2}; F_{P2} = \frac{k_p}{l_2^2}; \cdots; F_{Pi} = \frac{k_p}{l_i^2}; \cdots; F_{Pn} = \frac{k_p}{l_n^2} \tag{13}$$

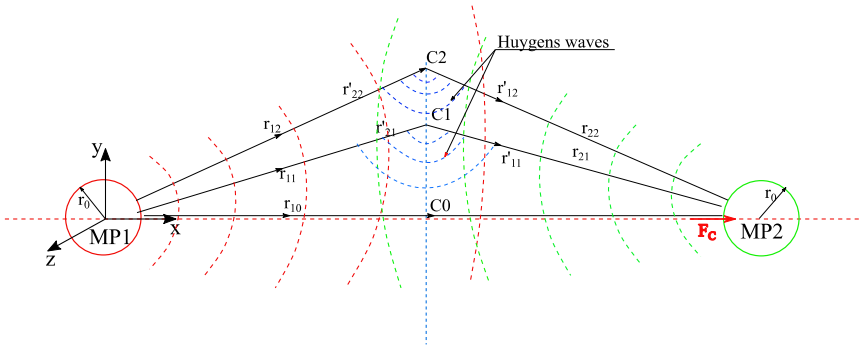

Figure 5. Transmission of FVs in the form of rays r_i created by MP1 and MP2, which at points C continue as secondary waves of the Huygens type, in the $Oxyz$ reference frame attached to the immovable MP1.

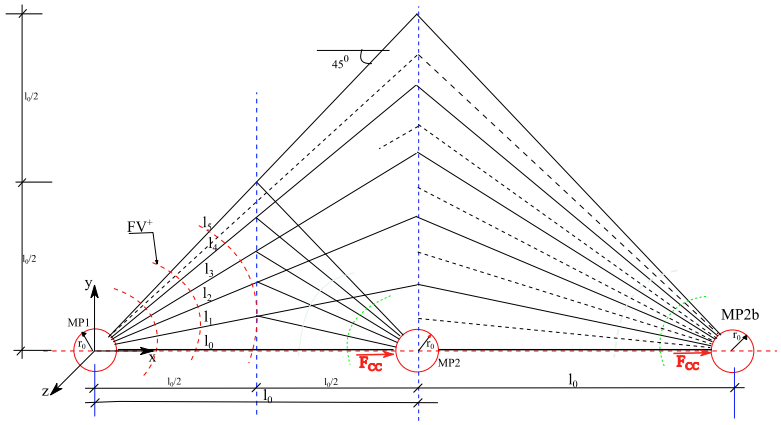

Figure 6. Simple representation of the triangular pathways l_i of the F_{CC} electrical interaction force between MP1, MP2 and MP2b, including $2l_0$ with 11 paths, in the $Oxyz$ reference frame attached to the immovable MP1.

The total force F_P^{tot} is obtained by summing all the F_{Pi} forces from Equations (13), as they are simultaneous actions with simultaneous percussions p_i in time. However, the sum must be vectorial.

This real F_P^{tot} total force will only be obtained correctly if each force F_{Pi} in the series of forces in (13) is of the F_{Pi} type, *i.e.*, is the result of a single full vibration FV_i, which will produce a single set of percussions p_i. This result can only be obtained if, when starting from MP1, the FV_i waves are separated in time by a time period T_i. This fact will correspond, on arrival at MP2, with the distance between two successive wavelengths of FV_i.

$$\Delta l_i = \lambda = ct \tag{14}$$

On MP2b, the F_{2i} forces have the same formulas as in Equation (13), but with new distances l_i adapted according to **Figure 6**.

Below, we analyse the situation created at the surface of an MP2, where the specific deformations ε and $\gamma(\omega)$ occur in the EC network of the ether. These deformations are due to the FVs created by a series of microparticles MP1a, MP1b, MP1c, … (**Figure 7**).

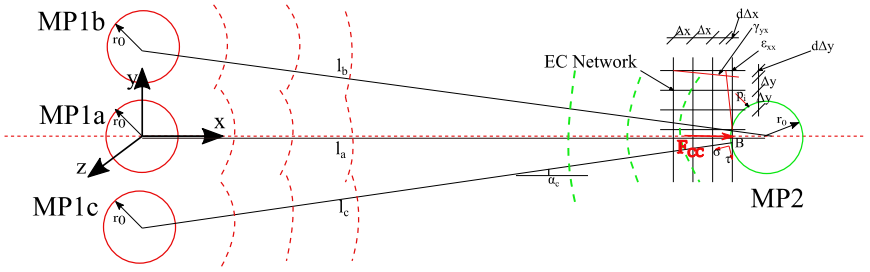

Figure 7. The mode of occurrence of the stresses σ and τ on MP2, due to strains ε and $\gamma(\omega)$ created by MP1a, in the *Oxyz* reference frame attached to the immovable MP1.

Obviously, according to **Figure 7**, the deformations ε and $\gamma(\omega)$ in the ether, at a point P_i on the surface of MP2, located at distances l_a, l_b, l_c from MP1a, MP1b and MP1c, decrease inversely relative to the square of these distances, when taking into account the formula for F_C obtained in Equation (1) from [1] and the formula of the F_P force obtained in Equation (13). This behaviour of FVs in the ether, considered as a special mechanical matter, is also justified by its similarity to a common physical phenomenon depending on $1/r^2$ in normal matter (solid, liquid or gas).

Therefore, the unitary forces σ and τ, exerted upon MP2 by the ECs due to the strains ε and $\gamma(\omega)$ created by MP1a, MP1b, …, will have to be inversely proportional to the square of these distances $l_a^2,\cdots,l_c^2,\cdots$ based on the result from Section 4.

In **Figure 7**, only the effect of the direct rays r_a, having the slope $\alpha_0 = 0^\circ$ with path length l_a, is represented as a grid of ECs near MP2 and as percussions p_i.

However, it is necessary to analyse the effects upon MP2 produced by other possible indirect paths starting from MP1, on various radii r_{1i} drawn in any direction with inclination angles α_i (**Figures 5-7**).

As the rays starting from MP1 are inclined at angle α_i, they are able to reach MP2 on an indirect path in the form of an isosceles triangle (**Figure 6**). This isosceles path will be the shortest path starting from MP1 at any angle α_i.

Such a path can be accomplished physically by applying the Huygens principle to the midpoint C_i of the radius r_{1i} (**Figure 5**). Here, the circles (in the plane problem, but real spheres in the spatial problem) of the Huygens secondary waves with a centre at C_i will allow the construction of the symmetrical radius r'_{1i} of the radius r_{1i}.

In fact, at the point C_i (**Figure 5**), the waves which will travel along the ray r_{1i}, will arrive at the same time as those arriving from the r_{2i} radius that started from MP2 simultaneously with r_{1i}. As a result, the interaction between MP1 and MP2 must be symmetrical in space and in time (**Figure 5**, **Figure 6**).

Therefore, it can also be considered that, at point C_i (**Figure 5**), a special interference of FVs appears, with no terminus point between the waves in the rays r_{1i} and r_{2i}. At this point, these rays mutually interchange their path, moving in the forward direction beyond point C_i. This phenomenon is symmetrical due to the symmetry of MP1 and MP2, including the ether homogeneity and hence the

symmetry of HM16.

The rays $r_i + r_i'$, which are inclined at the angle α_i, will travel the corresponding distances l_i (Figure 5, Figure 6) to MP2 in a longer time t_i.

However, at a certain moment (t_0), various waves with rays r_i, which left MP1 at various moments preceding t_0 (the shortest time), will arrive at MP2 with forces F_{Pi} according to Equation (13), giving a total force F_P^{tot}.

A question arises as to whether the overlapping of rays with various angles $\alpha_i > 0$ from the other MPs existing in the range close to MP2 (Figure 6), influence the final result of the interaction force F_P between MP1 and MP2. The situation occurs in compact MBs (solids, liquids) when the distance d_0 between neighbouring MPs is less than 1_0 at a certain density.

However, as we discuss and analyse for two different physical situations for MP2, isolated or not isolated, the result for the F_P force must be different. Consequently, it is necessary to introduce a correction reducing F_P based on the MP density. Such a correction is possible using various mathematical procedures, including correcting the power of 2 in the distance l^2.

However, in our current stage of analysis, we evaluate the interaction between any MP1 and MP2 as isolated, considering the normal contribution of all the rays with angles $\alpha \leq 45^\circ$ (a cone, in space).

6. Presentation of the Calculation for the F_P Electric Interaction Force between Microparticles, Considering Multiple Paths in the Ether, including Justification of the Term ln*r* in F_{CC} Force

6.1. The General Case of the Electric Interaction Problem

A calculus demonstrating the capping trend of decreasing of the F_P force with distance l (according to the term ln$r$), is presented in the following analysis. Here, we analyse the variation of electric force F_P with distance, starting from the percussions of the ether (Sections 4 and 5). The next calculation of F_P is based on multiple paths l_i of FVs between two MPs.

We consider the situation of two MPs, MP1 and MP2, each with an elementary electric charge $\pm q$, located at a direct distance l_0 (Figure 8).

The electrical interaction between the two MPs occurs via all FVs, which can occur outside the direct path l_0 and travel on other deviating paths, with the general form of concave curves (Figure 8).

As a simplified particular case, we adopt here simple paths in the form of isosceles triangles, as discussed in Section 5.

In the general case, we accept that we have discretized the area of influence between MP1 and MP2 in a number $n + 1$ of curvilinear paths l_i (Figure 8).

These paths are arranged on one half of the interaction surface, which is bounded at the bottom by the Ox axis and at the top by the line inclined at 45˚, in the case of the plane problem. Figure 8 presents the case with 6 paths (red), l_0, l_1, l_2, l_3 l_4, and l_5, which applies to the plane problem of the interaction between MP1 and MP2.

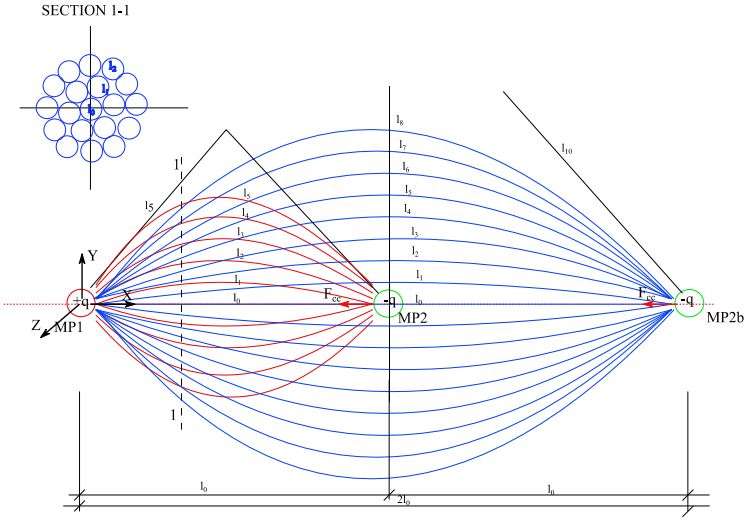

Figure 8. Representation in the HM16A ether of the concave-shaped paths, approximated by isosceles triangles, for the electrical interaction force F_P, which creates the F_{CC} force between MP1 and MP2, in the *Oxyz* reference frame attached to the immovable MP1.

Further, in the general case with n + 1 paths $l_0, l_1, l_2, l_3, \cdots, l_n$, for the total force from the percussions F_P^{tot}, noting the differences in the paths $\Delta l_i = l_i - l_{i-1}$, we have from Equation (13):

$$F_P^{tot} = \frac{k_p}{l_0^2}\left[1 + \frac{1}{\left(1+\frac{\Delta l_1}{l_0}\right)^2} + \frac{1}{\left(1+\frac{\Delta l_1 + \Delta l_2}{l_0}\right)^2} + \cdots + \frac{1}{\left(1+\frac{\Delta l_1 + \Delta l_2 + \cdots + \Delta l_n}{l_0}\right)^2}\right] \quad (15)$$

For simplicity, we consider the length differences of paths Δl to be constant and identical between any two paths l_i and l_{i-1}. This does not significantly affect the final result. These paths differences Δl must be at least equal to the wavelength λ, according to Section 5, but may be multiples of it, as in the general case.

In turn, the lengths of successive paths l_i can be written as:

$$l_i = l_0 + i\Delta l \quad \text{with} \quad i \in (0, n) \quad (16)$$

In this case, we can also write:

$$\Delta l = l_i - l_{i-1} = \frac{l_n - l_0}{n} \quad (16a)$$

We will define the relative length difference ε as follows:

$$\varepsilon = \frac{\Delta l}{l_0} \quad (16b)$$

We will directly calculate the magnitude of the total corrected force F_P^{tot}, adding, term by term, the F_{Pi} forces, which arise from the various FV waves that have passed along the paths l_i (**Figure 6**, **Figure 8**), according to Equations (7)

and (13), resulting in:

$$F_P^{tot}=\frac{k_p}{l_0^2}\left[1+\frac{1}{\left(1+\frac{\Delta l}{l_0}\right)^2}+\frac{1}{\left(1+\frac{2\Delta l}{l_0}\right)^2}+\cdots+\frac{1}{\left(1+\frac{i\Delta l}{l_0}\right)^2}+\cdots+\frac{1}{\left(1+\frac{(n)\Delta l}{l_0}\right)^2}\right]$$

$$F_P^{tot}=\frac{k_p}{l_0^2}\left[1+\frac{1}{(1+\varepsilon)^2}+\frac{1}{(1+2\varepsilon)^2}+\cdots+\frac{1}{(1+i\varepsilon)^2}+\cdots+\frac{1}{(1+(n)\varepsilon)^2}\right] \quad (17)$$

It is noted that, in Equation (17), after the first term, there appears a series with n terms with the variable ratio q, where

$$q=\left(\frac{1+(k-1)\varepsilon}{1+k\varepsilon}\right)^2 \text{ and the first term is } a_1=\frac{1}{(1+\varepsilon)^2};\ k\in(2,3,\cdots,n) \quad (18)$$

The sum of this series is too laborious to compute analytically.

Consequently, we will apply the numerical calculation method to the series sum, whose results can then be generalized as follows.

6.2. Case of the Plane Problem for Numerical Calculations

6.2.1. Situation with the Maximum Angle $\alpha = 45^\circ$

a.1) Situation Involving the Initial Distance l_0, Considering the Upper Half of the Plan Domain, Comprising 6 Paths

In this section, we use an approximate numerical empirical calculation by considering some numerical cases with a small number of paths (n + 1). The result obtained via this procedure can be then generalized and will be useful at the current stage of the HM16 model.

In the first situation a.1) (in the parentheses in (17)), we consider the initial case (**Figure 8**) in which n = 5 and there are 6 paths which are distributed initially on only half of the domain above the Ox axis, in the plane problem. For simplicity, we replace the curved paths in **Figure 8** with isosceles triangular paths, according to Section 5, as shown in **Figure 6** and **Figure 9**. In this case, for the angle $\alpha_{\max} = 45^\circ$ from Equation (16a), we obtain:

$$\delta l = l_5 - l_0 = 1.41 l_0 - l_0 = 0.41 l_0 \quad (19)$$

$$\Delta l = \frac{\delta l}{n} \quad (20)$$

$$\varepsilon = \frac{\Delta l}{l_0} = \frac{0.41 l_0}{l_0 \cdot n} = \frac{0.41}{5} = 0.082 \quad (21)$$

By introducing (21) into Equation (17), we have:

$$F_P^{tot}=\frac{k_p}{l_0^2}\left[1+\frac{1}{(1+0.082)^2}+\frac{1}{(1+2\times0.082)^2}+\frac{1}{(1+3\times0.082)^2}+\frac{1}{(1+4\times0.082)^2}+\frac{1}{(1+5\times0.082)^2}\right] \quad (22)$$

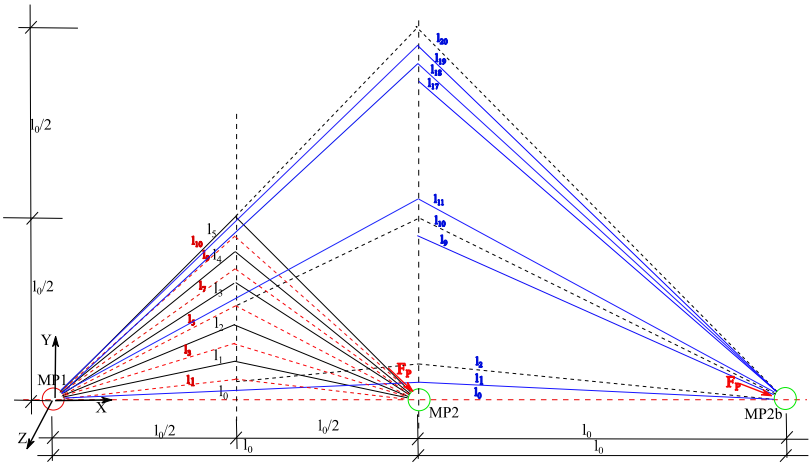

Figure 9. Representation of the triangular paths l_i of the electrical interaction force F_P, which creates the F_{CC} force between MP1 and MP2, including the case $2l_0$ with 21 paths, in the *Oxyz* reference frame attached to the immovable MP1.

$$\begin{aligned} F_P^{tot} &= \frac{k_p}{l_0^2}\left[1+0.854+0.783+0.644+0.567+0.503\right] \\ &= \frac{k_e}{l_0^2}\left[1+3.35\right] = \frac{k_e}{l_0^2}\times 4.35 \end{aligned} \tag{22a}$$

a.1).s. A supplemental calculus (not reproduced here) also for this distance but with 9 paths gave the result:

$$F_P^{tot} = \frac{k_e}{l_0^2}\left(1+5.432\right) = \frac{k_e}{l_0^2}\times 6.432 \tag{22b}$$

a.2) Situation Involving the Initial Distance l_0, on Half of the Plan Domain, with 11 Paths

Now, we double the number of paths by thickening the 6 paths considered in a.1), according to Figure 9, including the dashed paths, resulting in 11 paths for which $n = 10$. For simplicity, we have also replaced the curved paths with isosceles triangles, according to Section 5. In this case, for the angle $\alpha_{\max} = 45^\circ$ from (16b), we obtain:

$$\delta l = l_{10} - l_0 = 1.41 l_0 - l_0 = 0.41 l_0 \tag{23}$$

$$\varepsilon = \frac{\Delta l}{l_0} = \frac{0.41 l_0}{l_0 \cdot 10} = \frac{0.41}{10} = 0.041 \tag{23a}$$

By introducing (23a) into Equation (17), we obtain:

$$\begin{aligned} F_P^{tot} = \frac{k_p}{l_0^2}\Bigg[& 1+\frac{1}{\left(1+0.041\right)^2}+\frac{1}{\left(1+2\times 0.041\right)^2}+\frac{1}{\left(1+3\times 0.041\right)^2} \\ & +\frac{1}{\left(1+4\times 0.041\right)^2}+\frac{1}{\left(1+5\times 0.041\right)^2}+\frac{1}{\left(1+6\times 0.041\right)^2} \\ & +\frac{1}{\left(1+7\times 0.041\right)^2}+\frac{1}{\left(1+8\times 0.041\right)^2}+\frac{1}{\left(1+9\times 0.041\right)^2}+\frac{1}{\left(1+10\times 0.041\right)^2}\Bigg] \end{aligned} \tag{24}$$

$$\begin{aligned} F_P^{tot} &= \frac{k_p}{l_0^2}\left[1+0.9227+0.8541+0.793+0.738+0.6886\right. \\ &\quad \left.+0.644+0.6037+0.567+0.5335+0.503\right] \\ &= \frac{k_p}{l_0^2}\left[1+6.847\right] \\ &= \frac{k_p}{l_0^2}\times 7.847 \end{aligned} \tag{25}$$

b.1) Situation with the Initial Distance Doubled ($2l_0$) on Half of the Plan Domain, with 6 Paths

In the second case in Figure 9, between MP1 and MP2 we have a distance $2l_0$ and $n = 5$ with 6 paths, so we replace l_0 with $2l_0$ in Equations (16), (17) and (21), resulting in:

$$l_5 - l_0 = 1.41\times 2l_0 - 2l_0 = 0.41\times 2l_0 = 0.82l_0 \tag{26}$$

$$\Delta l = \frac{0.82l_0}{5} = 0.164l_0 \tag{26a}$$

$$\varepsilon = \frac{\Delta l}{2l_0} = \frac{0.164l_0}{2l_0} = 0.082 \tag{26b}$$

By introducing (26b) into Equation (17), we obtain:

$$F_P^{tot} = \frac{k_p}{(2l_0)^2}\left[1+\frac{1}{(1.082)^2}+\frac{1}{(1.164)^2}+\frac{1}{(1.246)^2}+\frac{1}{(1.328)^2}+\frac{1}{(1.41)^2}\right] \tag{27}$$

$$F_P^{tot} = \frac{k_p}{(2l_0)^2}\left[1+0.854+0.738+0.644+0.567+0.503\right]$$

$$\begin{aligned} F_P^{tot} &= \frac{k_p}{(2l_0)^2}\left[1+3.306\right] = \frac{k_p}{(2l_0)^2}\times 4.306 \\ &= \frac{k_p}{(2l_0)^2}\frac{1}{4}\times 4.306 = \frac{k_p}{l_0^2}\times 1.0765 \end{aligned} \tag{27a}$$

b.2) Situation with the Initial Distance Doubled ($2l_0$) on Half of the Plan Domain, with 11 Paths

Now, we double the number of paths by thickening the 6 paths considered in b.1) according to Figure 9, including the dashed paths, resulting in 11 paths for which $n = 10$. For simplicity, we also replace the curved paths from Figure 7 with isosceles triangles from Figure 9, according to Section 5. In this case, for the angle $\alpha_{\max} = 45^\circ$, we obtain from (26a):

$$l_{10} - l_0 = 1.41\times 2l_0 - 2l_0 = 0.41\times 2l_0 = 0.82l_0 \tag{28}$$

$$\Delta l = \frac{0.82l_0}{10} = 0.082l_0 \tag{28a}$$

$$\varepsilon = \frac{\Delta l}{2l_0} = \frac{0.082l_0}{2l_0} = 0.041 \tag{28b}$$

Introducing (28b) into Equation (17), we have:

$$F_P^{tot}=\frac{k_p}{(2l_0)^2}\left[1+\frac{1}{(1+0.041)^2}+\frac{1}{(1+2\times0.041)^2}+\frac{1}{(1+3\times0.041)^2}+\frac{1}{(1+4\times0.041)^2}+\frac{1}{(1+5\times0.041)^2}+\frac{1}{(1+6\times0.041)^2}+\frac{1}{(1+7\times0.041)^2}+\frac{1}{(1+8\times0.041)^2}+\frac{1}{(1+9\times0.041)^2}+\frac{1}{(1+10\times0.041)^2}\right] \tag{29}$$

$$F_P^{tot}=\frac{k_p}{(2l_0)^2}[1+0.9227+0.8541+0.793+0.738+0.6886+0.644+0.6037+0.567+0.5335+0.503] \tag{29a}$$

$$=\frac{k_p}{(2l_0)^2}[1+6.847]=\frac{k_p}{(2l_0)^2}\times7.847=\frac{k_p}{(l_0)^2}\frac{1}{4}\times7.847=\frac{k_p}{(l_0)^2}\times1.962$$

b.2).s. A supplemental calculus (not reproduced here) also for this distance but with 17 paths gave the result:

$$F_P^{tot}=\frac{k_e}{l_0^2}(1+2.045)=\frac{k_e}{l_0^2}\times3.045 \tag{29b}$$

b.3) Situation with the Initial Distance Doubled ($2l_0$) on Half of the Plan Domain, with 21 Paths

Now, we double the number of paths by thickening the 6 paths considered in b.2) according to Figure 9, including the dashed paths, resulting in 21 paths for which n = 20. For the sake of simplicity, we also replace the curved paths with isosceles triangles, according to Section 5. In this case, for the angle $\alpha_{\max}$ = 45˚, from (28a) we obtain:

$$l_{20}-l_0=1.41\times2l_0-2l_0=0.41\times2l_0=0.82l_0 \tag{30}$$

$$\Delta l=\frac{0.82l_0}{20}=0.041l_0 \tag{30a}$$

$$\varepsilon=\frac{\Delta l}{2l_0}=\frac{0.041l_0}{2l_0}=0.0205 \tag{30b}$$

By introducing (30b) into Equation (17), we have:

$$F_P^{tot}=\frac{k_p}{(2l_0)^2}\left[1+\frac{1}{(1+0.0205)^2}+\frac{1}{(1+2\times0.0205)^2}+\frac{1}{(1+3\times0.0205)^2}+\frac{1}{(1+4\times0.0205)^2}+\frac{1}{(1+5\times0.0205)^2}+\cdots+\frac{1}{(1+16\times0.0205)^2}+\frac{1}{(1+17\times0.0205)^2}+\frac{1}{(1+18\times0.0205)^2}+\frac{1}{(1+19\times0.0205)^2}+\frac{1}{(1+20\times0.0205)^2}\right] \tag{31}$$

$$F_P^{tot} = \frac{k_p}{(2l_0)^2}[1+0.960+0.9227+0.887+0.8541+0.8227+0.793 + 0.7647+0.738+0.7126+0.6886+0.6658+0.644+0.6234 + 0.6037+0.5849+0.567+0.5499+0.5335+0.5179+0.503] \quad (31a)$$

$$= \frac{k_p}{(2l_0)^2}[1+13.271] = \frac{k_p}{(2l_0)^2}\times 14.271$$

$$= \frac{k_p}{(l_0)^2}\frac{1}{4}\times 14.271 = \frac{k_p}{(l_0)^2}\times 3.318$$

c.1) Situation with the Initial Distance l_0 and the Path Number Symmetrically Doubled across the Whole Plan Area

Let us now consider the complete plane situation shown in **Figure 9**, including the symmetrical paths relative to the horizontal centre axis *Ox*. This is a plane problem, doubling the terms in cases a) and b) above, which results in the following cases.

Case a.1):

$$F_P^{tot} = \frac{k_p}{l_0^2}[1+3.35+3.35] = \frac{k_p}{l_0^2}[1+6.70] = \frac{k_p}{l_0^2}\times 7.70 \quad (32)$$

Case a.2):

$$F_P^{tot} = \frac{k_p}{l_0^2}[1+6.847+6.847] = \frac{k_p}{l_0^2}[1+13.694] = \frac{k_p}{l_0^2}\times 14.694 \quad (33)$$

Case b.1):

$$F_P^{tot} = \frac{k_p}{4l_0^2}[1+3.306+3.306] = \frac{k_p}{4l_0^2}[1+6.612] = \frac{k_p}{l_0^2}\times 1.9034 \quad (34)$$

Case b.2):

$$F_P^{tot} = \frac{k_p}{4l_0^2}[1+6.847+6.847] = \frac{k_p}{4l_0^2}[1+13.694] = \frac{k_p}{l_0^2}\times 3.673 \quad (35)$$

Case b.3):

$$F_P^{tot} = \frac{k_p}{4l_0^2}[1+13.271+13.271] = \frac{k_p}{4l_0^2}[1+26.542] = \frac{k_p}{l_0^2}\times 6.885 \quad (36)$$

Now, in the relations (32), (33), (34), (35) and (36), it can be observed that the coefficients multiplying the same fraction k_p/l_0^2 are almost doubled, though not exactly but with a slightly diminished value, compared to similar cases in the relations (22a), (25), (27a), (29a) and (31a), as set out in Section 6.2.1 above. Accordingly, the favourable effect of the duplication of paths is acknowledged in this subsection.

6.2.2. Situation with the Angle $\alpha = 60^\circ$

d.1) Case of the Plane Domain Half Restricted: Path l_0, from Case a.1)

We now consider the case in which $\alpha = 60^\circ$. We add four additional paths giving 6 + 4 = 10 paths from 6.2.1. The number of intervals will be $n = 10 - 1 =$

9.

$$\delta l = l_{10} - l_0 = 2l_0 - l_0 = l_0 \tag{37}$$

$$\Delta l = \delta l / n = l_0 / 9 = 0.111 l_0;\ \ \varepsilon = \Delta l / l_0 = 0.111 \tag{37a}$$

We introduce (37a) into Equation (17), resulting in:

$$F_P^{tot} = \frac{k_p}{l_0^2}\left[1 + \frac{1}{(1+0.111)^2} + \frac{1}{(1+2\times 0.111)^2} + \frac{1}{(1+3\times 0.111)^2} + \frac{1}{(1+4\times 0.111)^2} + \frac{1}{(1+5\times 0.111)^2} + \cdots + \frac{1}{(1+9\times 0.111)^2}\right] \tag{38}$$

$$\begin{aligned} F_P^{tot} &= \frac{k_p}{l_0^2}[1 + 0.810 + 0.6696 + 0.5628 + 0.4795 + 0.4135 \\ &\quad + 0.3603 + 0.3166 + 0.2805 + 0.246] \\ &= \frac{k_e}{l_0^2}[1 + 4.1388] = \frac{k_e}{l_0^2}\times 5.1388 \end{aligned} \tag{38a}$$

The increase in the coefficient will be 5.1388/4.35 = 1.18 = 118%. Accordingly, the favourable effect of increasing the angle α to 60˚ is confirmed.

d.2) Case of the Half Restricted Domain: Path $2l_0$, from Case b.2)

We now consider the case in which α = 60˚. We add nine additional paths giving 10 + 9 = 19 paths from 6.2.1. The interval number is n = 19 − 1 = 18.

$$\Delta l = l_{19} - l_0 = 4l_0 - 2l_0 = 2l_0 \tag{39}$$

$$\Delta l = \delta l / n = 2l_0 / 18 = 0.111 l_0;\ \ \varepsilon = \Delta l / 2l_0 = 0.111 l_0 / 2l_0 = 0.0555 \tag{39a}$$

We introduce (39a) into Equation (17) resulting in:

$$F_P^{tot} = \frac{k_p}{(2l_0)^2}\left[1 + \frac{1}{(1+0.0555)^2} + \frac{1}{(1+2\times 0.0555)^2} + \frac{1}{(1+3\times 0.0555)^2} + \frac{1}{(1+4\times 0.0555)^2} + \frac{1}{(1+5\times 0.0555)^2} + \cdots + \frac{1}{(1+19\times 0.111)^2}\right] \tag{40}$$

$$\begin{aligned} F_P^{tot} &= \frac{k_p}{(2l_0)^2}[1 + 0.8976 + 0.810 + 0.7349 + 0.6696 + 0.6127 + 0.5628 \\ &\quad + 0.5186 + 0.4795 + 0.4447 + 0.4135 + 0.3855 + 0.3603 + 0.3374 \\ &\quad + 0.3166 + 0.2978 + 0.2805 + 0.2647 + 0.246 + 0.2369] \\ &= \frac{k_p}{(2l_0)^2}[1 + 8.8696] = \frac{k_p}{(2l_0)^2}\times 9.8696 \\ &= \frac{k_p}{l_0^2}\frac{1}{4}\times 9.8696 = \frac{k_p}{l_0^2}\times 2.4674 \end{aligned} \tag{40a}$$

The increase in the coefficient will be 2.4674/1.962 = 1.25 = 125%. Consequently, the favourable effect of increasing the angle α from 45˚ to 60˚ is confirmed above (+25%). But the paths extension beyond 45˚ is not justified physically because it do not match with ether symmetry and homogeneity, and will be abandoned.

6.3. Case of the Spatial Problem

a) General Situation

In order to be able to generalize to the spatial problem from any of the plane problems in Section 6.2, the number of paths which it is possible to consider in the spatial case will be determined.

For this, we note that the central path l_0 considers the ether as a cylinder of maximum radius r_0 in the middle part of the path (Figure 8, left). Further, the second row of cylindrical paths, each having a maximum radius r_0, is arranged in a circular manner with the cylinders centred on the paths in the form of a circle with radius $r_1 = 2r_0$. The length of this circle is

$$L_1 = 2\pi r_1 = 2\pi(2r_0) = 4\pi r_0 \tag{41}$$

The circles in row 2, which are evenly distributed, will have centres located on the L_1 circle to which a length reduction of approximately 5% is applied, to take account of the curvature of the route. Under these conditions, the reduced cylinder diameter will be $d_r = 0.95 \times 2r_0 = 1.9r_0$. Meanwhile, the number of adjacent circles (and cylinders) N_1 will be (Figure 8, left):

$$N_1 = \frac{L_1}{d_r} = \frac{4\pi r_0}{1.9r_0} = \frac{4\pi}{1.9} = 6.61 \text{ pcs} \tag{42}$$

Now, the paths in the third row with radius r_0 are placed with the centres of the cylinders on the circle with radius $r_2 = 4r_0$. The length of this circle is (Figure 8, left):

$$L_2 = 2\pi r_2 = 2\pi(4r_0) = 8\pi r_0 \tag{43}$$

The number of uniformly distributed circles will be:

$$N_2 = \frac{L_2}{d_r} = \frac{8\pi r_0}{1.9r_0} = \frac{8\pi}{1.9} = 13.2 \text{ pcs} \tag{44}$$

Similarly, the paths in the fourth row with radius r_0 can be distributed with the centres of the cylinders on the circle having a radius $r_3 = 6r_0$. The length of this circle is:

$$L_3 = 2\pi r_3 = 2\pi(6r_0) = 12\pi r_0 \tag{45}$$

The number of adjacent circles, evenly distributed, will be:

$$N_3 = \frac{L_3}{d_r} = \frac{12\pi r_0}{1.9r_0} = \frac{12\pi}{1.9} = 19.8 \text{ pcs} \tag{46}$$

From Equations (42), (44) and (46), we can observe the rule for forming the rows of cylinders, the number of which is an arithmetic progression, with a ratio of approximately 6 pcs (covered for 7 pcs) and having the first term equal to 1.

b) Particular Situations

e.1) Situation Involving the Initial Distance l_0 in Space, with 6 Initial Paths (from Case a.1)

We now recalculate the magnitude of the force of interaction F_P between MP1 and MP2, considering all spatial paths for the initial distance l_0, starting from the

six paths in Section 6.2. The number of these paths (pieces) will be in accordance with the rule above:

$$N^{tot} = 1+6+13+19+25+31 = 95 \text{ pcs} \tag{47}$$

The magnitude of the F_P interaction force is obtained from (22a) using (47):

$$\begin{aligned} F_P^{tot} &= \frac{k_p}{l_0^2}\left[1\times 1+0.854\times 6+0.783\times 13+0.644\times 19+0.567\times 25+0.503\times 31\right] \\ &= \frac{k_p}{l_0^2}\left[1+5.12+10.18+12.23+14.17+15.59\right] = \frac{k_e}{l_0^2}\times 58.29 \end{aligned} \tag{48}$$

e.2) Situation Involving the Initial Distance l_0 in Space, with 11 Initial Paths (from Case a.2)

We now recalculate the magnitude of the force of interaction F_P between MP1 and MP2, by considering all spatial paths for the initial distance l_0, starting from the six paths in Section 6.2. The number of these paths will be in accordance with the rule above:

$$N^{tot} = 1+6+13+19+25+31+37+43+49+55+61 = 340 \text{ pcs} \tag{49}$$

The magnitude of the F_P interaction force is obtained from (24a) using (49):

$$\begin{aligned} F_P^{tot} &= \frac{k_p}{(l_0)^2}\left[1\times 1+0.9227\times 6+0.8541\times 13+0.793\times 19+0.738\times 25\right. \\ &\quad \left.+0.6886\times 31+0.644\times 37+0.6037\times 43\right. \\ &\quad \left.+0.567\times 49+0.5335\times 55+0.503\times 61\right] \\ &= \frac{k_p}{(l_0)^2}\left[1+5.536+11.10+15.06+18.45+21.34\right. \\ &\quad \left.+23.83+25.96+27.78+29.34+30.68\right] \\ &= \frac{k_p}{l_0^2}\times 210.10 \end{aligned} \tag{50}$$

f.1) Situation Involving the Doubled Distance ($2l_0$) in Space, with 6 Initial Paths (from Case b.1)

We now recalculate the magnitude of the force of interaction F_P between MP1 and MP2, by considering all spatial paths for the doubled initial distance $2l_0$, starting from the 6 paths in Section 6.2. The number of these paths will be in accordance with the rule above:

$$N^{tot} = 1+6+13+19+25+31 = 95 \text{ pcs} \tag{51}$$

The magnitude of the interaction force F_P is obtained from (27a) using (51):

$$\begin{aligned} F_P^{tot} &= \frac{k_p}{(2l_0)^2}\left[1\times 1+0.854\times 6+0.738\times 13+0.644\times 19\right. \\ &\quad \left.+0.567\times 25+0.503\times 31\right] \\ &= \frac{k_p}{(2l_0)^2}\left[1+5.12+9.594+12.23+14.17+15.59\right] \\ &= \frac{k_p}{(2l_0)^2}\times 57.704 = \frac{k_p}{l_0^2}\frac{1}{4}\times 57.704 = \frac{k_p}{l_0^2}\times 14.42 \end{aligned} \tag{52}$$

f.2) Situation Involving the Doubled Distance ($2l_0$) in Space, with 11 Initial Paths (from Case b.2)

We now recalculate the magnitude of the force of interaction F_P between MP1 and MP2, by considering all spatial paths for the doubled initial distance 21_0, starting from the 11 paths in Section 6.2. The number of these paths will be in accordance with the rule above:

$$N^{tot} = 1+6+13+19+25+31+37+43+49+55+61 = 340 \text{ pcs} \tag{53}$$

The magnitude of the interaction force F_P is obtained from (29a) using (53):

$$\begin{aligned} F_P^{tot} &= \frac{k_p}{(2l_0)^2}\big[1\times 1+0.9227\times 6+0.8541\times 13+0.793\times 19+0.738\times 25 \\ &\quad +0.6886\times 31+0.644\times 37+0.6037\times 43 \\ &\quad +0.567\times 49+0.5335\times 55+0.503\times 61\big] \\ &= \frac{k_p}{(2l_0)^2}\big[1+5.536+11.10+15.06+18.45+21.34 \\ &\quad +23.83+25.96+27.78+29.34+30.68\big] \\ &= \frac{k_p}{l_0^2}\frac{1}{4}\times 210.10 = \frac{k_p}{l_0^2}\times 52.52 \end{aligned} \tag{54}$$

f.3) Situation Involving the Doubled Distance ($2l_0$) in Space, with 21 Initial Paths (from Case b.3)

We now recalculate the magnitude of the force of interaction F_P between MP1 and MP2, by considering all spatial paths for the doubled initial distance 21_0, starting from the 21 paths in Section 6.2. The number of these paths will be in accordance with the rule above:

$$\begin{aligned} N^{tot} &= 1+6+13+19+25+31+37+43+49+55+61+67 \\ &\quad +73+79+85+91+97+103+109+115+121 \\ &= 340+940 = 1290 \text{ pcs} \end{aligned} \tag{55}$$

The magnitude of the F_P interaction force is obtained from (31a) using (55):

$$\begin{aligned} F_P^{tot} &= \frac{k_p}{(2l_0)^2}\big[1+0.960\times 6+0.9227\times 13+0.887\times 19+0.8541\times 25 \\ &\quad +0.8227\times 31+0.793\times 37+0.7647\times 43+0.738\times 49 \\ &\quad +0.7126\times 55+0.6886\times 61+0.6658\times 67+0.644\times 73 \\ &\quad +0.6234\times 79+0.6037\times 85+0.5849\times 91+0.567\times 97 \\ &\quad +0.5499\times 103+0.5335\times 109+0.5179\times 115+0.503\times 121\big] \\ &= \frac{k_p}{(2l_0)^2}\big[1+5.76+11.995+16.853+21.35+25.50+29.34 \\ &\quad +32.88+36.16+39.19+42.0+44.61+47.0+49.25 \\ &\quad +51.31+53.22+54.99+56.64+58.15+59.56+60.86\big] \\ &= \frac{k_p}{(2l_0)^2}(1+796.62) = \frac{k_p}{(l_0)^2}\frac{1}{4}\times 797.62 = \frac{k_p}{(l_0)^2}\times 199.40 \end{aligned} \tag{56}$$

6.4. Comparison of the Results from the Previous Situations from Sections 6.2.1 and 6.3, with Conclusions

In Sections 6.2.1 and 6.3, based on the analysis of the variation with distance l of the force of electrical interaction F_P between the two MPs (See Section 6.1.), a series of numerical calculations was performed for some particular cases involving the distance l_0 between MP1 and MP2, the limit of angle α, the spatial distribution of paths and the path deformation ε. The initial conditions and results of calculations for the forces F_P are presented in **Table 1**.

The purpose of this calculation was to establish a new correlation between the magnitude of the force F_P and the change in the distance l between MP1 and MP2. For the distance between MP1 and MP2, multiple integer values of an initial distance l_0, *i.e.* $l_0, 2l_0, 3l_0, \cdots$ were considered.

However, it was sufficient for generalization purposes to use only the first two multiples of the distance l_0, *i.e.*, l_0 and $2l_0$. For n paths l_i between MP1 and MP2, 6, 11 and 21 paths were considered, which proved to be sufficiently precise for generalization.

Table 1. Results of calculations for forces F_P from all above Cases.

Cases/Paragr.	Angα (˚)	Plan/ zone	Dist.	No. $n+1$	Deformation ε	Force F_P	Final F_P
a.1)	45	up	l_0	6	$\varepsilon = \Delta l/l_0 = 0.082$	$(1+3.35)\cdot k_p/l_0^2$	$4.35\cdot k_p/l_0^2$
a.1).s	45	up	l_0	9	$\varepsilon = \Delta l/l_0 = 0.05125$	$(1+5.432)\cdot k_p/l_0^2$	$6.432\cdot k_p/l_0^2$
a.2)	45	up	l_0	11	$\varepsilon = \Delta l/l_0 = 0.041$	$(1+6.847)\cdot k_p/l_0^2$	$7.847\cdot k_p/l_0^2$
b.1)	45	up	$2l_0$	6	$\varepsilon = \Delta l/2l_0 = 0.082$	$(1+3.306)\cdot k_p/(2l_0^2)$	$1.0765\cdot k_p/l_0^2$
b.2)	45	up	$2l_0$	11	$\varepsilon = \Delta l/2l_0 = 0.041$	$(1+6.847)\cdot k_p/(2l_0^2)$	$1.962\cdot k_p/l_0^2$
b.2).s	45	up	$2l_0$	17	$\varepsilon = \Delta l/2l_0 = 0.02562$	$(1+11.10)\cdot k_p/(2l_0^2)$	$3.045\cdot k_p/l_0^2$
b.3)	45	up	$2l_0$	21	$\varepsilon = \Delta l/2l_0 = 0.0205$	$(1+13.271)\cdot k_p/(2l_0^2)$	$3.318\cdot k_p/l_0^2$
c.1)/a.1)	45	u/d	l_0	6	$\varepsilon = \Delta l/l_0 = 0.082$	$(1+6.70)\cdot k_p/l_0^2$	$7.70\cdot k_p/l_0^2$
/a.2)	45	u/d	l_0	11	$\varepsilon = \Delta l/l_0 = 0.041$	$(1+13.694)\cdot k_p/l_0^2$	$14.694\cdot k_p/l_0^2$
/b.1)	45	u/d	$2l_0$	6	$\varepsilon = \Delta l/2l_0 = 0.082$	$(1+6.612)\cdot k_p/(2l_0^2)$	$1.934\cdot k_p/l_0^2$
/b.2)	45	u/d	$2l_0$	11	$\varepsilon = \Delta l/2l_0 = 0.041$	$(1+13.694)\cdot k_p/(2l_0^2)$	$3.673\cdot k_p/l_0^2$
/b.3)	45	u/d	$2l_0$	21	$\varepsilon = \Delta l/2l_0 = 0.0205$	$(1+26.542)\cdot k_p/(2l_0^2)$	$6.885\cdot k_p/l_0^2$
d.1)	60	up	l_0	10	$\varepsilon = \Delta l/l_0 = 0.111$	$(1+4.138)\cdot k_p/l_0^2$	$5.138\cdot k_p/l_0^2$
d.2)	60	up	$2l_0$	19	$\varepsilon = \Delta l/2l_0 = 0.055$	$(1+8.8696)\cdot k_p/(2l_0^2)$	$2.467\cdot k_p/l_0^2$
e.1)	45	cone	l_0	6	$\varepsilon = \Delta l/l_0 = 0.082$	$(1+57.29)\cdot k_p/l_0^2$	$58.29\cdot k_p/l_0^2$
e.2)	45	cone	l_0	11	$\varepsilon = \Delta l/l_0 = 0.041$	$(1+209.10)\cdot k_p/l_0^2$	$210.10\cdot k_p/l_0^2$
f.1)	45	cone	$2l_0$	6	$\varepsilon = \Delta l/2l_0 = 0.082$	$(1+56.704)\cdot k_p/(2l_0^2)$	$14.42\cdot k_p/l_0^2$
f.2)	45	cone	$2l_0$	11	$\varepsilon = \Delta l/2l_0 = 0.041$	$(1+209.10)\cdot k_p/(2l_0^2)$	$52.52\cdot k_p/l_0^2$
f.3)	45	cone	$2l_0$	21	$\varepsilon = \Delta l/2l_0 = 0.0205$	$(1+796.60)\cdot k_p/(2l_0^2)$	$199.1\cdot k_p/l_0^2$

It was intended to obtain information on the F_P force variation when changing both the above parameters: the distance l and the number of paths $n + 1$, where n represents the side paths, but not the central path.

However, in order to have comparable values for the two values of the F_P force, when both of the above parameters (number n of paths and distance l_0) change, we firstly compare the situation for the distance $2l_0$ with that for the distance l_0 (Figure 7, Figure 9).

A). For the plane situation, to highlight the effect of doubling the distance $l_0 \to 2l_0$ on F_P, the following 4 combinations of cases a.) to f.) from Table 1 are considered and compared, analysing the forces ratio $r_F = F_{P2}/F_{P1}$ for $2l_0$ and for l_0 at corresponding paths number $n + 1$, of 6, 11 and 21.

i). The plane situation with upward paths (u) with 11/6 paths, Case b.2) with F_{P2}, versus Case a.1) with F_{P1}, give the next values for the forces F_P ratio r_F:

$$r_F = F_{P2}/F_{P1} = 1.962/4.35 = 0.45 \tag{57}$$

i).s. The plane situation with upward paths (u) with 17/9 paths, Case b.2).s. with F_{P2}, versus Case a.1).s. with F_{P1}, give the next values for the forces F_P.

$$r_F = F_{P2}/F_{P1} = 3.045/6.432 = 0.473 \tag{57b}$$

One remark here that increasing the paths number $n + 1$, from 6 to 9, gives only a little influence on r_F, so the number of 6 paths utilised above is correct and sufficient.

ii). The plane situation with upward paths (u) with 21/11 paths, Case b.3) with F_{P2}, versus Case a.2) with F_{P1}, give the next values for the forces F_P.

$$r_F = F_{P2}/F_{P1} = 3.318/7.847 = 0.42 \tag{58}$$

iii). The plane situation as in c.1) with upward and downward paths (u/d) with 11/6 paths, Case c.1)/b.2) with F_{P2}, versus Case c.1)/a.1) with F_{P1}, give the next values for the forces F_P.

$$r_F = F_{P2}/F_{P1} = 3.67/7.70 = 0.47 \tag{59}$$

iv). The plane situation as in Case c.1) with upward and downward paths (u/d) with 21/11 paths Case c.1)/b.3) with F_{P2}, versus Case c.1)/a.2) with F_{P1}, give the next values for the forces F_P.

$$r_F = F_{P2}/F_{P1} = 6.8857/14.694 = 0.47 \tag{60}$$

The plane situation for the paths results in a decrease in F_{P2} of approximately 54.4% (mean ratio $r_F = 0.456$) of F_{P1}, by doubling the distance l between MPs.

However, the decrease in F_C force ratio $r_F =$ according to Coulomb's law for doubling the distance l, is:

$$r_F = F_{C2}/F_{C1} = \left[1/(2l_0)^2\right]/\left[1/(l_0)^2\right] = 1/4 = 0.25 \ll 0.456 \tag{61}$$

This indicates a decrease in F_P force with only 54.7% compared with 75.0% decrease for F_C force. Even in this case, with only incomplete plane paths, result of Coulomb's law differs markedly from Equations (57)-(60).

B). For the spatial situation with a conic at $2 \times 45^\circ$ distribution of paths, to

highlight the effect of doubling the distance $l_0 \to 21_0$ on F_P, the following two Cases from Table 1 are considered and compared.

i). The spatial situation, with 11/6 paths, Case f.2) with F_{P2}, versus Case e.1) with F_{P1}, give the next values for the forces F_P ratio r_F.

$$r_F = F_{P2}/F_{P1} = 52.52/58.29 = 0.90 \tag{62}$$

ii). The spatial situation, with 21/11 paths, Case f.3) with F_{P2}, versus Case e.2) with F_{P1}, give the next values for the forces F_P.

$$r_F = F_{P2}/F_{P1} = 199.0/210.1 = 0.947 \tag{63}$$

One remark here that the spatial situation from B), compared with the plane situation from A) gives an important favourable influence on r_F ratio, which has increased strongly, so only the spatial situation must be considered in future, which is also physically justified.

The spatial situation of paths from ii). gives an r_F ratio of F_P forces from relation (63) which indicate a diminution of F_P forces with about 5.3% (ratio 0.947), by doubling the distance between MPs.

This also must be compared with the r_F ratio of F_C forces according to Coulomb's law, where doubling the distance l_0 from (61), results in:

$$r_F = F_{C2}/F_{C1} = 0.25 \ll 0.947 \tag{64}$$

Also, in this spatial case, Coulomb's law in Equation (61) is more clearly not confirmed by result from (63).

This indicates a decrease in F_P force with only 5.3% compared with the decrease of 75.0% (ratio 0.25) for F_C force by doubling distance l_0.

It appears probable, that by increasing the number n of paths beyond $n = 21$, one could obtain a ratio $r_F = F_{P2}/F_{P1}$ greater than 0.947 or equal to 1.0, or even greater than 1.0.

However, the result from (63) provides strong support for justifying the introduction of the term $\ln r$ in the F_{CC} formula from [3].

This justification appears because, in this case of F_{CC}, the effect of doubling the distance from l_0 *to* $2l_0$ is the next:

$$\begin{aligned} r_F &= F_{CC2}/F_{CC1} = \ln(2l_0)^2 / \ln l_0^2 = 2\cdot\ln(2l_0)/2\cdot\ln l_0 \\ &= \ln 2l_0/\ln l_0 = \ln 2/\ln l_0 + 1 \end{aligned} \tag{65}$$

We observe in (65) that for long distances l_0, the first term becomes zero and the ratio r_F of F_{CC} forces tends to 1.0.

Consequently, the result from (63) is almost the same as that from (65) for long distances, and hence this result justifies the presence of the term $\ln r$ in the formula for the F_{CC} force from [1].

We remark that in any of the pairs of comparable cases above from A) and B), the condition of the equality of maximum intervals $\Delta d_2 = \Delta d_1$ was considered, between two successive paths, at the midpoint of the distance between the two MPs (Figure 8). This is the physical justification of the equivalence and comparability of any pair of paths as above from A) and B).

We observe that the result obtained in (63) for the electrical interaction force F_P between MP2 and MP1, indicates a spatial effect of the ether which leads at a limit of r_F to 1.0 in the decrease of the F_P forces ratio when doubling the distance l, in contrast to Coulomb's F_C forces whose ratio r_F decreases to 0.25 with doubling l.

But this result for F_P is in concordance with the presence of term $\ln r$ in formula of F_{CC} force from [1].

We must remark that results for all the Cases above analysed, when we doubled the distances from l_0 to $2l_0$, can be generalised for new doubled distances: $2l_0, 4l_0, 8l_0, 16l_0, 32l_0, \cdots$, when the first forces F ratio r_F, must be put at the correspondent power:

$$r_F, (r_F)^2, (r_F)^3, (r_F)^4, (r_F)^5, \cdots \tag{66}$$

In case of F_C force, the first ratio $r_F = 0.25$ put at rising powers from (66) will tend quickly to zero.

But in case of F_P force, the first ratio $r_F = 0.95, \cdots, 1.0$, put at rising powers from (66) will tend to approx. 1.0, as tends also the r_F ratio for term $\ln r$, (in 65), so being justified its presence.

The physical explanation for this result from (63) lies in the presence around MP1 and MP2 of ether cells (ECs), which transmit the percussion forces F_P, not by a single direct path but by multiple paths between MP1 and MP2, spatially distributed, but some of them simultaneously arriving at MP2, so that their effect is superposed.

These multiple forces F_P continue to arrive at MP2 at any moment in time, and hence they accumulate. The number n of paths l_i increases as the distance is doubled, compensating for the diminution of the percussion forces F_P by $1/l^2$ term.

7. Conclusions and Consequences

In this paper, we analysed the role of the ether and the effect of its presence in nature, in the form of our HM16 model, with reference to the interaction between two MPs situated at the distance l. The interaction consists of forces F_P, produced by mechanical percussions between MPs through the ether vibrations FVs, and depending on $1/l^2$. But the forces F_P, constitute in fact the so called electric Coulomb's forces F_C, between so called electric charges, which charges in fact do not exist as a physical quantity.

We have shown that the force F_P, regarded as the basic elementary electric force, can be considered as the resultant force of multiple percussions p_i on an MP. These percussions are produced by the vibrating ECs of the ether and are transmitted by the fundamental vibrations (FVs) created in ether by other MPs. Was calculated that individual F_P force given by the ether percussions at astronomical distances is practically equal with F_C, but at laboratory distance discrepancies appear, indicating the theory applicability at long distances.

An initial assessment of the all F_P forces upon an MP was made in the paper, using a simplified numerical calculation, aimed to determine the effect of all FVs travelling along various rays/paths l_i through the ether, between two MPs considered today as having electric charges.

However, a series of such paths departing in a given time interval from MP1, at different angles from the direct path to MP2, but inside an angle of 45˚, will arrive at the same moment t_0 at MP2, with the result that their individual forces F_{Pi} cumulates their effects, and so compensating the decrease of F_P due to the term in $1/l^2$.

As a result of these multiple paths and of associated forces F_{Pi}, a limited to 1.0 decrease in the final F_P force was obtained in the calculations, along with an increase in the distance l, in contrast to Coulomb's law, where F_C decreases to zero with increasing l, due to the term in $1/l^2$.

The effects of these multiple paths, of associated forces F_{Pi}, and of the spatial presence of the ether, were evaluated by numerical calculus which furnished a limit to 1.0 in the decrease of the F_P forces ratio, when doubling the distance l. This result is in contrast to Coulomb's F_C forces, whose ratio decreases to 0.25 with doubling l, and to zero after multiples doublings.

Accordingly, the possibility of including the term $\ln r$ in the F_{CC} forces was demonstrated, because the ratio of decreasing of $\ln r$ is capped also to 1.0 for doubling l at long distances.

These results justify the possibility and necessity of introducing the term $\ln r$ into the F_{CC} force in Equations (21) in [3], which will be maintained in our future analyses.

As a consequence of the above results validating the F_{CC} force formula, the electrical nature of gravity based on the electrical dipole constitution of matter, is confirmed, since numerical results given by F_{DC} force as gravity force, are very close to those gave by Newton's law force F_N [3].

Our "new gravity" theory, starting from the F_{CC} electric force in [3], involves a more complex force law of gravity, considering for this the F_{DC} force between the electrical dipoles of all matter. The formula of F_{DC} force is constituted by a series of powers of r^x, which is different from Newton's simple gravitational force F_N.

However, the new form of the gravitational force F_{DC} will explain special phenomena observed elsewhere.

The above results through F_{DC} as gravitation force, undermine the usefulness of gravity wave searches, of black hole hunting and of searches for dark matter and dark energy, which can all (among other things) be explained by the new gravity force F_{DC}.

Obviously, our overall analysis of gravity started earlier in 2000, with the admission of the existing error in Michelson's calculation [9], resulting immediately in the nonutility of Special Relativity Theory (SRT), along with the readmission of the ether into physics, according to the HM16 model. The ether presence indicates the uselessness of General Relativity (GR), and of Newton's

law force F_N, which can be replaced by the F_{DC} force, appearing between any two electrical dipoles constituents of all the matter, at any distance. But the F_{DC} force complex general equation, needs to be developed and applied to different practical situations, by physics community.

Acknowledgements

The first author acknowledges the initial advice on the subject and the encouragement of his late professor N. Barbulescu. He is sincerely grateful to the late Prof. P. Mazilu from TUCB Bucharest for his rigorous lessons on rationality. He is also indebted to Gen. Prof. G. Barsan, Col. Prof. Al. Babos from LFA Sibiu, Prof. D. Stoicescu from ULBS Sibiu, Prof. D. Siposan from MTA Bucharest and Miss Veronica Has from Bucharest, for their continued or past support. For the first developments of this theme, the authors appreciate the support of the MEC (grant under contract no. 05-D11-54/2005).

Conflicts of Interest

The authors declare no conflicts of interest regarding the publication of this paper.

References

[1] Has, I. and Miclaus, S. (2017) *Physics Essays*, **30**, 45-56. https://doi.org/10.4006/0836-1398-30.1.45

[2] Has, I., Miclaus, S. and Has, A. (2018) *Journal of Applied Mathematics and Physics*, **6**, 1886-1895. https://doi.org/10.4236/jamp.2018.69160

[3] Has, I., Miclaus, S. and Has, A. (2015) *American Journal of Modern Physics*, **4**, 97-108. https://doi.org/10.11648/j.ajmp.20150403.11

[4] Whittaker, E.T. (1910) A History of the Theories of Aether and Electricity. Longman Green and Co., London; Hodges, Figgis and Co., Dublin.

[5] Feynman, R.P. (1964) Lectures in Physics. Vol. 2: Mainly Electromagnetism and Matter. Addison-Wesley, Reading.

[6] Purcell, E.M. (1982) Electricity and Magnetism. Berkley Physics Course Vol. 2, Editura Didactica & Pedagogica, Bucharest. (In Romanian)

[7] Barbulescu, N. (1962) Elements of General Physics. Editura Didactica & Pedagogica, Bucharest. (In Romanian)

[8] Luca, E., Ciubotariu, C., Maftei, G., Zet, G., Jeflea, A. and Pasnicu, C. (1996) Physics. Vol. 2, Editura Stiintifica, Bucharest. (In Romanian)

[9] Has, I., Miclaus, S. and Has, A. (2018) *Journal of Applied Mathematics and Physics*, **6**, 1507-1521. https://doi.org/10.4236/jamp.2018.67127

Journal of Modern Physics, 2019, 10, 1125-1133
http://www.scirp.org/journal/jmp
ISSN Online: 2153-120X
ISSN Print: 2153-1196

In-Situ Study of Non-Equilibrium Charge Carriers' Behavior under Ultra-Short Pulsed Electrons Irradiation in Silicon Crystal

Hrant N. Yeritsyan[1*], Aram A. Sahakyan[1], Norair E. Grigoryan[1], Vachagan V. Harutyunyan[1], Vika V. Arzumanyan[1], Vasili M. Tsakanov[2], Bagrat A. Grigoryan[2], Gayane A. Amatuni[2]

[1]A. Alikhanyan National Science Laboratory (Yerevan Physics Institute), Department of Applied Physics, Yerevan, Armenia
[2]CANDLE Synchrotron Research Institute, Yerevan, Armenia
Email: *grant@yerphi.am

How to cite this paper: Yeritsyan, H.N., Sahakyan, A.A., Grigoryan, N.E., Harutyunyan, V.V., Arzumanyan, V.V., Tsakanov, V.M., Grigoryan, B.A. and Amatuni, G.A. (2019) *In-Situ* Study of Non-Equilibrium Charge Carriers' Behavior under Ultra-Short Pulsed Electrons Irradiation in Silicon Crystal. *Journal of Modern Physics*, **10**, 1125-1133.
https://doi.org/10.4236/jmp.2019.109072

Received: June 25, 2019
Accepted: August 3, 2019
Published: August 6, 2019

Abstract

The recombination processes for charge carriers have been studied in *n*-type silicon crystals which were irradiated by pico-second duration pulse electrons with energy of 3.5 MeV (ultrafast irradiation), and maximum dose of 3.3×10^{13} el/cm^2. *In-situ* measurements were carried out under artificial conditions simulating natural environment (space, semiconductor detectors, etc.). The observed phenomena were investigated experimentally *in-situ* using a high-speed oscilloscope equipped with a special preamplifier. Following irradiation to particular doses, some peculiarities of the recovery time of the semiconductor equilibrium condition ("characteristic time"), were obtained. Thus, it was found that the value of the "characteristic time" differs by an order of magnitude from the lifetime of the non-equilibrium (minority) charge carrier measured in an *ex-situ* regime. However, their behavior, as a function of irradiation dose, is similar and decreases with dose increase. Investigations of the dependencies of electro-physical parameters on irradiation dose, using Hall effect measurements, showed that at particular doses the radiation defects thus created, have an insignificant influence on the concentration of the charge carriers, but change their scattering properties appreciably, which affects the time parameters for the recombination of the semiconductor charge carriers. This investigation uses a novel approach to solid-state radiation physics, where *in situ* measurements were conducted in addition to conventional pre- and post-irradiation.

Keywords

Silicon Crystal, Irradiation, Recombination, Non-Equilibrium State,

Carrier Lifetime

1. Introduction

The study of recombination processes in irradiated semiconductors as a non-equilibrium state, mainly in silicon crystals, is of significance because it determines the behavior of the electro-physical parameters for these materials: conductivity, concentration and mobility of charge carriers, and a characteristic property, which is the lifetime of the minority charge carriers. The main factors that prevent the achievement of an equilibrium state under conditions of irradiation are the energetic parameters of impurity redistributions and vacancy-interstitials, both as initially present, and those which are created during irradiation [1] [2] [3] [4] [5]. These radiation defects are often responsible for the degradation of devices that contain silicon crystals, and even in the absence of degradation, the performance of a device can be impeded by the presence of defects. Those defects which have energy levels within the bandgap can act as recombination centers, and affect the carrier collection within a device. These effects can sometimes be used to advantage, since the frequency characteristics of devices may be increased by the presence of a high concentration of defects, and thus, the optical generation of THz pulses is possible, in semiconductors with sufficiently large defect densities that the carrier lifetimes are as short as a few picoseconds [4]. The radiation-induced changes in properties of the silicon used in the tracking detectors, that are employed in different areas of science and technology, mainly occur as a result of the formation and interaction of radiation defects with impurities, and these fundamentally influence the electrical parameters of the detectors, their efficiency [6] [7].

The formation of a non-equilibrium state in irradiated host crystals is well known [7] [8] [9]; however only a few initial investigations have been made using radiation applied at very short pulse durations [10] [11] [12], whereas such investigations are highly demanded both in theory and practice, particularly in space applications. The concept of a non-equilibrium state provides a basis for reinterpretation of the following radiation effects: formation of stable state of the crystal properties; differences in the radiation, thermal and time stability of materials with different impurity contents; injection of impurity atoms into the positions where intrinsic interstitial atoms are trapped; and thermal processes that occur in irradiated crystals: the latter is not feasible in the current study, because the thermal processes are not activated on the short timescale of pico-second pulse irradiation [11].

The influence of high-density pulse irradiation in current study—which results in an intensive ionization of semiconductors, with the generation of additional non-equilibrium charge carriers—is significant, since it may give rise to large non-stationary currents and electrostatic forces in electronic devices, and hence, damage them.

In the present paper we report the results from some experiments in which silicon crystals were irradiated using pico-second duration pulse electrons, to create a non-equilibrium state. This state is characterized by recombination processes, which take place in semiconductor materials and act as trapping centers for charge carriers, and are determined by the carrier lifetimes (often those of minority carriers) at the centers. In silicon, which is an indirect-bandgap semiconductor, the recombination centers are efficient when the radiation defect level is close to the middle of the bandgap, since it has a large capture cross-section for holes and electrons [13] [14]. Hence, it can be concluded that the lifetime of the minority charge carriers (τ) is the most useful parameter for the characterization of non-equilibrium processes in irradiated semiconductors, in particular, crystalline silicon. Indeed, τ is very sensitive to the effect of irradiation, and changes by an order of magnitude at low radiation doses, although the specific resistivity shows practically no change. Below the results of measurements and discussion are given.

2. Experimental Procedure and Results

Although many energy levels are created in the forbidden gap of crystalline silicon when it is irradiated, the behavior of minority charge carriers' lifetime (τ) is determined by just one or two such levels. For example, the A-centre (Oxygen atom with a complex vacancy) is the dominant radiation defect formed in silicon crystals that have been grown using the Czochralski method, which is located in the upper half (E_c-0.17 eV) of the bandgap and acts as an acceptor level in *n*-Si. The E-centre (Phosphorus atom with a complex vacancy) is the most dominant recombination centre in silicon that has been grown using the floating-zone method (doping with Phosphorus), which is located at the E_c-0.41 eV level of the bandgap and also acts as an acceptor level in *n*-Si [1].

In previous studies, we have shown that the application of pico-second duration pulse irradiation mainly generates A-centre type defects (in the form of clusters) in *n*-Si crystals [12], and in the following, we describe measurements of this center specifically. In the current paper a determination is made of the conductivity, concentration of charge carriers, their mobility, the lifetime of the minority charge carriers, in irradiated samples, and a detailed analysis of the results was made in order to elucidate the nature of the recombination centers. A standard Hall effect method [15] and a lifetime of the minority charge carriers' recombination method, based on HF (high-frequency) light-absorption [16] are used. All measurements were carried out both before and after irradiation at room temperatures.

The irradiation was performed using the linear electron accelerator AREAL at the CANDLE organization [11]. Time dependent measurements of the resistivity of the silicon crystals were made, *in-situ*, during irradiation, and the occurrence of recombination was observed on oscilloscope. The use of a stabilized current source and a high-speed oscilloscope, fitted with a preamplifier, enabled the ob-

servation of the dynamics of changes in the resistivity of the sample, with an accuracy of ±0.5 μs on the distance of 20 m. The parameters of the electron beam were: electron energy 3.5 MeV, pulse duration 4×10^{-13} s, charge 50 pico-Coulomb and the frequency was 12 Hz, which corresponds to an intensity of 10^9 el/cm^2·s. The *n*-type silicon single crystal samples were of dimension, 10 mm × 4 mm × 1 mm, and had a dual-cross form and a specific resistance of 120 Ω·cm. The irradiation scheme is presented in **Figure 1**. Following the irradiation, the main parameters of *n*-Si were again measured.

The lifetime of the minority charge carriers (τ) in Si was determined non-destructive by measuring the decay time of the signal of the recombination process of nonequilibrium charge carriers in a semiconductor. Non-equilibrium charge carriers are generated by illumination of a sample with a radiation wavelength of 1.05 μm, the decay process of which is detected by microwave absorption at a frequency of 10 GHz, which is recorded on an oscilloscope. The accuracy of the measurement is ±10% [16]. A significant aspect of these experiments is that all parameters were measured on the same sample, for both *in-situ* and *ex-situ* regimes.

Experimental results are given in **Figures 2-4**, in the form of oscilloscope pictures and dose dependences of the electro-physical parameters of the *n*-Si crystal samples. The change of resistivity of the silicon sample under *in-situ* irradiation to different doses $R = R(t)$ is presented in **Figure 2** by the oscilloscope pictures (OP). The behavior of $R = R(t)$ during pico-second pulse irradiation was characterized by a particular time, Δt, which represents the recovery time of the sample's resistivity following the irradiation pulse (see **Figure 2(a)**). It is important to note that this OP corresponds to the starting point of the irradiation process, which is about 10 seconds. It is obvious from the OP-s presented that Δt characterizes the dynamics of the crystal resistivity, and primarily depends on the initial stages of the irradiation (see $\Delta t(D)$ in **Figure 3**), and the form of the OPs can be seen to vary, along with changes in the resistivity of the crystal.

As the irradiation dose accumulates, the form and parameters of the OPs are substantially changed. It is known that the recombination processes of holes and electrons in silicon crystals are well described by an exponential function. At low irradiation doses, the initial regions of the $R = R(t)$ curves are non-linear (see **Figure 2(a)** and **Figure 2(b)**), but as the dose increases, they become nearly linear (**Figure 2(c)** and **Figure 2(d)**), which may be due to an increase in the density of radiation defects. From **Figure 2** it is clear that exponential relationship applies at the final region of the diagram, and thus it is reasonable to suppose that there is a different mechanism operating here, for the recovery of the resistivity, than exists at the initial stage.

It is apparent from **Figure 3** that both the characteristic time Δt, and the lifetime of the minority charge carriers, τ, decrease as the irradiation dose accumulates, and the $\Delta t(D)$ curve has some peculiarity. The value of Δt was found to decrease following each irradiation dose, and as a result of being stored

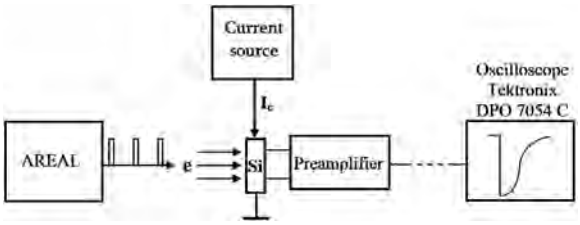

Figure 1. Schematic diagram of the sample irradiation and observation of resistivity change at *in-situ* process.

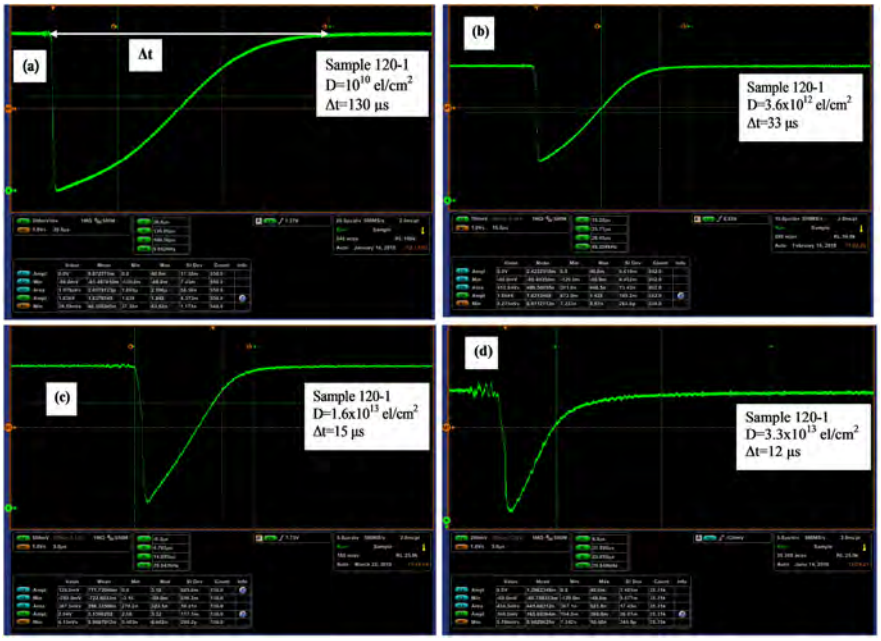

Figure 2. Oscilloscope pictures showing the dynamics of changes in the resistivity of a crystalline silicon sample, measured *in-situ* under the influence of picoseconds electron pulse irradiation: (a) at the initial stage of irradiation, (b) after irradiation to a dose of 3.6×10^{12} el/cm^2, (c) after irradiation to a dose of 1.1×10^{13} el/cm^2, (d) after irradiation to a dose of 3.3×10^{13} el/cm^2. In all cases the sample temperature was T = 300 K.

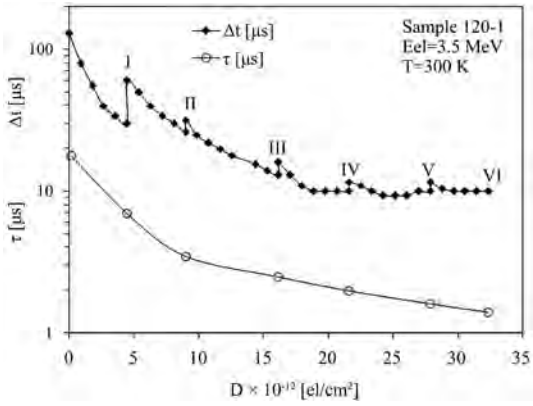

Figure 3. Pico-second electron pulse irradiation dose dependences of the characteristic time $\Delta t(D)$ and the lifetime of the minority charge carriers $\tau(D)$ in crystalline Si. On the $\Delta t(D)$ curve the values of Δt are presented in terms of defined stages of irradiation doses, and above the curve the number of stages is shown.

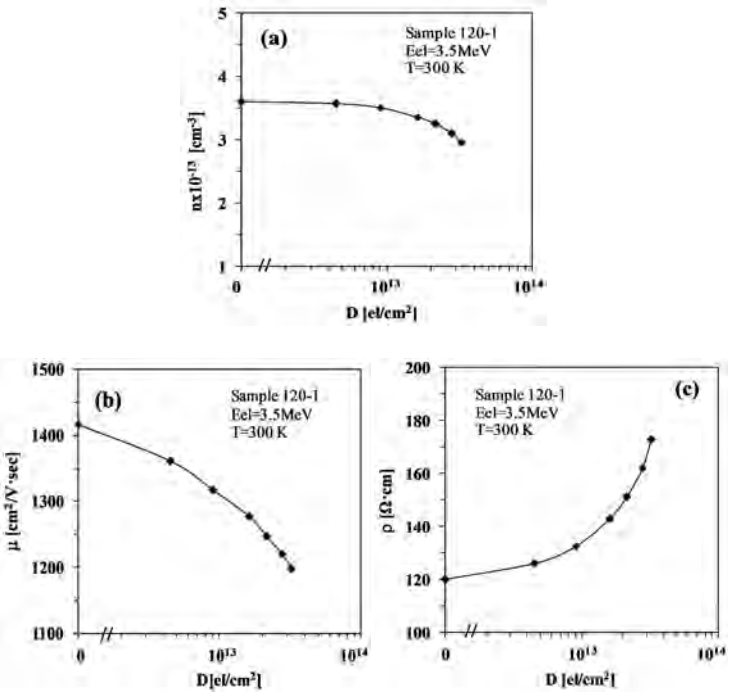

Figure 4. Pico-second electron pulse irradiation dose dependences of: (a) main charge carriers' concentration— $n(D)$, (b) mobility— $\mu(D)$ and (c) specific resistivity— $\rho(D)$ of *n*-Si with initial specific resistivity 120 Ω·cm.

for one month (stage duration) it increased significantly above the initial value. As a result of further irradiation and storage the peak decreases, and finally almost disappears as the degree of irradiation increases.

The dose dependencies of the electro-physical parameters of samples measured at room temperatures both before and after irradiation are presented in Figure 4. It can be seen that the concentration of the main charge carriers, *n*, at initial irradiation doses are practically unchanged after two stags, while the mobility $\mu(D)$ and specific resistivity $\rho(D)$ are changed significantly. Hence, at low irradiation doses, the mobility of the main charge carriers is more sensitive to the ultrafast irradiation.

3. Discussion

The transformations of defect complexes may occur by direct interaction with vacancies, interstitials or impurities. Since the impurity concentrations often are higher than the saturation limit, a redistribution of the concentrations of the impurities may occur in sites and interstitial positions, and interact with point crystal defects to form defect complexes such as A- or E-centers, or other defects that involve the participation of the impurity atoms. Hence, the displacement of impurity atoms from the lattice sites in interstitial positions will occur in any crystal with impurity concentrations higher than at the non-equilibrium state and this process will become more important for higher concentrations of impurities and will be dependent on the conditions (e.g. dose) of the irradiation.

We offer an explanation of the observed phenomena, which relate to the time-scales of the recombination processes, in terms of an annealing of meta-stable radiation defects at room temperatures, and the establishment of an equilibrium condition of the crystal with stable defects, *i.e.* "steady state" of the silicon crystal. The behavior of lifetime $\tau(D)$ in **Figure 3** corresponds with results reported in the literature (without any peculiarity) and is explained by a decrease in τ as the concentration of radiation defects increases, which are created by irradiation, as a result of a more effective trapping of minority charge carriers [10] [13]. The analogous dependences of both $\Delta t(D)$ and $\tau(D)$ emphasize that a process occurs involving the recombination of charge carriers, in result of irradiation, which achieves "steady state" after defined irradiation dose (in this case, 3.3×10^{13} el/cm^2). It is possible that different factors may influence the outcome of illumination of a sample with radiation of a 1.05 μm wavelength, in the case of τ measurements, while it is the Δt parameter which is being determined *in-situ* during irradiation by electrons with energy of 3.5 MeV, *i.e.* there are different crystal excitation mechanisms in operation. It is possible that the pico-second duration pulse irradiation may create some plasma effects in the crystals, and thus influence their properties as a result of a significantly high density of radiation defects, a subject which we intend to explore in additional investigations.

It has been mentioned in the literature [17] [18] [19] that a divacancy type radiation defect is the main trap for free charge carriers, and its formation in irradiated Si crystals leads to an increase in the resistivity of the material which is an amphoteric center and has three energy levels in the Si bandgap. However, in our experiments, despite the fact that the resistivity increases during irradiation, three energy levels were not observed and we consider that A-centers are the main recombination centers for minority charge carriers. In any case, it is more likely that divacancy type radiation defects will be created in silicon, by irradiation with very high energy electrons (higher than 10 MeV), neutrons or protons [18] [19] [20].

4. Conclusions

Thus, the *in-situ* observation of the behavior of the electro-conductivity for silicon crystals under conditions of pico-second duration pulse electron irradiation with an energy of 3.5 MeV, suggests that the transition of the crystal from a non-equilibrium state to a "steady state", takes place by a process involving the recombination of charge carriers, and has some particular characteristic which is a consequence of their interaction times.

1) The value of the "characteristic time", $\Delta t(D)$, observed under *in-situ* condition is 10 times higher than the lifetime of the minority charge carriers $\tau(D)$, measured at *ex-situ*, despite the fact that both decrease with increasing irradiation dose.

2) Meta-stable defects were observed, which can be annealed at room temper-

ature, and the irradiation dose at which this phenomenon disappeared (3.3×10^{13} el/cm^2), *i.e.* when a "steady state" occurs, was determined.

3) It was shown that at low doses of pico-second pulse irradiation, the specific resistivity change of silicon is determined by the mobility of the charge carriers, rather than by their concentration.

4) Detailed analysis of the OPs demonstrated that there is additional process that influences the relaxation during the recovery of the equilibrium state under irradiation of crystalline silicon.

5) Future investigations are planned with theoretical interpretation to elucidate the physical nature of the Δt parameter because it may reveal behavior of semiconductor materials and devices operating in the real processes.

Acknowledgements

The authors acknowledge support of this work by the State Committee of Science of the Ministry of Education and Science Republic of Armenia, in the framework of the research project grant No. 17A-1C002. The authors are thankful to Christopher Rhodes for useful discussion.

Conflicts of Interest

The authors declare no conflicts of interest regarding the publication of this paper.

References

[1] Hallen, A., Keskitalo, N., Masszi, F. and Nagl, V. (1996) *Journal of Applied Physics*, **79**, 3906. https://doi.org/10.1063/1.361816

[2] Emtsev, V.V. and Mashovets, T.V. (1981) Impurities and Point Defects in Semiconductors. Radio I Svyaz, Moscow, 248 p. (In Russian)

[3] Takakura, K., Ohyama, H., Murakawa, H., Yoshida, T., *et al.* (2004) *Journal of Applied Physics*, **27**, 133. https://doi.org/10.1051/epjap:2004058

[4] Krotkus, A. (2010) *Journal of Physics D: Applied Physics*, **43**, Article ID: 273001. https://doi.org/10.1088/0022-3727/43/27/273001

[5] Mukashev, N., Abdullin, K.A., *et al.* (2000) *Rus. Usp. Phys. Nauk*, **170**, 143.

[6] Radu, R., Pintilie, I., Nestor, L.C., *et al.* (2015) *Journal of Applied Physics*, **117**, Article ID: 164503. https://doi.org/10.1063/1.4918924

[7] Lee, Y.H., Brosious, P.R. and Corbett, J.W. (1974) *Physical Review B*, **9**, 4351. https://doi.org/10.1103/PhysRevB.9.4351

[8] Smirnov, L.S., Bolotov, V.V. and Vasilyev, A.V. (1979) The Effect of Semiconductor Crystals Unequilibrium State on Radiation Processes. *International Conference on Radiation Physics of Semiconductors and Related Materials*, Tbilisi, 13-19 September 1979, 334-337.

[9] Makarov, V.A. and Ukhin, N.A. (1979) The Influence of Particle Energy on the Efficiency of Recombination Rate Change in Si and Ge. *International Conference on Radiation Physics of Semiconductors and Related Materials*, Tbilisi, 13-19 September 1979, 410-413.

[10] Dvurechenski, A.V., Kashnikov, B.P. and Smirnov, L.S. (1979) Defects in Silicon Irradiated with High Current Density Electron Pulses. *International Conference on Radiation Physics of Semiconductors and Related Materials*, Tbilisi, 13-19 September 1979, 305-307.

[11] Yeritsyan, H.N., Sahakyan, A.A., Grigoryan, N.E., Harutyunyan, V.V., Tsakanov, V.M., Grigoryan, B.A., Amatuni, G.A., Petrosyan, V.H., Khachatryan, A.A. and Rhodes, C.J. (2018) *Journal of Electronic Materials*, **47**, 4010-4015. https://doi.org/10.1007/s11664-018-6286-6

[12] Yeritsyan, H.N., Sahakyan, A.A., Grigoryan, N.E., Harutyunyan, V.V., Khachatryan, A.A., Grigoryan, B.A., Avagyan, V.S., Amatuni, G.A. and Vardanyan, A.S. (2016) *Journal of Modern Physics*, **7**, 1413. https://doi.org/10.4236/jmp.2016.712128

[13] Konopleva, R.F. and Ostroumov, V.I. (1975) The Interaction of High Energy Charged Particles with Silicon and Germanium. Atom-Edition, Moscow, 128 p.

[14] Schroder, K. (1997) *IEEE Transactions on Electron Devices*, **44**, 160-170. https://doi.org/10.1109/16.554806

[15] Kauppinen, H., Korbel, C. and Skog, C. (1997) *Physical Review B*, **55**, 9598. https://doi.org/10.1103/PhysRevB.55.9598

[16] Eremin, V., Ivanov, A., *et al.* (1999) *Nuclear Instruments and Methods in Physics Research Section A*, **426**, 120. https://doi.org/10.1016/S0168-9002(98)01479-X

[17] Poiler, V.A., Dannefaer, S. and Schiettekatte, F. (2003) *Nuclear Instruments and Methods in Physics Research Section B*, **206**, 85. https://doi.org/10.1016/S0168-583X(03)00686-4

[18] Kozlovski, V.V. and Kozlov, V.A. (2001) *Semiconductors*, **35**, 735. https://doi.org/10.1134/1.1385708

[19] Wondrak, W., Bethke, K. and Silber, D.G. (1987) *Journal of Applied Physics*, **62**, 3464. https://doi.org/10.1063/1.339289

[20] Lang, D.V. (1977) Point Radiation Defects in Semiconductors. *Proceedings International Conference on Radiation Defects in Semiconductors*, Dubrovnik, Institute of Phys. Conf. Ser. 31, 70-94.

Journal of Modern Physics, 2019, 10, 1134-1143
http://www.scirp.org/journal/jmp
ISSN Online: 2153-120X
ISSN Print: 2153-1196

Imaginary Time Density Functional Calculation of Ground States of Atoms Using CWDVR Approach

Naranchimeg Davgiikhorol[1], Munkhsaikhan Gonchigsuren[1*], Khenmedekh Lochin[1], Sukh Ochir[1], Tsogbadrakh Namsrai[2]

[1]Department of Physics, School of Applied Sciences, Mongolian University of Science and Technology, Ulaanbaatar, Mongolia
[2]Department of Physics, School of Arts and Sciences, National University of Mongolia, Ulaanbaatar, Mongolia
Email: *gmunkhsaikhan@must.edu.mn

How to cite this paper: Davgiikhorol, N., Gonchigsuren, M., Lochin, K., Ochir, S. and Namsrai, T. (2019) Imaginary Time Density Functional Calculation of Ground States of Atoms Using CWDVR Approach. *Journal of Modern Physics*, **10**, 1134-1143.
https://doi.org/10.4236/jmp.2019.109073

Received: June 17, 2019
Accepted: August 3, 2019
Published: August 6, 2019

Abstract

The self-consistent Kohn-Sham equations for many-electron atoms are solved using the Coulomb wave function Discrete Variable Method (CWDVR). Wigner type functional is used to incorporate correlation functional. The discrete variable method is used for the uniform and optimal spatial grid discretization and solution of the Kohn-Sham equation. The equation is numerically solved using the CWDVR method. First time we have reported the solution of the Kohn-Sham equation on the ground state problem for the many-electronic atoms by the CWDVR method. Our results suggest CWDVR approach shown to be an efficient and precise solution of ground-state energies of atoms. We illustrate that the calculated electronic energies for He, Li, Be, B, C, N and O atoms are in good agreement with other best available values.

Keywords

Density Functional Theory, Effective Potential, Electronic Energies, Kohn-Sham Equation

1. Introduction

Numerical approach of many-electron systems is extremely difficult computation. Density functional theory (DFT) [1] [2] is a computational quantum mechanical modeling method used to investigate many-electron systems, in particular atoms, molecules, and the condensed phases [3] [4]. It provides a powerful alternative technique to ab-initio wave function approach, since the electron density $\rho(\boldsymbol{r})$ possesses only three spatial dimensions no matter how large the

system is. The DFT proves accurate and computationally much less expensive than usual ab-initio wave function methods, such as a Hartree Fock method. However, the majority of the applications are restricted to the ground states. The exchange-correlation energy functional, which is a functional of the total electron density, is not known exactly, and thus approximate exchange-correlation energy functional must be used. Moreover, while the highest-occupied orbital energy corresponds to the negative of the ionization potential for well-behaved potentials vanishing at infinity, energies of other occupied and unoccupied orbitals have no rigorous correspondence to the excitation energies. Nevertheless, it has been shown recently [5] that the unoccupied true Kohn-Sham eigenvalues can also provide good excitation energies which the commonly used approximate density functionals usually do not satisfy. Nevertheless, numerous attempts [3] [6] have been made in this direction over the years; the ensemble density functional method [7] [8] [9] [10] [11], the method based on partitioning of the wave function, the time-dependent density functional theory (TDDFT) approach [12] [13] [14] [15]. The DFT based upon the Hohenberg-Kohn (HK) energy functional [3] [4] focuses on the solution of exchange-correlation energy and it had been used in many calculations of ground state properties an atomic system. An efficient and accurate grid method for solving the time-dependent Schrödinger equation for an atomic system interacting with an intense laser pulse has been shown by Liang-Y.Peng and A.F. Starace [16]. Instead of the usual finite difference (FD) method, the radial coordinate is discretized using the discrete variable representation (DVR) constructed from Coulomb wave functions. The DVR method has its origin in the transformation method devised by Harris *et al.* [17], where it was further developed by Dickinson and Certain [18]. Light *et al.* [19] first explicitly used the DVR method as a basis representation for quantum problems, where after different types of DVR methods have found wide applications in different fields of physical and chemical problems. The DVR method gives an idea; associated basis functions are localized about discrete values of the coordinate under consideration. The DVR simplifies the evaluation of Hamiltonian matrix elements. The matrix elements of kinetic energy can also be calculated very simply and analytically in most cases [20]. Since the CWDVR method is able to treat the Coulomb singularity naturally, it is suitable for atomic systems [16]. The Kohn-Sham equation is shown to be solved by the Coulomb wave function discrete variable representation method.

To the best of our knowledge, no one reported the solution of the Kohn-Sham equation on the ground state problem for the many-electronic atoms by the CWDVR method. Furthermore, we accurately present the ground state energies of the many-electronic atoms by the CWDVR method.

This paper consists of methodology and results obtained within the CWDVR method. We show that ground state energy values calculated by the present method are in good agreement with other precise theoretical calculations. Finally, we present conclusions. Here, atomic units (a.u.) are used throughout this paper unless otherwise specified.

2. CWDVR Method

In this section, we first give a brief introduction to the DVR constructed from orthogonal polynomials and Coulomb wave functions, which will be used to solve the Kohn-Sham equation for many-electron atomic systems. The DVR approach basis functions can be constructed from any complete set of orthogonal polynomials, defined in the domain with the corresponding weight function [21].

It is known that a Gaussian quadrature can also be constructed using nonclassical polynomials. The DVR derived from the Legendre polynomials has been shown by Machtoub and Zhang [22] to provide very precise results for the metastable states of the exotic helium atom. An appropriate quadrature rule for the Coulomb wave function was given by Dunseath *et al.* [23] with explicit expressions for the weights.

It is known that a Gaussian quadrature can also be constructed using nonclassical polynomials. The DVR derived from the Legendre polynomials has been shown by Machtoub and Zhang [22] to provide very precise results for the metastable states of the exotic helium atom. An appropriate quadrature rule for the Coulomb wave function was given by Dunseath *et al.* [23] with explicit expressions for the weights.

The time dependent single particle Kohn-Sham equation has the form

$$i\frac{\partial \psi_j(\boldsymbol{r},t)}{\partial t} = \left(\hat{H}_0 + \upsilon_{eff}\right)\psi_j(\boldsymbol{r},t),\ j = \overline{1,N} \tag{1}$$

here, $\psi(\boldsymbol{r},t)$ is the single particle Kohn-Sham orbit of N electron atom, $\hat{H}_0$ —atomic Hamiltonian, υ_{eff} is the time dependent effective potential, and charge density depends on the coordinates and time and is given by

$$\rho(\boldsymbol{r}) = \sum_{j=1}^{N}\left|\psi_j(\boldsymbol{r})\right|^2 \tag{2}$$

However, one can write Equation (1) in imaginary time τ and substitute $\tau = -it$, t being the real time, to obtain a diffusion-type equations:

$$-\frac{\partial R_j(\boldsymbol{r},t)}{\partial t} = \left(-\frac{1}{2}\nabla^2 + \upsilon_{eff}\right)R_j(\boldsymbol{r},t). \tag{3}$$

The Kohn-Sham effective local potential contains both classical and quantum potentials and can be written as:

$$\upsilon_{eff}\left[\rho;\boldsymbol{r},t\right] = \frac{\delta E_{ee}}{\delta\rho} + \frac{\delta E_{ne}}{\delta\rho} + \frac{\delta E_{xc}}{\delta\rho} + \frac{\delta E_{ext}}{\delta\rho}. \tag{4}$$

here; the first term is inter-electronic Coulomb repulsion, the second is the electron-nuclear attraction term, the third is exchange-correlation term, and last term comes from interaction with the external field (in the present case, this interaction is zero). A simple local energy functional form has been applied for the atoms, and the exchange part can be found to be [24],

$$\frac{\delta E_x}{\delta\rho}=\frac{\delta E_x^{LDA}}{\delta\rho}-\beta\left[\frac{\frac{4}{3}\rho^{1/3}+\frac{2}{3}\frac{r^2\rho}{\alpha_x}}{\left(1+\frac{r^2\rho^{2/3}}{\alpha_x}\right)^2}\right] \tag{5}$$

$$\frac{\delta E_x^{LDA}}{\delta\rho}=-\frac{4}{3}C_x\rho^{1/3}. \tag{6}$$

The simple local parameterized Wigner-type correlation energy functional [25] used for ground states:

$$E_c=-\int\frac{\rho}{a+b\cdot\rho^{-1/3}}\mathrm{d}\boldsymbol{r} \tag{7}$$

$$\frac{\delta E_c}{\delta\rho}=-\frac{a+c\cdot\rho^{-1/3}}{\left(a+b\cdot\rho^{-1/3}\right)^2} \tag{8}$$

where: $a=9.81$, $b=21.437$, $c=28.582667$ are respectively.

The solution of Equation (1) is used split time method, for split time Δt. It can be written

$$R(\boldsymbol{r},t+\Delta t)\cong \mathrm{e}^{-\Delta t\hat{H}_0/2}\mathrm{e}^{-\hat{V}\Delta t}\mathrm{e}^{-_0\Delta t\hat{H}/2}R(\boldsymbol{r},t) \tag{9}$$

One of the main features of the DVR is that a function $R(\boldsymbol{r},t)$ can be approximated by interpolation through the given grid points:

$$R(r)\cong\sum_{j=0}^{N}R(r_j)g_j(r) \tag{10}$$

here: $R(r_j)$ is the interpolation function, $g_j(r)$ is the cardinal function.

The Coulomb wave function is defined by radial grid points. Interpolation function is obtained by using the radial function that is derived from the cardinal functions.

By noting that $F(r)$ is the Coulomb function, $F'(r)$ is the first derivative from $F(r)$ at the position r_j, ψ_j is found to be $\psi_j=R(r)/F'(r)$.

The propagation in the energy space (step first in equation) can now be achieved through

$$\mathrm{e}^{-\hat{H}_0\Delta t/2}R(r)=\sum_{j=0}^{N}\mathrm{e}^{-\hat{H}_0\Delta t/2}R(r_j)g_j(r). \tag{11}$$

The cardinal functions $g_j(r)$ in Equation (10) are given by the following expression

$$g_j(r)=\frac{1}{F'(r_j)}\frac{F(r)}{r-r_j} \tag{12}$$

where the points $r_j\ (j=1,2,\cdots,N)$ are the zeros of the Coulomb wave function $F(r)$ and $F'(r_j)$ stands for its first derivative at r_j and $g_j(r)$ satisfies the cardinality condition

$$g_j(r_i)=\delta_{ij}. \tag{13}$$

Since the Coulomb wave functions was expressed in quadrature rule with expressions for the weight ω_j, then DVR basis function $F_j(r)$ satisfies the eigenvalue for the radial Kohn-Sham type equation:

$$\hat{H}(r)\psi(r) = E\psi(r) \tag{14}$$

and

$$\hat{H}(r) = -\frac{d^2}{2d^2} + V(r). \tag{15}$$

The DVR greatly simplifies the evaluation of Hamiltonian matrix elements. The potential matrix elements involve merely the evaluation of the interaction potential at the DVR grid points, where no integration is needed.

The DVR basis function $f_j(r)$ is constructed from the cardinal function g_j as follows

$$f_j(r) = \frac{1}{\sqrt{\omega_j}} g_j(r), \tag{16}$$

here the weight ω_j is given by [23]:

$$\omega_j \approx \frac{\pi}{a_j^2}. \tag{17}$$

$$a_j = F'(r_j) \tag{18}$$

The second derivative of the cardinal function g_j'' is given,

$$g_j''(r_j) = \delta_{jk}\frac{c_k}{3a_k} - (1-\delta_{jk})\frac{a_k}{a_j}\frac{2}{(r_k - r_j)^2}, \tag{19}$$

where a_k is given by Equation (18) and c_k. Here kinetic energy matrix elements D_{ij} calculated using:

$$c_k = -a_k(2E + 2Z/r), \tag{20}$$

$$D_{ij} = -\delta_{ij}\frac{c_i}{6a_i} + (1-\delta_{ij})\frac{1}{(r_i - r_j)^2}. \tag{21}$$

In the Equation (15), to expand $R(r_j)$ in the eigenvectors of the Hamiltonian $\hat{H}_0$, we first solve the eigenvalue problem for $\hat{H}_0$ after discretization of coordinate, the differential equation for this problem can be written as:

$$\sum_{j=1}^{N}\left[-\frac{1}{2}D_{ij} + V(r_j)\delta_{ij}\right]\varphi_{kj} = \varepsilon_k\varphi_{kj} \tag{22}$$

here D_{ij} denotes the symmetrized second derivative of the cardinal function that is given as,

$$(D_2)_{ij} = \frac{1}{3}\left(E + \frac{Z}{r}\right), i = j \tag{23}$$

$$(D_2)_{ij} = \frac{1}{(r_j - r_i)^2}, i \neq j \tag{24}$$

Equation (2) is then numerically solved to achieve a self-consistent set of orbitals, using the DVR method. These orbitals are used to construct various Slater determinants arising out of that particular electronic configuration and its energies computed in the usual manner.

A key step in the time propagation of Equation (9) is to construct the evolution operator $e^{-\hat{H}_\ell^0 \Delta t/2} \cong S(\ell)$ through an accurate and efficient representation of $\hat{H}_\ell^0$. Here we extend the DVR method to achieve optimal grid discretization and an accurate solution of the eigenvalue problem of $\hat{H}_\ell^0$.

In the present work, we are particularly interested in the exploration of the improvement of the Kohn Sham type equation in electron structure calculation. Thus we choose the Slater wave function as our initial state at $t = 0$. Note that, the differential equation for time propagation is normalized at each time step. Here the 152 grid points are used for the DVR discretization of the radial coordinates and $\Delta t = 0.001$ a.u, with 500 iterations is used in the time propagation to achieve convergence.

3. Results and Discussions

In this section we present results from nonrelativistic electronic structure calculation of the ground states of He, Li, Be, B, C, N and O atoms. Wolfram Mathematica Software has used for the calculations. Here, parameters of the Coulomb wave function such as wave number and effective charges are chosen to be $k = \sqrt{2E} = 3$ and $Z = 400$. Table 1 summarizes the main results for the mentioned atoms. The first row shows the present results. The results from the Amlan

Table 1. Calculated ground-state properties of He, Li, Be, B, C, N and O atoms (in au) along with literature data for comparison.

		He	Li	Be	B	C	N	O
−E	Present work	2.900	7.3197	14.582	24.779	37.9484	55.625	74.795
	Hartree-Fock [3]	2.8617	7.4332	14.573	24.529	37.688	54.400	74.809
	Roy [26]	2.8973	7.221	14.221	23.964	36.953	53.407	73.451
−Z/r	Present work	6.853	17.054	33.447	56.728	88.447	128.915	178.317
	Hartree-Fock [3]	6.749	17.115	34.072	58.143	88.649	127.326	176.324
−Ex	Present work	1.039	1.752	2.656	3.732	5.0416	6.527	8.223
	Hartree-Fock [3]	1.026	1.781	2.667	3.744	5.045	6.596	8.174
	Roy [26]	1.032	1.574	2.404	3.478	4.640	5.987	7.490
−Ec	Present work	0.0424	0.0659	0.093	0.1252	0.1637	0.2058	0.2524
	Hartree-Fock [3]	0.0423	0.0435	0.094	0.111	0.1560	0.1890	0.2412
	Roy [26]	0.0423	0.154	0.322	0.302	0.368	0.434	0.543
T	Present work	2.960	7.301	14.172	23.888	37.301	53.536	74.825
	Hartree-Fock [3]	2.8617	7.433	14.573	24.529	37.688	54.401	74.810
	Roy [26]	2.8974	7.382	14.844	25.300	37.924	53.664	73.444

K Roy [26] for energies for the ground states for He, Li, Be, B, C, N and O atoms are shown below the present results. The corresponding Hartree-Fock values from the literature are listed for comparison. For all atoms considered, we found the present results of the total electronic energies considerably match the Hartree-Fock values and are significantly better than the results from Amlan K Roy [26].

It is satisfying that the CWDVR approach can be used to perform a high precision calculation of the Kohn-Sham type equation with the use of only a few grid points.

Analyses of the results for exchange and correlation energies are given in the same table separately. The results from exchange energies (Ex) calculations of the present calculations show a good agreement with the Hartree-Fock results [3]. For the Be, B, C and O atoms, the calculated exchange energy is nearly exact, while for He, Li and N, there is an underestimation by 1.05% - 1.63%. The calculated exchange energy for He and N gives close results to Amlan J Roy, underestimated about 0.68% - 1.05%, the rest atoms are being the worst case. This indicates that the simple local exchange functional in Equation (5) is well accurate, compared to those of Amlan J Roy [26], which show a closer agreement with Hartree-Fock exchange energies.

The "exact" correlation energies are considered for the Li, Be, B, C, N and O atoms in **Table 1** due to the comparison with other results. The Wigner-type correlation energy functional likely seems to be sufficiently enough for the systems considered. Compared with Hartree-Fock results for He, Be, C and O atoms, it is nearly exact, otherwise underestimated by about 0.24% - 4.94%; the Li, B and N atoms are being the worst case. The calculated correlation energy for He atom is nearly exact to Amlan J Roy, but worse results for other atoms.

We note that the primary purpose of this work is to explore the feasibility of extending the CWDVR to the solution of the Kohn-Sham type differential equation with imaginary time propagation. LDA-type xc energy functional can be easily adopted in the present CWDVR approach.

Table 1 shows that the virial theorem is nearly satisfied for all atoms. The calculated kinetic energy term for the O atom is reasonably exact to Hartree-Fock, while for rest atoms there is an underestimation by 1.03% - 3.44%.

The results for total energies are given in the same table separately. The results from total energies calculations of the present calculations show a good agreement with the Hartree-Fock results [3]. For the Be, and O atoms, the calculated exchange energy is nearly exact, while for rest atoms there is an underestimation by 1.02% - 2.25%. This indicates that the total energy functional is well accurate, compared to those of Amlan J Roy [26], which show a closer agreement with Hartree-Fock total energies.

Results from the calculations of radial densities of atoms were created images of correspondent plots. Examples of radial density plots are shown in **Figure 1** and **Figure 2**. In **Figure 1**, we report the radial density plots for beryllium. The inset (a) reports the result from the present calculation; the inset (b) shows the

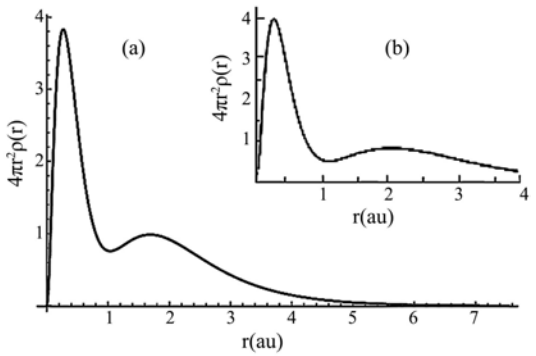

Figure 1. Radial density plot of Be (in au). The inset (a) reports the result from the present calculation; the inset (b) shows the Hartree-Fock plot for comparison.

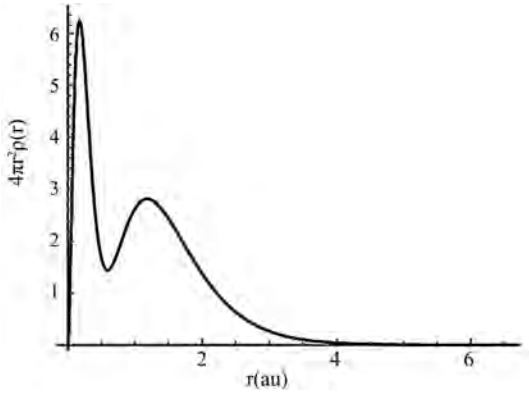

Figure 2. Radial density plot of C (in au) obtained from the present calculation.

Hartree-Fock plot for comparison. Here, the radial density plot shape from our calculation is in good agreement with Hartree-Fock plot [3].

Figure 2 shows the radial density plot for carbon. We note that the radial density of carbon calculated maintain the expected shell structure and closely resemble the Hartree-Fock density, where Hartree-Fock plot is not shown.

4. Conclusion

In this paper, we present that nonrelativistic ground-state properties of He, Li, Be, B, C, N and O atoms can be calculated by means of time-dependent Kohn-Sham equations and an imaginary time evolution methods. The CWDVR approach is shown to be an efficient and precise solution of ground-state energies of atoms. The calculated electronic energies are in good agreement with the Hartree-Fock values and are significantly better than the results in the literature [26]. The approach likely opens a road to the solution of ionization and excitation states of many electron atoms.

Acknowledgements

This work was supported by the Science Technology Foundation Project (Code:

ShUS-2019/08) of Mongolia.

Conflicts of Interest

The authors declare no conflicts of interest regarding the publication of this paper.

References

[1] Hohenberg, P. and Kohn, W. (1964) *Physical Review*, **136**, B864. https://doi.org/10.1103/PhysRev.136.B864

[2] Kohn, W. and Sham, L.J. (1965) *Physical Review*, **140**, A1133. https://doi.org/10.1103/PhysRev.140.A1133

[3] Parr, R.G. and Yang, W. (1989) Density-Functional Theory of Atoms and Molecules. Oxford Univ. Press, New York.

[4] Gross, E.K.U. and Dreizler, R.M. (1995) Density Functional Theory. Plenum, New York.

[5] Savin, A., Umrigar, C.J. and Gonze, X. (1998) *Chemical Physics Letters*, **288**, 391-395. https://doi.org/10.1016/S0009-2614(98)00316-9

[6] Singh, R. and Deb, B.M. (1999) *Physics Reports*, **311**, 47. https://doi.org/10.1016/S0370-1573(98)00081-7

[7] von Barth, U. (1979) *Physical Review A*, **20**, 1693. https://doi.org/10.1103/PhysRevA.20.1693

[8] Ziegler, T., Rauk, A. and Baerends, E.J. (1977) *Theoretica Chimica Acta*, **43**, 261. https://doi.org/10.1007/BF00551551

[9] Ziegler, T. (1991) *Chemical Reviews*, **91**, 651. https://doi.org/10.1021/cr00005a001

[10] Daul, C. (1994) *International Journal of Quantum Chemistry*, **52**, 867. https://doi.org/10.1002/qua.560520414

[11] Nagy, A. (1991) *Journal of Physics B*, **24**, 4691. https://doi.org/10.1088/0953-4075/29/3/007

[12] Petersilka, M., Gossmann, U.J. and Gross, E.K.U. (1996) *Physical Review Letters*, **76**, 1212. https://doi.org/10.1103/PhysRevLett.76.1212

[13] Petersilka, M. and Gross, E.K.U. (1996) *International Journal of Quantum Chemistry*, **60**, 181. https://doi.org/10.1002/(SICI)1097-461X(1996)60:7<1393::AID-QUA21>3.0.CO;2-4

[14] Casida, M.E., Jamorski, C., Casida, K.C. and Salahub, D.R. (1998) *The Journal of Chemical Physics*, **108**, 4439. https://doi.org/10.1063/1.475855

[15] Grabo, T., Petersilka, M. and Gross, E.K.U. (2000) *Journal of Molecular Structure: THEOCHEM*, **501**, 353. https://doi.org/10.1016/S0166-1280(99)00445-5

[16] Peng, L.-Y. and Starace, A.F. (2006) *The Journal of Chemical Physics*, **125**, Article ID: 154311. https://doi.org/10.1063/1.2358351

[17] Harris, D.O., Engerholm, G.G. and Gwinn, W.D. (1965) *The Journal of Chemical Physics*, **43**, 1515. https://doi.org/10.1063/1.1696963

[18] Dickinson, A.S. and Certain, P.R. (1968) *The Journal of Chemical Physics*, **49**, 4209-4211. https://doi.org/10.1063/1.1670738

[19] Lill, J.V., Parker, G.A. and Light, J.C. (1982) *Chemical Physics Letters*, **89**, 483. https://doi.org/10.1016/0009-2614(82)83051-0

[20] Heather, R.W. and Light, J.C. (1983) *The Journal of Chemical Physics*, **79**, 147. https://doi.org/10.1063/1.445574

[21] Baye, D. and Heenen, P.H. (1986) *Journal of Physics A*, **19**, 2041. https://doi.org/10.1088/0305-4470/19/11/013

[22] Machtoub, G. and Zhang, C. (2002) *International Journal of Theoretical Physics*, **41**, 293. https://doi.org/10.1023/A:1014010923548

[23] Dunseath, K.M., Launay, J.M., Terao-Dunseath, M. and Mouret, L. (2002) *Journal of Physics B*, **35**, 3539. https://doi.org/10.1088/0953-4075/35/16/313

[24] Deb, B.M. and Chattaraj, P.K. (1989) *Physical Review A*, **39**, 1696. https://doi.org/10.1103/PhysRevA.39.1696

[25] Roy, A.K. and Chu, S.-I. (2002) *Journal of Physics B*: *Atomic*, *Molecular and Optical Physics*, **35**, 2075-2086.

[26] Roy, A.K. (2011) *Journal of Mathematical Chemistry*, **49**, 1687-1699. https://doi.org/10.1007/s10910-011-9851-2

Journal of Modern Physics, 2019, 10, 1144-1148
http://www.scirp.org/journal/jmp
ISSN Online: 2153-120X
ISSN Print: 2153-1196

A Universe Comprised of 50% Matter Mass-Energy and 50% Dark Energy

Eugene Terry Tatum

Bowling Green, KY, USA

Email: ett@twc.com

How to cite this paper: Tatum, E.T. (2019) A Universe Comprised of 50% Matter Mass-Energy and 50% Dark Energy. *Journal of Modern Physics*, **10**, 1144-1148.
https://doi.org/10.4236/jmp.2019.109074

Received: July 17, 2019
Accepted: August 11, 2019
Published: August 14, 2019

Abstract

The new C.G.S.I.S.A.H. theory of dark matter is used to appropriately classify and quantitate the previously-overlooked cold ground state neutral atomic hydrogen within the intergalactic vacuum. A surprising discovery is demonstrated in the Results section that approximately one-fifth of the cosmic critical density can be attributable to intergalactic cold ground state neutral atomic hydrogen. By subtracting this quantity of the critical density from the dark energy ledger column and adding it to the total matter mass-energy ledger column, our current universe appears to be equally proportioned between total matter mass-energy and dark energy. This has been a longstanding prediction of the Flat Space Cosmology model.

Keywords

Dark Matter, Dark Energy, CGSISAH Theory, Flat Space Cosmology, Dirac Sea, Intergalactic Medium, Interstellar Medium, ΛCDM Concordance Model

1. Introduction and Background

Before 1998, the energy density of the universe was believed to be wholly comprised of approximately 5% visible matter (*i.e.* the visible stars, warm molecular gas clouds and cosmic dust), an unknown quantity of dark matter within and haloed around the visible galaxies, and a comparatively negligible amount of radiation energy. Observations prior to 1998 consistent with current spatial flatness provided support for the idea that our universe is at, or nearly at, critical density. And yet there didn't seem, at the time, to be sufficient galactic and peri-galactic (*i.e.* virial) dark matter to account for this. However, since the 1998 discovery of dark energy, the balance of the previously missing critical density has been wholly ascribed to a mysterious energy within the intergalactic vacuum. As such, cosmological general relativity equations now incorporate a "cosmo-

logical constant" to represent this non-matter dark vacuum energy.

Furthermore, observations of galactic rotation [1], the Milky Way [2], and the cosmic microwave background (CMB) anisotropy appear to confirm that the galactic and peri-galactic dark matter mass is approximately 5 to $5\frac{1}{2}$ times the visible galactic matter mass. For instance, the Gaia-Hubble Collaboration reported in March 2019 that the Milky Way has a total virial mass of approximately 1.5 trillion MΘ and a visible matter mass of 250 billion MΘ, in support of a 5:1 dark matter to visible matter ratio. A recent consensus [3] is that the visible baryonic matter of the universe comprises 4.95%, the galactic and peri-galactic dark matter comprises 26.55%, and the dark vacuum energy comprises 68.5% of the critical density (ρ_c), now estimated to be 8.533×10^{-27} $kg{\cdot}m^{-3}$ (using the 2018 Planck Collaboration H_0 consensus value, 67.4 ± 0.5 $km{\cdot}s^{-1}{\cdot}Mpc^{-1}$).

One of the puzzling things about the current cosmological energy density partition of approximately one-third total matter mass-energy and approximately two-thirds dark vacuum energy is the fact that, at present, these energy densities are of the same order of magnitude! This appears to be an extraordinary coincidence, because the ΛCDM concordance model stipulates that the total matter mass-energy density must have been many orders of magnitude greater than the vacuum energy density in the early universe and will be many orders of magnitude smaller than the vacuum energy density in the future of the universal expansion. How then is it that we happen to be living at just the right time in the history of the universe that these energy densities are nearly equal? Or, are we wrong in assuming radically different energy density partitions in the remote past and the distant future? These and other questions arise concerning this unexpected coincidence, which is known among cosmologists as the "coincidence problem". As an aside, there is an interesting link between the coincidence problem and the cosmological constant problem, but that is beyond the scope of the current paper. In the history of progress in our understanding of the universe, unexplained coincidences have often been signposts leading to a deeper understanding.

One of the questions one might ask concerning the coincidence problem is whether there could be some systematic error in our quantitation of dark matter that, once corrected, could point to a 50%/50% energy density partition (*i.e.* 50% total matter mass-energy and 50% dark energy). This could be achieved, for instance, if approximately one-fifth of the critical energy density currently being classified as a component of the vacuum energy is actually hidden dark matter within the deep intergalactic vacuum. This has long been one of the predictions of the Flat Space Cosmology (FSC) $R_h = ct$ model [4] [5]. In fact, this model stipulates a perpetual 50%/50% energy density partition as a falsifiable prediction. This is in stark contrast to the approximately 31.5%/68.5% energy density partition now widely accepted, within tight constraints, and claimed by proponents of the ΛCDM concordance model (see [3]). Over the last 40 years, standard inflationary cosmology has been repeatedly subject to *ad hoc* adjustments from

new observations, and has made relatively few falsifiable predictions in comparison to the new FSC model [6].

Once-tight constraints, however, can sometimes be broken when new discoveries and/or theories arise. Prior to the discovery of dark energy, for instance, the very idea of a cosmological constant was thought to be highly improbable. A new case in point, as emphasized in this paper, has been the assumption that the dark matter within and haloed around the galaxies is all, or nearly all, of the discoverable dark matter within the universe.

There is now a new and very plausible theory of dark matter which should loosen the ΛCDM density partition constraints considerably. It is the purpose of this paper to show how the C.G.S.I.S.A.H. (Cold Ground State Inter Stellar Atomic Hydrogen) theory of dark matter [7] can be used to identify dark matter within the deep intergalactic vacuum which should be removed from the dark energy ledger column and placed under the total matter mass-energy ledger column.

2. Results

It has long been known that the intergalactic vacuum is exceedingly sparse with respect to matter. However, it is not entirely empty! Observational 21-cm studies of the cold ground state neutral atomic hydrogen within the intergalactic vacuum, of a similar nature to those made of the interstellar vacuum of the Milky Way, have determined an average density of approximately one atom per cubic meter [8]. Thus, the average cold ground state neutral atomic hydrogen density of the intergalactic vacuum is approximately 1.67×10^{-27} kg·m^{-3}. This is one million times less dense than that within the Milky Way galactic disc (1.67×10^{-21} kg·m^{-3}). Nevertheless, one can readily see that the following ratio equation is relevant to the purpose of this paper:

$$\left[\text{intergalactic } H \text{ density}\right] / \left[\rho_c\right] = \left[1.67 \times 10^{-27}\,\text{kg}\cdot\text{m}^{-3}\right] / \left[8.533 \times 10^{-27}\,\text{kg}\cdot\text{m}^{-3}\right] \quad (1)$$

which equals 0.195.

This is approximately one-fifth of the observed critical density!

3. Discussion

The ratio equation given in the Results section shows that the currently-observed average density of intergalactic cold ground state neutral atomic hydrogen is 19.5% of the critical density determined from the 2018 Planck Collaboration report (see [3]). This is a component of the cosmic total matter mass-energy and should not be considered as a component of the vacuum dark energy. By this calculation, one can readily see that 19.5% of the current critical density has been misappropriated by the ΛCDM concordance model as dark energy. In fact, in accordance with the new C.G.S.I.S.A.H. dark matter theory, it should be credited as intergalactic dark matter. Thus, by extending the C.G.S.I.S.A.H. dark matter concept to the intergalactic vacuum, a previously-ignored reservoir of additional dark

matter is discovered.

With correct re-apportionment of this additional dark matter to the total matter mass-energy, the cosmic critical energy density partition now becomes approximately 51% total matter mass-energy and 49% dark energy. The current negligible radiation energy contribution to the critical density does not affect the above approximations. Thus, the results of this new C.G.S.I.S.A.H. calculation may be considered to be well within the acceptable margin of observational error, and in support of the FSC prediction of 50%/50%. It should be remembered that there is no cosmological coincidence problem in the FSC model, which stipulates perpetual equality of the cosmological matter mass-energy and non-matter vacuum energy.

4. Summary and Conclusions

The new C.G.S.I.S.A.H. (Cold Ground State Inter Stellar Atomic Hydrogen) theory of dark matter is applied to the incredibly sparse cold ground state neutral atomic hydrogen within the intergalactic vacuum. Despite an average density of about one atom per cubic meter, this amounts to approximately one-fifth of the cosmic critical density! Thus, according to the new dark matter theory, the intergalactic vacuum contains an additional dark matter contribution to the total matter mass-energy ledger column which must be subtracted from the dark energy ledger column. Within the range of observational error, the resulting 51%/49% matter/dark energy partition of the critical density appears to strongly support the longstanding FSC prediction of 50%/50%. There is no cosmological coincidence problem in the FSC model.

Furthermore, this discovery of a universe comprised of 50% matter mass-energy and 50% dark energy suggests that the recent resurrection of the Dirac sea idea [9], as it may pertain to positive and negative energy eigenstates (rather than positive and negative mass eigenstates) within the FSC model, may be a guide to understanding matter and dark energy as the perpetual yin and yang of universal expansion. This is to be expected in a finite perpetual matter-generating cosmological model which begins from a zero-energy state and follows conservation of energy [10].

Dedications and Acknowledgements

This paper is dedicated to Dr. Stephen Hawking and Dr. Roger Penrose for their groundbreaking work on black holes and their possible application to cosmology. Dr. Tatum also thanks U.V.S. Seshavatharam for his co-authorship of the seminal papers of FSC, and Dr. Rudolph Schild of the Harvard-Smithsonian Center for Astrophysics for his past support and encouragement.

Conflicts of Interest

The author declares no conflicts of interest regarding the publication of this paper.

References

[1] Torres-Flores, S., *et al.* (2011) *Monthly Notices of the Royal Astronomical Society*, **416**, 1936-1948. https://doi.org/10.1111/j.1365-2966.2011.19169.x

[2] Gaia-Hubble Collaboration (2019). http://sci.esa.int/hubble/61198-hubble-and-gaia-accurately-weigh-the-milky-way-heic1905

[3] Aghanim, N., *et al.* (2018) Planck 2018 Results VI. Cosmological Parameters. http://arXiv:1807.06209v1

[4] Tatum, E.T. (2018) *Journal of Modern Physics*, **9**, 1559-1563. https://doi.org/10.4236/jmp.2018.98096

[5] Tatum, E.T. and Seshavatharam, U.V.S. (2018) *Journal of Modern Physics*, **9**, 2008-2020. https://doi.org/10.4236/jmp.2018.910126

[6] Tatum, E.T. (2018) *Journal of Modern Physics*, **9**, 1867-1882. https://doi.org/10.4236/jmp.2018.910118

[7] Tatum, E.T. (2019) *Journal of Modern Physics*, **10**, 881-887. https://doi.org/10.4236/jmp.2019.108058

[8] Cain, F. (2009) What Is Intergalactic Space? Universe Today Website. https://www.universetoday.com/30280/intergalactic-space

[9] Tatum, E.T. (2019) *Journal of Modern Physics*, **10**, 974-979. https://doi.org/10.4236/jmp.2019.108064

[10] Sapar, A. (2019) *Proceedings of the Estonian Academy of Sciences*, **68**, 1-12. https://doi.org/10.3176/proc.2019.1.01

Journal of Modern Physics, 2019, 10, 1149-1156
http://www.scirp.org/journal/jmp
ISSN Online: 2153-120X
ISSN Print: 2153-1196

Gauge Field, Fermi-Bose Duality, Minimization Entropy Reduction and Degeneracy of Critical Temperatures

Yougang Feng

College of Physics, Guizhou University, Guiyang, China
Email: ygfeng45@aliyun.com

How to cite this paper: Feng, Y.G. (2019) Gauge Field, Fermi-Bose Duality, Minimization Entropy Reduction and Degeneracy of Critical Temperatures. *Journal of Modern Physics*, **10**, 1149-1156.
https://doi.org/10.4236/jmp.2019.109075

Received: July 30, 2019
Accepted: August 11, 2019
Published: August 14, 2019

Abstract

A non-Abelian gauge field is introduced to maintain the gauge invariance for the self-similar transformation, resulting in three conservation laws. It has been found that the non-Abelian gauge field is suitable to electromagnetic interaction. The Fermi-Bose duality for blocks makes blocks act as both fermi-blocks involving in spin interaction and non-spin interaction and bose-blocks carrying non-spin interaction. The self-similar transformation requires the block type inversion guaranteed by the gauge field. There is a constant and minimization entropy reduction in the transformation. It is realized that there is degeneracy of critical temperatures in the experiments for real materials. The thermodynamic dark parameters associated with the non-spin interaction should be taken seriously.

Keywords

Gauge, Fermi-Bose Duality, Inversion, Entropy, Dark Parameters, Degeneracy

1. Introduction

Quantum field theory has been applied in the research on critical phenomena, for example, by means of renormalization group theory, perturbation theory, and Feynman graphs to compute critical points and critical exponents [1] [2] [3]. The renormalization group itself is a symmetry group, in which transformation we found coexistence of ordered blocks and disordered blocks. On this basis, the concept of isomorph spin is set up, and then some hidden symmetries have been revealed [4]. The two types of blocks make us recall the coexistence of protons and neutrons, and further, we think that there must be a gauge field to maintain

the transformation. According to the definition put forward in reference [4], the n_+-blocks are ordered blocks, with which coexisting the n_--blocks are disordered. Each lattice point is similar to a fermion, and they can form an n_+-block spin behaving as a fermion. We call the n_+-block as fermi-block. An n_+-block spin has Z (coordinate number) nearest neighbor n_+-blocks, and these Z coupled block spins have different energy states due to Pauli exclusion principle, leading to that this block spin has Z different spin states at least. This is the reason why we yet introduce hyperspin Y_f for the blocks, besides the isomorph spin I_f [4]. Furthermore, a block is a set of lattices; it is these lattices that give the block a peculiar ability to possess more states a particle not having. For example, two states of $I_f = 1/2$ and $I_f = 1$ [4], by which a block can behave as either fermi-block participating in spin interaction and non-spin interaction or bose-block carrying the non-spin interaction, which will be illustrated in Section 2.

The spin interaction is essentially electromagnetic interaction in which spins take part. Since each block contains charged lattice spins, the block always has nonzero charge although it may have zero-spin. The so-called non-spin interaction is different from neither weak interaction nor strong interaction; it is just an electromagnetic interaction in which no spin involve. Particle physics tells us that the electromagnetic field is, in nature, an Abelian gauge field introduced to maintain the invariance U(1) of electromagnetic interaction. Non-Abelian gauge field is available for those interactions to keep the invariance of SU(2), etc. [5]. Studying continuous phase transition, however, we see that there is localized SU(2) symmetry describing non-spin electromagnetic interaction, indicating that non-Abelian gauge field is also suitable for electromagnetic interaction. For this reason, we neglect mass to explore the gauge field in this paper.

In Section 2, at first, we introduce a gauge field on a finite hierarchy of the self-similar transformation at temperature T, and get W_+-blocks, W_--blocks, and Z_0-blocks carrying the non-spin interaction like bosons. We call them as bose-blocks. Then, we discover Fermi-Bose duality for blocks, we've revised the explanation of the excitation states and the intermediate states of reference [4]. In Section 3, we discuss gauge field relating to the block type inversion when temperature charges and system entropy evolution, finding constant $k_B \ln 2$ and minimization entropy reduction. We explain why the scaling law only occurs nearby the first critical temperature T_{cf} and there is degeneracy of critical temperatures for experimental specimens; point out that the thermodynamic dark parameters will play important roles in the further research on phase transition. Section 4 is conclusion remark.

2. Theory

2.1. Gauge Field and Three Conservation Laws

On the r-th hierarchy, $0 < r < +\infty$, at temperature T_m, the state of an ordered n_+^m-block is ψ_+^m (the superscript m relates to T_m, the following are the same as), the state of a disordered n_-^m-block is ψ_0^m, the two states are regarded as iso-

morph spin doublet for an identical block, represented as

$$\psi = \begin{pmatrix} \psi_0^m \\ \psi_+^m \end{pmatrix} \tag{1}$$

its conjugate state is $\bar{\psi}$. The Lagrangian density of the interaction in which a gauge field participates is expressed by [6]

$$L^m = \bar{\psi} i\gamma^\mu \left(\partial_\mu - igT^i A_\mu^i\right)\psi - \frac{1}{4}F_{\mu\upsilon}^i F^{i\mu\upsilon} \tag{2}$$

The kinetic energy term for the non-Abelian field is $\left(-1/4\right)F_{\mu\upsilon}^i F^{i\mu\upsilon}$, and

$$F_{\mu\upsilon}^i = \partial_\mu A_\upsilon^i - \partial_\upsilon A_\mu^i + g\varepsilon^{ijk} A_\mu^j A_\upsilon^k \tag{3}$$

where g is a constant. The term of interaction between the gauge field and the isomorph spin field is

$$g\bar{\psi}\gamma^\mu T^i A_\mu^i \psi \tag{4}$$

There are three matrices for $T^i, i = 1,2,3$,

$$T^1 = \frac{1}{2}\begin{pmatrix} 0 & 1 \\ 1 & 0 \end{pmatrix},\ T^2 = \frac{1}{2}\begin{pmatrix} 0 & -i \\ i & 0 \end{pmatrix},\ T^3 = \frac{1}{2}\begin{pmatrix} 1 & 0 \\ 0 & -1 \end{pmatrix} \tag{5}$$

Substituting Formula (5) into Formula (4), we get

$$\frac{1}{2}g\bar{\psi}\gamma^\mu \begin{pmatrix} Z_0^m & \sqrt{2}W_-^m \\ \sqrt{2}W_+^m & -Z_0^m \end{pmatrix}\psi \tag{6}$$

W_+^m and W_-^m are newly defined fields:

$$W_-^m = \left(1/\sqrt{2}\right)\left(A_\mu^1 - iA_\mu^2\right),\ W_+^m = \left(1/\sqrt{2}\right)\left(A_\mu^1 + iA_\mu^2\right) \tag{7}$$

And the third new field follows

$$Z_0^m = A_\mu^3 \tag{8}$$

The definition of W_-^m and W_+^m differs from that of the particle physics [5]. Using Formula (1), the Formula (6) becomes

$$\frac{g}{2}\left[\overline{\psi_0^m}\gamma^\mu Z_0^m \psi_0^m + \sqrt{2}\overline{\psi_0^m}\gamma^\mu W_{-,\mu}^m \psi_+^m + \sqrt{2}\overline{\psi_+^m}\gamma^\mu W_{+,\mu}^m \psi_0^m - \overline{\psi_+^m}\gamma^\mu Z_0^m \psi_+^m\right] \tag{9}$$

Each term contains three block states, i = 1, 2, 3, which parameters satisfy three conservation laws:

$$\sum_{i=1}^3 Y_{f,i} = 0,\ \sum_{i=1}^3 S_i = 0,\ \sum_{i=1}^3 I_{f3,i} = 0 \tag{10}$$

where the units for Y_f, S, and I_{f3} are defined by reference [4]. The states W_+^m, W_-^m, and Z_0^m correspond to W_+^m-blocks, W_-^m-blocks, and Z_0^m-blocks, respectively, carrying the non-spin interaction, and they are bose-blocks. The bose-blocks are somewhat like the Cooper electron pairs of BCS theory of superconductivity [7]. In addition, the four terms of Formula (9) show there are four kinds of the non-spin interactions and seems to be no limit to the interaction length, unlike that the spin interaction is limited to blocks as their neighbors (Ising models).

2.2. Fermi-Bose Duality

Referring to Figure 1 and Figure 3 of reference [4], the structure of a n_+-block for the plane square lattice system is different from that of a n_+-block for a plane triangle lattice system. For the latter, a n_+-block and a n_--block are clearly separated. For the former, a n_+-block consists of n_+ lattices, n_- of which construct a n_--block, $n_- < n_+$. According to the renormalization group theory, when we only consider a block its inner structure is indistinguishable, namely, the lattices can be neglected. For the plane square lattice system, as the symmetry center of a n_+-block and the symmetry center of a n_--block are not superposed, so they are two blocks, just as the center of positive charge and the center of negative charge of a water molecule of three atoms containing positive charges and negative charges are not covered with each other, and the water molecule is a polar molecule, the two charges hence play their respective roles. The above interpretation is also applicable to the simply cubic lattice system.

Referring to Figure 5 of reference [4], the following symbol→represents corresponding relation between states, with the relevant parameters listed:

$$\psi_+^m \to A_+ : Y_f = 1, S = 1, I_{f3} = 1/2;$$

$$\psi_0^m \to B_+ : Y_f = 1, S = 0, I_{f3} = -1/2;$$

$$\overline{\psi_+^m} \to A_- : Y_f = -1, S = -1, I_{f3} = -1/2;$$

$$\overline{\psi_0^m} \to B_- : Y_f = -1, S = 0, I_{f3} = 1/2.$$

As there is not any other type of block except the n_+-blocks and the n_--blocks, the Fermi-Bose duality makes the existences of W_+-blocks, W_--blocks, and Z_0-blocks become possible:

$$W_+^m \to A_+^* : Y_f = 0, S = 1, I_{f3} = 1;$$

$$W_-^m \to A_-^* : Y_f = 0, S = -1, I_{f3} = -1;$$

$$Z_0^m \to A_0 \text{ or } B_0 : Y_f = 0, S = 0, I_{f3} = 0.$$

The A_+ and A_- are the ground states for the n_+-blocks, the B_+ and B_- are the ground states for the n_--blocks, they have the same isomorph spin $I_f = 1/2$. The A_+^* and A_-^* are the excitation states for the n_+-blocks, with $I_f = 1$, for which the explanation of reference [4] is not precise. As the same reason, the intermediate states A_0 and B_0 come out of the n_+-blocks and the n_--blocks, respectively. All these states are originated in the n_+-blocks and the n_--blocks, belonging to the isomorph spin octet. By the previous corresponding relations, for example, the parameters of the states B_-, A_-^*, and A_+ in the second term of Formula (9) successively are $Y_{f,1} = -1$, $S_1 = 0$, $I_{f3,1} = 1/2$, $Y_{f,2} = 0$, $S_2 = -1$, $I_{f3,2} = -1$, $Y_{f,3} = 1$, $S_3 = 1$, $I_{f3,3} = 1/2$, accord with the conservation laws given by Formula (10).

An important feature is that the formula can only describe the initial or final states of the interaction, and cannot show the intermediate process. Actually, there is not any block having a changeless state, every block is in a dynamic

process, all the states are changing, at the same time comply with the relative symmetry and the conservation laws. As geometric positions cannot be changed the non-spin interaction only is accomplished by exchanging states. Let states α, β, and λ are in the same term, α and β interact through λ, one possible way to do this is as follows: The α goes to the λ, the λ goes to the α in turn; then the β goes to the λ, and inversely, the λ goes to the β; by swapping with the λ, the original α and β exchange. If you continue like this, you may revert to your original state. This picture is available for the first and fourth terms of Formula (9). Another scene may be suitable to the interactions in the second and third terms of the formula: As all state transition, excitation, and degeneration should go through the intermediate states, the exchange with the excited state is completed in there. What's more, the intermediate states of the n_+-blocks and the n_--blocks are exactly the same, which is the property that allows the interactions to come true. Meanwhile, there could be a situation where the original states in the second term are interchanged with the original states in the third term by one-to-one correspondence way, keeping the Lagrangian density constant. Balance the energy must be in the interactions.

We can think of those states in each interaction term as bound states made up of blocks. The three conservation laws list a restricted condition for the block spin states in the non-spin interaction, embodied in the fourth term of Formula (9): The block spin parallel pairs are forbidden to participate in this interaction. It shows that the block spin states are, in the non-spin interaction sense, not randomly distributed, but a conditional combination.

On the other hand, both combinations of spin parallel and spin anti-parallel are allowed in the spin interaction. Considering the two kinds of interactions, it can be seen that the way of the spin anti-parallel has larger existence probability, such that the total spin is always zero at any finite hierarchy of the transformation course, and the system becomes ordered only if through infinitely hierarchical transformation. As the spin-up parallel and the spin-down parallel are two states of energy lower than that of the anti-parallel state, they are two sides for the block magnetic spin-pair energy symmetry, having the same value, which evidences there is no Goldstone bosons derived from the spontaneous symmetry [8] [9].

3. Discussion

3.1. Block Type Inversion

Temperatures T_{m+1} and T_m are, $T_{cs} < T_m < T_{m+1} \le T_{cf}$, so close to each other that the n_+^{m+1}-blocks transfer into the n_-^m-blocks when temperature changes from T_{m+1} into T_m. Because the block's fractal dimension is a monotonically increasing function of the block side length in the region $T_{cs} < T \le T_{cf}$, the T_{cs} is the secondary phase transition critical temperature [4]. The longer the side length is, the larger the dimension will be, when the temperature drops [9]. This means that there is block type inversion. For example, in the plane triangle lattice spin system:

$n_-^{m+1}=19$, $n_+^{m+1}=20$, and $n_-^m=20$, $n_+^m=21$. The ordered n_+^{m+1}-block at T_{m+1} turns into the disordered n_-^m-block at T_m. If the n_+^{m+1}-block kept the state $\overline{\psi_+^{m+1}}$, instead of the state $\overline{\psi_0^m}$, the second interaction term in Formula (9) would show as

$$\sqrt{2}\overline{\psi_+^{m+1}}\gamma^\mu W_{-,\mu}^m \psi_+^m \tag{11}$$

This term violates the conservation laws of Formula (10), so it won't exist. Apparently, it is the gauge field that forces the n_+^{m+1}-blocks to reverse into the n_-^m-blocks, keeping the gauge invariance.

3.2. Constant $k_B$ln2 and Minimization Entropy Reduction

Because of the additive nature of entropy, we divide the system entropy H_e relating to magnetism into two parts: The first part H_{e1} is made by the existence probabilities of the n_+-blocks and the n_--blocks, and the second, H_{e2}, is determined by the various states combinations of these two types of blocks. The first part is denoted as H_{e1} [10],

$$H_{e1}=-k_B\left[P_+\ln P_+ + P_-\ln P_-\right] \tag{12}$$

where k_B is Boltzmann constant, P_+ and P_- are the occurrence probabilities for n_+-blocks and n_--blocks, respectively. As $P_+=P_-=1/2$, we get

$$H_{e1}=k_B\ln 2 \tag{13}$$

The constant is available for the region $T_{cs}<T\le T_{cf}$. The second part is constant independent of the finite hierarchy since the symmetry of the self-similar transformation. Therefore, the self-similar transformation for a certain temperature is an isentropic process.

On one hand, the magnitude of the system entropy loss is $\left|\Delta H_{e,+}^m\right|$, $\Delta H_{e,+}^m<0$, caused by the n_+^m-blocks for the degree of order of the system increases with the temperature decreases. On the other hand, the n_-^m-blocks are the disordered blocks closest to the n_+^m-blocks at T_m, responsible for the system entropy increase $\Delta H_{e,-}^m>0$, so the entropy reduction is minimized. The change in the system entropy takes

$$\Delta H_e^m=\Delta H_{e,+}^m+\Delta H_{e,-}^m<0 \tag{14}$$

We understand that for a certain temperature T_m, the n_+^m-block is as small as possible ordered block, the n_-^m-block is as large as possible disordered block, this is an ordered path to minimum entropy reduction.

As T_m is an arbitrary temperature in the previous temperature region, we have

$$\mathrm{d}^2H_e/\mathrm{d}T^2\approx 0 \tag{15}$$

The decrease in the system entropy with the temperature declining is approximately homogeneous.

3.3. Degeneracy of Critical Temperatures

The lattice spin correlation length is the same as the block side length, depend-

ing on temperature. The lower the temperature is, the larger both lengths become. The temperature at which all transition hierarchies disappear is defined as the secondary phase transition critical temperature T_{cs}. The largest lengths occur at the T_{cs}. The lengths corresponding to the block minimum fractal dimension appear at the T_{cf} [4]. In addition, the system's size restricts the values of both the largest side length and the correlation length. For an infinite system, if the block side length is finite in the transformation course, the hierarchical number is infinite. When the whole system becomes a block with its side length equaling the system's size, the hierarchy vanishes; while both lengths are infinite. There is a large enough temperature gap between T_{cs} and T_{cf}, which we call the renormalization region, where the scaling law exists [9]. For a finite system, if the side length is smaller than the system's size in the changing course, the number of the hierarchies are finite. When the side length turns into the system's size, the whole system is an isolated block and the hierarchy vanishes, while the correlation length is the same as the system's size.

The object of our theoretical study is an infinite system, the predicted laws cannot be fully displayed in the actual samples. All experimental specimens have only very limited size and one feature in common: the scaling law always appears nearby T_{cf}. It is the very finite size that leads to few transformation hierarchies. The T_{cs} is so close to the T_{cf} that the experimenters cannot distinguish both of them. The false image misleads to that there were no concepts of the T_{cs} and the secondary phase transition. An important sign of the indistinguishability of the two critical temperatures is that the correlation length nearby T_{cf} has covered entire specimens. We call this phenomenon as degeneracy of critical temperatures. Actual materials having the same molecular formula and crystal structure commonly share the same inherent T_{cf}. If they are all small, they all have the degeneracy phenomenon, otherwise the degeneracy will disappear: the larger the size, the lower the T_{cs}.

The analogous case concerns the compute simulation experiments [11] [12]. It's said that there is no block soon after the first phase transition nearby T_{cf}. In fact, the whole system has, at that moment, become an isolated block with its side length comparable to the system's size for the system is quite limited. One final point to note is that since we are concern about the phase transition under thermodynamic equilibrium state the simulation should insist the critical limit principle of maximum entropy and take the ordered path to minimum entropy reduction [9]. We expect the simulation test for a massive system on giant supercomputers may eliminate the degeneracy phenomenon.

3.4. Thermodynamic Dark Parameters

That an n_{-}-block is regarded as disordered mainly refers to magnetism, in the isomorph spin sense, however, it is also an ordered organization. So far, all thermodynamic parameters of the critical phenomena only involve the spin-interaction, ignoring the non-spin interaction. We call the parameters associated with the non-spin interaction such as energy, partition function, entropy, and free energy,

etc. thermodynamic dark parameters, which affect the system's property as much as the conventional parameters do.

4. Conclusion Remark

It is first found that the non-Abelian gauge field is suitable for the non-spin electromagnetic interaction in the continue phase transition, in which the blocks illustrate Fermi-Bose duality. The gauge field maintains the self-similar transformation and makes system take the ordered path to minimum entropy reduction. The degeneracy of critical temperatures interprets the reason why the scaling law shows only nearby the first critical temperature for the real experimental specimens. The concept of thermodynamic dark parameters associated with the non-spin interaction is proposed firstly.

Conflicts of Interest

The author declares no conflicts of interest regarding the publication of this paper.

References

[1] Zinn-Justin, J. (2007) Phase Transitions and Renormalization Group. Oxford University Press, Oxford. https://doi.org/10.1093/acprof:oso/9780199227198.001.0001

[2] Moshe, M. and Zinn-Justin, J. (2003) *Physics Reports*, **385**, 69-228. https://doi.org/10.1016/S0370-1573(03)00263-1

[3] Pelissetto, A. and Vicari, E. (2002) *Physics Reports*, **368**, 549-727. https://doi.org/10.1016/S0370-1573(02)00219-3

[4] Feng, Y.G. (2018) *Journal of Modern Physics*, **9**, 241-249.

[5] Weinberg, S. (1967) *Physical Review Letters*, **19**, 1264. https://doi.org/10.1103/PhysRevLett.19.1264

[6] Yang, C.N. and Mills, R.L. (1954) *Physical Review*, **96**, 191. https://doi.org/10.1103/PhysRev.96.191

[7] Bardeen, J., Cooper, L.N. and Schrieffer, J.R. (1957) *Physical Review*, **106**, 162. https://doi.org/10.1103/PhysRev.106.162

[8] Goldstone, J., Salam, A. and Weinberg, S. (1962) *Physical Review*, **127**, 965. https://doi.org/10.1103/PhysRev.127.965

[9] Feng, Y.G. (2018) *Journal of Modern Physics*, **9**, 2035-2044. https://doi.org/10.4236/jmp.2018.911128

[10] Gray, R.M. (2009) Entropy and Information Theory. Springer-Verlag, New York.

[11] Binney, J.J., Dowrick, N.J., Fisher, A.J. and Newman, M.J. (1992) The Theory of Critical Phenomena: An Introduction to the Renormalization Group. Oxford University Press, Oxford.

[12] Reynolds, P.J., Stanley, H.E. and Klein, W. (1977) *Journal of Physics C*: *Solid State Physics*, **10**, L167. https://iopscience.iop.org/article/10.1088/0022-3719/10/8/002/meta https://doi.org/10.1088/0022-3719/10/8/002

Call for Papers

Journal of Modern Physics

ISSN: 2153-1196 (Print) ISSN: 2153-120X (Online)
http://www.scirp.org/journal/jmp

Journal of Modern Physics **(JMP)** is an international journal dedicated to the latest advancement of modern physics. The goal of this journal is to provide a platform for scientists and academicians all over the world to promote, share, and discuss various new issues and developments in different areas of modern physics.

Editor-in-Chief

Prof. Yang-Hui He City University, UK

Subject Coverage

Journal of Modern Physics publishes original papers including but not limited to the following fields:

Biophysics and Medical Physics
Complex Systems Physics
Computational Physics
Condensed Matter Physics
Cosmology and Early Universe
Earth and Planetary Sciences
General Relativity
High Energy Astrophysics
High Energy/Accelerator Physics
Instrumentation and Measurement
Interdisciplinary Physics
Materials Sciences and Technology
Mathematical Physics
Mechanical Response of Solids and Structures
New Materials: Micro and Nano-Mechanics and Homogeneization
Non-Equilibrium Thermodynamics and Statistical Mechanics
Nuclear Science and Engineering
Optics
Physics of Nanostructures
Plasma Physics
Quantum Mechanical Developments
Quantum Theory
Relativistic Astrophysics
String Theory
Superconducting Physics
Theoretical High Energy Physics
Thermology

We are also interested in: 1) Short Reports—2-5 page papers where an author can either present an idea with theoretical background but has not yet completed the research needed for a complete paper or preliminary data; 2) Book Reviews—Comments and critiques.

Notes for Intending Authors

Submitted papers should not have been previously published nor be currently under consideration for publication elsewhere. Paper submission will be handled electronically through the website. All papers are refereed through a peer review process. For more details about the submissions, please access the website.

Website and E-Mail

http://www.scirp.org/journal/jmp **E-mail: jmp@scirp.org**

What is SCIRP?

Scientific Research Publishing (SCIRP) is one of the largest Open Access journal publishers. It is currently publishing more than 200 open access, online, peer-reviewed journals covering a wide range of academic disciplines. SCIRP serves the worldwide academic communities and contributes to the progress and application of science with its publication.

What is Open Access?

All original research papers published by SCIRP are made freely and permanently accessible online immediately upon publication. To be able to provide open access journals, SCIRP defrays operation costs from authors and subscription charges only for its printed version. Open access publishing allows an immediate, worldwide, barrier-free, open access to the full text of research papers, which is in the best interests of the scientific community.

- High visibility for maximum global exposure with open access publishing model
- Rigorous peer review of research papers
- Prompt faster publication with less cost
- Guaranteed targeted, multidisciplinary audience

Scientific Research Publishing

Website: http://www.scirp.org

Subscription: sub@scirp.org

Advertisement: service@scirp.org